UNIVERSITY OF THESSALY
POLYTECHNIC SCHOOL
DEPARTMENT OF MECHANICAL ENGINEERING

Diploma Thesis

RAREFIED GAS FLOWS IN MICRO ENCLOSURES DUE TO NON-ISOTHERMAL WALLS

by

GEORGIOS TATSIOS

Submitted for the Partial Fulfillment
of the Requirements for the Degree of
Diploma in Mechanical Engineering
2014

ΠΑΝΕΠΙΣΤΗΜΙΟ ΘΕΣΣΑΛΙΑΣ
ΒΙΒΛΙΟΘΗΚΗ & ΚΕΝΤΡΟ ΠΛΗΡΟΦΟΡΗΣΗΣ
ΕΙΔΙΚΗ ΣΥΛΛΟΓΗ «ΓΚΡΙΖΑ ΒΙΒΛΙΟΓΡΑΦΙΑ»

Αριθ. Εισ.: 12794/1
Ημερ. Εισ.: 10-09-2014
Δωρεά: Συγγραφέα
Ταξιθετικός Κωδικός: ΠΤ – ΜΜ
2014
ΤΑΤ

© 2014 Tatsios Georgios

The approval of the Diploma Thesis by the Department of Mechanical Engineering of the University of Thessaly does not imply acceptance of the author's opinions. (Law 5343/32, article 202, paragraph 2).

Εγκρίθηκε από τα Μέλη της Τριμελούς Εξεταστικής Επιτροπής:

Πρώτος Εξεταστής (Επιβλέπων)	Βαλουγεώργης Δημήτριος Καθηγητής, Τμήμα Μηχανολόγων Μηχανικών, Πανεπιστήμιο Θεσσαλίας
Δεύτερος Εξεταστής	Μποντόζογλου Βασίλειος Καθηγητής, Τμήμα Μηχανολόγων Μηχανικών, Πανεπιστήμιο Θεσσαλίας
Τρίτος Εξεταστής	Πελεκάσης Νικόλαος Καθηγητής, Τμήμα Μηχανολόγων Μηχανικών, Πανεπιστήμιο Θεσσαλίας

Certified by the member of the Thesis Committee:

1st member (Supervisor)	Valougeorgis Dimitrios Professor, Department of Mechanical Engineering, University of Thessaly
2nd member	Bontozoglou Vasileios Professor, Department of Mechanical Engineering, University of Thessaly
3rd member	Pelekasis Nikolaos Professor, Department of Mechanical Engineering, University of Thessaly

Acknowledgements

I would like to express my gratitude to my supervisor, Prof. Dimitrios Valougeorgis, for his support, inspiration and understanding throughout the period I was working on my thesis. His constant guidance had a major impact to the quality of this thesis.

I am grateful to Prof. Stefan Stefanov and Manuel Vargas for their contribution to the thesis and great collaboration, as the biggest part of it, is part of our conjoint work. I would also like to thank the members of the committee, Prof. Vasileios Bontozoglou and Prof. Nikolaos Pelekasis for dedicating their time to read the thesis. I am grateful to Steryios Naris for the discussions we had and his eagerness to help when I faced difficulties.

I would like to thank my parents, Athanasios Tatsios and Maria Iliadou as well as my sister Natasa for their continuous support. Finally, I am grateful to Anna Papageorgiou for her patience and to my friends for their support.

RAREFIED GAS FLOWS IN MICRO ENCLOSURES DUE TO NON-ISOTHERMAL WALLS

Georgios Tatsios
University of Thessaly, Department of Mechanical Engineering, 2014

Supervisor: Valougeorgis Dimitrios, Professor, Department of Mechanical Engineering, University of Thessaly

Abstract

This work is focused in non-equilibrium thermally induced flows in cavities. Such configurations have lately received considerable attention due to their implementation in the cooling process of vacuum packed micro-electromechanical systems. The low pressure and small characteristic dimensions of these systems, lead to conditions that are beyond the range of application of the usual Navier-Stokes formulation, as the gas cannot be considered a continuous medium and a kinetic approach is required.

The problem is described by the integro-differential Boltzmann equation, which in contrast to the Navier-Stokes, considers the gas as a number of discrete particles. The solution of the Boltzmann equation though, is a demanding and computationally expensive task because of the complicated collision term. One of the methods to overcome this is using kinetic models that provide a relaxation to this term, reducing the computational cost. In the present work the Shakhov kinetic model equation has been numerically solved for the simulation of the flow.

In every point of the flow domain there are particles that have arrived after an arbitrary number of collisions since they were emitted from the boundary, and particles that have arrived without colliding. Whether the number of the former or latter kind of particles is bigger, has a great impact on the flow field, and leads to very interesting phenomena. Here a procedure is introduced for the deterministic calculation of the impact either of these kinds of particles has on the flow field.

It is believed that the present work has both scientific and technological interest and it may support the design and optimization of microdevices with respect to heat transfer mechanisms.

Αραιοποιημένες ροές αερίων σε μικρό-κοιλότητες λόγω μη ισοθερμοκρασιακών τοιχωμάτων

Γεώργιος Τάτσιος
Πανεπιστήμιο Θεσσαλίας, Τμήμα Μηχανολόγων Μηχανικών, 2014

Επιβλέπων: Βαλουγεώργης Δημήτριος, Καθηγητής, Τμήμα Μηχανολόγων Μηχανικών, Πανεπιστήμιο Θεσσαλίας

Περίληψη

Η παρούσα εργασία επικεντρώνεται σε ροές εκτός θερμοδυναμικής ισορροπίας σε κοιλότητες λόγω θερμοκρασιακών βαθμίδων. Τέτοιες διατάξεις έχουν λάβει ενδιαφέρον τα τελευταία χρόνια λόγω της εφαρμογής τους στην ψύξη μικροηλεκτρομηχανολογικών εξαρτημάτων, σε καταστάσεις κενού. Η χαμηλές πιέσεις καθώς και οι μικρές διαστάσεις σε αυτά τα συστήματα, οδηγούν σε συνθήκες που βρίσκονται εκτός του εύρους εφαρμογής των εξισώσεων Navier-Stokes, καθώς καταρρέει η υπόθεση του συνεχούς μέσου, και απαιτούνται κινητικές προσεγγίσεις για την μοντελοποίηση.

Η μοντελοποίηση μπορεί να γίνει με βάση την ολοκληροδιαφορική εξίσωση Boltzmann, η οποία σε αντίθεση με τις εξισώσεις Navier-Stokes δεν θεωρεί το αέριο ως ένα συνεχές μέσο, αλλά ως ένα αριθμό σωματιδίων. Η επίλυση της εξίσωσης Boltzmann είναι μία απαιτητική και υπολογιστικά ακριβή διαδικασία, λόγω του πολύπλοκου όρου των μοριακών συγκρούσεων σε αυτή. Μία από τις μεθόδους που χρησιμοποιούνται για την αποφυγή του υπολογισμού αυτού του όρου είναι η χρήση των κινητικών μοντέλων. Τα κινητικά μοντέλα παρέχουν μία χαλάρωση αυτού του όρου, μειώνοντας σημαντικά το υπολογιστικό φορτίο. Στην παρούσα εργασία το κινητικό μοντέλο του Shakhov έχει χρησιμοποιηθεί.

Σε κάθε σημείου του ροϊκού πεδίο υπάρχουν σωματίδια που φτάνουν απευθείας αφού ανακλαστούν από τα τοιχώματα, και σωματίδια που φτάνουν αφού συγκρουστούν με άλλα. Το αν υπερτερεί σε κάποιο σημείο ο αριθμός του πρώτου ή δεύτερου είδους σωματιδίων έχει μεγάλη σημασία στη δομή του ροϊκού πεδίου και οδηγεί σε ενδιαφέροντα φαινόμενα. Στην παρούσα εργασία αναπτύσσεται μία μέθοδος για τον ντετερμινιστικό προσδιορισμό της επίδρασης που έχει το κάθε είδος στο ροϊκό πεδίο.

Πιστεύεται πως η παρούσα εργασία έχει επιστημονικό καθώς και τεχνολογικό ενδιαφέρον και μπορεί να βοηθήσει στην βελτιστοποίηση μια κατηγορίας μικροηλεκτρομηχανολογικών εξαρτημάτων.

Contents

List of Figures

List of Tables

Chapter 1 Introduction

1.1 The origin of kinetic theory

The nature of matter itself has been a topic of debate among philosophers and scientist since the ancient times. They were divided into two schools, the one believing that matter is a continuum, much like time, and the other believing that all things were composed by tiny bits of matter and between them there was empty space. As time and science advanced these two ideas generated some interesting paradoxes, but the most interesting thing was that in many cases both of those methods were to produce very similar results. One of the main paradoxes was that, if all things are composed of tiny bits of matter, then all interaction between them could be time-reversed (assuming elastic collisions between them), as their motion could be modeled by the classical mechanics. If it is so, then why are macroscopic processes irreversible?

Such questions were answered by kinetic theory. Kinetic theory first originated in 1738 when Daniel Bernoulli stated in his book Hydrodynamica [1] that gasses consist of large amounts of molecules travelling in all directions, that pressure is the force excreted by those molecules to a surface during a collision, and that heat is just the kinetic energy of the molecules. Great advances in Kinetic Theory were to come much later, when in 1878 Clausius [2] introduced the mean free path and Maxwell in 1860 [3] who laid the road for a statistical description of gasses, introducing the concept of the velocity distribution function, a tool that could be used to compute the probability of finding a molecule in a certain range of its microscopic velocity. Although Maxwell came very close to extracting the expression for the calculation of this function (the Boltzmann equation), it was Boltzmann in 1872 [4] that made the final steps to its derivation and so this expression is accorded to him.

1.2 The Knudsen number and flow regimes

Kinetic theory using the velocity distribution function and the Boltzmann equation can be used to provide interesting theoretical results, such as the transport coefficients, for all dilute gasses. The solution of the Boltzmann equation though is a very demanding process, and is used for the simulation of practical problems only when absolutely necessary. The main advantage it has against other methods of gas modeling is that the only assumption that needs

to be made is the specification of the intermolecular interaction model, so it is has a greater range of applications than most continuum methods. The dimensionless parameter that gives us the information of whether the solution of the Boltzmann equation is needed, or that other approaches are valid is the Knudsen number.

The Knudsen number is defined as the ratio of the mean free path of the molecules over a characteristic length of the problem [5]

$$Kn = \frac{\lambda}{L} \tag{1.1}$$

The mean free path for the Hard Sphere model for a single gas can be expressed as [5]

$$\lambda = \frac{m}{\sqrt{2}\pi d^2 \rho} \tag{1.2}$$

where m is the molecular mass, d is the diameter of the molecule and ρ is the gas density. It is seen that for a specific gas the mean free path is a function only of density, and is inversely proportional to it. The Knudsen number is a measure of the gas rarefaction, and a measure of the departure from thermodynamic equilibrium.

The Knudsen number is related to other important dimensionless parameters, such as the rarefaction parameter

$$\delta = \frac{PL}{\mu u_0} = \frac{\sqrt{\pi}}{2Kn} \tag{1.3}$$

and the Mach and Reynolds numbers [5]

$$Kn = \frac{Ma}{\mathrm{Re}} \sqrt{\frac{\gamma\pi}{2}} \tag{1.4}$$

where P is the gas pressure, μ is the dynamic viscosity, $u_0 = \sqrt{2\frac{k_B}{m}\mathrm{T}}$ is the most probable molecular thermal velocity, k_B is the Boltzmann constant and γ is the ratio of the specific heats of the gas.

According to the Knudsen number the flow regimes can be defined, as shown below in Table 2. The Boltzmann equation, although valid in the whole range of the Knudsen number, is utilized only in the transition and free molecular regimes because of the high computational cost that it requires.

Table 1: The cross and direct effects

	Heat flux	Momentum flux	Mass flux
$\vec{\nabla}T$	Heat conduction	Thermal creep	Thermal diffusion
$\vec{\nabla}P$	Mechanocaloric effect	Poiseuille flow	Baroeffect
$\vec{\nabla}C$	Duffour effect	Diffusion baroeffect	Diffusion flow

When the Knudsen number is small and the flow is in the continuum regime, the macroscopic approach of the Euler and Navier Stokes equations can be used with very good accuracy. As the Knudsen number is increased and we move to the Slip regime, the no slip boundary conditions associated with the Navier Stokes equations start to collapse. This can be treated with velocity slip and temperature jump boundary conditions [6], and the range of their application is extended. In those regimes the flow is near thermodynamic equilibrium.

As the Knudsen number is increased and the flow further departs from thermodynamic equilibrium, the Newton, Fourier and Fick laws do not hold and the continuum approach collapses. It is in those regimes, the transition and free molecular, that very interesting non-equilibrium phenomena start to appear, and the flow can only be simulated using kinetic approaches [7],[8].

If we consider the three driving forces acted on gases being temperature gradient, pressure gradient and concentration gradient, then the result of those forces according to continuum approaches will be heat flux, momentum flux and mass flux respectively. Those are called direct effects. In flows far from thermodynamic equilibrium six more effects are present, the cross effects. They are shown in Table 1. Those effects are beyond the range of the continuum models, and can be modeled by kinetic approaches.

The direct solution of the Boltzmann equation is a very hard and computationally demanding process. To overcome this, certain methods are used in order to obtain kinetic solutions without solving the exact Boltzmann equation (BE). One of them is the use of kinetic models. Kinetic models provide a relaxation to the collisional term of the BE, making the solution faster. The most well-known kinetic models are the BGK [9], the Shakhov [10] and Ellipsoidal [11] models for monatomic single gas flows, the Rykov [12] and Holway [13] models for polyatomic single gas flows and the McCormak [14] model for gas mixtures.

Table 2: Knudsen regimes

Range of Kn	Regime	Governing Equations	Numerical approach
$Kn \to 0$	Continuum (inviscid)	Euler	Typical CFD schemes
$Kn < 10^{-3}$	Continuum (viscous)	Navier Stokes	
$10^{-3} < Kn < 10^{-1}$	Slip (viscous)	Navier Stokes with slip boundary conditions, Generalized equations.	
$10^{-1} < Kn < 10$	Transition (Knudsen)	Boltzmann Kinetic models	Analytical methods, Variational methods, Discrete velocity method Integro-moment method DSMC
$10 < Kn$	Free molecular	Boltzmann and kinetic models without collisions	Method of characteristics Test particle Monte Carlo

In order for a model to be accepted it must: satisfy the collision invariants, satisfy the H-theorem and provide the correct expressions for the transport coefficients.

Another very widely used method for the simulation of such flows is the Direct Simulation Monte Carlo method (DSMC) [7]. This is a stochastic method, in contrast to the direct solution of the BE or model equations. For the solution the flow domain is discretized and a big number of fictional particles (simulators) are distributed on the field, each of them corresponding to a large number of real particles. Then the real motion of the particles is

divided into two parts, the free motion according to a distance proportional to their velocities and the time step, and a collision part, where the collisions are simulated in a stochastic manner. The macroscopic quantities are sampled for a large number of time steps, and are calculated using the simulator particles microscopic quantities.

A number of methods have been proposed, using high-order equations [15] derived from the BE. Those methods are able to simulate flows in the slip and early transition regimes, capturing effects that are beyond the NSF (Navier-Stockes-Fourier) analysis. The most know of them are the Burnett equations. Those methods have some known problems, like stability issues, and can be misleading when used in the whole transition regime.

1.3 Temperature driven flows and related applications

The literature survey on rarefied gas flows driven by temperature differences on the basis of kinetic theory is very extensive. A thorough description of various types of thermal flows may be found on a recent book by Sone [6]. A brief description of thermal creep, thermophoresis and thermal-stress slip flow is given here.

Thermal creep is one of the six cross effects mentioned. It is momentum transfer due to temperature gradient. When a temperature gradient is imposed to a wall, momentum is transferred in a direction opposing that of the temperature gradient, leading to a flow from cold-to-hot. This phenomenon is not prevailing in the continuum regime, as the natural convection is the dominant effect. In the absence of gravity, or in cases where gravitational forces are negligible, such as rarefied flows, thermal creep is very important.

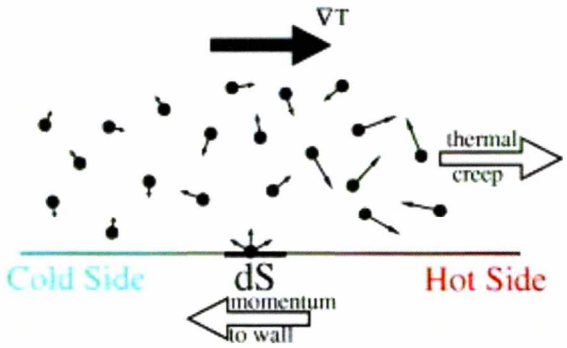

Figure 1: Thermal creep flow

An explanation to thermal creep, shown in Figure 1 is the following. Particles in the hot side of the wall travel with large thermal velocities and as they collide with the wall in a

differential area dS their velocity is decreased. Particles from the cold side of the wall have small thermal velocities. As they collide with the wall at a differential area dS their velocity is increased. In both cases the velocity is increased when moving from cold to hot, and decreased when moving in the other way. This leads to momentum transfer, opposite to the temperature gradient.

Thermophoresis [16] is a phenomenon of temperature induced flows around particles submerged in a gas with temperature gradient, when the dimension of the particles is of the order of a mean free path. This flow exerts a force on the particle, called thermal force. If the particle is free, it drifts because of the thermal force. This whole phenomenon is called thermophoresis. This flow has long been of interest, especially in the field of aerosol sciences.

Thermal stress [17] is exerted on any surface element in a gas with a nonuniform temperature gradient, as a result of the different thermal velocities the incident to the surface molecules have. If we consider a differential volume element in such a gas, then the contribution of the thermal stress on the volume of the gas surrounded by this volume element vanishes when integrated over the element, if the linear theory is applicable. In the special case where a surface of this volume element is part of the boundaries of the flow, the situation is different. Since the molecules emitted from the boundary have no tangential contribution (in the case of the diffuse boundary conditions), the thermal stress on this surface is reduced. Thus the balance of the thermal stress on the volume element is violated and a flow is induced, the thermal-stress slip flow. The difference between this kind of flow and the thermal creep flow, is that in the latter the temperature gradient is imposed on the boundary, whereas in the former case the boundaries can be isothermal.

One of the first instances where these kinds of flows were observed was in 1873, the Crookes' radiometer shown in Figure 2. It consists of an airtight bulb kept in partial vacuum and four rectangular vanes suspended by an axis, in a vertical orientation. One side of each vane is colored black, while the other is white, leading to different thermal radiation absorption coefficients. When the radiometer is exposed to thermal radiation, the vanes start rotating with the black colored side trailing. While it is clear now that the flow is induced due to thermal creep because of the temperature gradient, it became a topic of scientific debate when first observed as there was not an apparent driving force to set the vanes in motion.

Figure 2: The Crookes' radiometer

In the recent years, due to advances in the fields of nano/micro-electromechanical systems and a need for pumping in vacuum setups, these forces have begun to find applications in those areas. In the field of pumping the Knudsen pump, or Knudsen compressor has been developed. It consists of arrays of tube elements connecting the upstream and downstream vessels, their diameter being in the range of $10^{-3}\,\mathrm{m}$. The ends of those tube elements in the vicinity of the upstream vessel are kept at low temperature and the ends at the vicinity of the downstream are at a larger temperature. Thermal creep predicts a flow from cold-to-hot in those tubes. The pumping ability of this pump is regulated by the length of the tubes and their length, while the ultimate pressure difference that can be achieved is regulated by the Poisseuille flow, in the direction opposing thermal creep flow, expected due to the pressure difference of the vessels.

Temperature driven flows in nano/micro-electromechanical systems have been used in a number of setups in the recent years, mainly in sensor apparatuses. They offer considerable advantages compared to devices used different operating principals, as they usually have no moving parts, are of small size and often provide high resolution. Mass flows sensors have been developed, utilizing two temperature sensors (one upstream and one downstream of the flows) and a heat source between them. Through the different temperature readings, the mass flow rate can be extracted. Accelerometers have been constructed consisting of highly accurate temperature sensors inside of a sealed cavity containing a rarefied gas and a heat source. When external forces are acted upon the gas, the temperature profile is altered. This deviation from the temperature profile when no external forces are acted is linked to the force, and the acceleration is calculated.

1.4 Thesis objectives and structure

Thermally driven flows in microenclosures have lately received considerable attention. At some extend this is due to the potential implementation of such flows in the emerging field of microfluidics [18] and more specifically in vacuum packed MEMS [19],[20] as well as in micropumps [21],[22] and microactuators/microsensors [23],[24]. In addition to that, over the years, temperature driven flows in cavities have been commonly applied in rarefied gas dynamics as prototype problems in order to investigate theoretically interesting physical phenomena [25[29] as well as to benchmark and validate novel numerical schemes [30],[31],[32].

In the present work, thermally induced flows in two-dimensional rectangular enclosures with several boundary condition configurations are investigated in a wide range of the Knudsen number covering the slip and transition regimes. Modeling is based on the numerical solution of the Shakhov kinetic model. The influence of the Knudsen number, the temperature ratio and the cavity aspect ratio on the bulk quantities is examined. Depending on the flow in addition to the well-known thermal creep flow, the recently reported flow pattern from hot-to-cold in the vicinity of the boundaries is observed. Furthermore, a deterministic procedure equivalent to the stochastic decomposition introduced in [33] is developed in order to separately calculate the streaming and collision parts of the distribution function and help explain the mentioned hot-to-cold flow.

The thesis is outlined as follows:

- A literature review is presented in Chapter 2. The basic concepts, equations and expressions used in this work are presented.
- The mathematical formulation of the problem is presented in Chapter 3. The system of equations along with the moments and the appropriate boundary conditions are derived and their discretized form is presented.
- The deduction of the mentioned deterministic decomposition in done in Chapter 4.
- The results are presented and discussed in Chapter 5. In section 5.2 the half heated cavity problem, which is used as a benchmark problem, is discussed. In section 5.3 the bottom wall heated cavity flow with given temperature or heat flux is provided. In section 5.4 the non-isothermal lateral walls cavity flow is presented.
- Closing the thesis some concluding remarks are made in Chapter 6.

Chapter 2 Literature review

2.1 The Boltzmann equation

The velocity distribution function $f(\vec{\xi},\vec{r},t)$, where $\vec{\xi}$ is the molecular velocity vector, $\vec{r}$ is the position vector and t is time, is defined so that $f(\vec{\xi},\vec{r},t)d\vec{\xi}d\vec{r}$ is the average number of particles in the differential phase space element $d\vec{\xi}d\vec{r}$, and is a fundamental quantity in kinetic theory [5]. It contains the whole information of the gas microstate and all macroscopic quantities can be derived as moments of the distribution function. For the kinetic determination of the distribution function the Boltzmann equation (BE) is used. The derivation of the BE for monatomic single gases is presented in Appendix A. Following the procedure of Appendix A we obtain the BE in the following form

$$\underbrace{\frac{\partial}{\partial t}f(\vec{r},\vec{\xi},t)}_{\text{rate of change of the average number of particles}} + \underbrace{\vec{\xi}\frac{\partial f}{\partial \vec{r}}}_{\text{rate of change due to free motion}} + \underbrace{\vec{F}\frac{\partial f}{\partial \vec{\xi}}}_{\text{rate of change due to field forces}} = \underbrace{\int_{-\infty}^{\infty}\int_{0}^{4\pi}\left(f_1^* f^* - f_1 f\right)\vec{c}_r \sigma d\Omega d\vec{\xi}_1}_{\text{rate of change due to collisions}} = J(f) \qquad (2.1)$$

It is seen that the only quantities in the BE that need to be specified are the differential cross section σ and the differential solid angle $d\Omega$ that are given by the molecular interaction model, some of them are [5] the Hard Sphere model (HS), the Inverse Power Law model (IPL), the Maxwell model which is a special case of the IPL model, the Variable Hard Sphere model (VHS), the Variable Soft Sphere model (VSS), the Generalized Hard Sphere model (GHS) and the Generalized Soft Sphere model (GSS). Apart from those quantities each model provides expressions for transport coefficients used in the macroscopic approach.

In the derivation of the BE two main assumptions were made. BE is only applicable in dilute gasses (when the distance between molecules is much larger than the molecular diameter) as only binary collisions were assumed. It is noted that gases in atmospheric pressure are in dilute conditions. The other assumption is the molecular chaos or

Stosszahlansatz. It was introduced by Boltzmann and states that the velocities of colliding molecules are uncorrelated.

During each collision there are some quantities that are conserved. If ψ is such a quantity then during a collision of the form $\left(\vec{\xi},\vec{\xi_1}\rightarrow\vec{\xi^*},\vec{\xi_1^*}\right)$ the conservation equation can be written as

$$\psi\left(\vec{\xi}\right)+\psi\left(\vec{\xi_1}\right)=\psi\left(\vec{\xi^*}\right)+\psi\left(\vec{\xi_1^*}\right) \tag{2.2}$$

It can be shown that the average rate of change of a quantity ψ due to collisions is [5]

$$\left(\frac{\partial\psi}{\partial t}\right)_{coll}=\frac{1}{N}\int_{-\infty}^{\infty}J(f)\psi\left(\vec{\xi}\right)d\vec{\xi}=\frac{1}{N}\int_{-\infty}^{\infty}\int_{-\infty}^{\infty}\int_{0}^{4\pi}\psi\left(\vec{\xi}\right)\left(f_1^*f^*-f_1f\right)\vec{c}_r\sigma d\Omega d\vec{\xi}_1 d\vec{\xi} \tag{2.3}$$

where N is the number density. If we interchange the two velocity integration variables, substitute them with their post collision velocities, interchange the latter and sum the four expressions we get

$$\int_{-\infty}^{\infty}J(f)\psi\left(\vec{\xi}\right)d\vec{\xi}=\frac{1}{4}\int_{-\infty}^{\infty}\int_{-\infty}^{\infty}\int_{0}^{4\pi}\psi\left(\vec{\xi}\right)\left(f_1^*f^*-f_1f\right)\left(\psi\left(\vec{\xi}\right)+\psi\left(\vec{\xi_1}\right)-\psi\left(\vec{\xi^*}\right)-\psi\left(\vec{\xi_1^*}\right)\right)\vec{c}_r\sigma d\Omega d\vec{\xi}_1 d\vec{\xi}$$

and using Eq. (2.2)

$$\int_{-\infty}^{\infty}J(f)\psi\left(\vec{\xi}\right)d\vec{\xi}=\int_{-\infty}^{\infty}\left(\frac{\partial}{\partial t}f(\vec{r},\vec{\xi},t)+\vec{\xi}\frac{\partial f}{\partial\vec{r}}+\vec{F}\frac{\partial f}{\partial\vec{\xi}}\right)\psi\left(\vec{\xi}\right)d\vec{\xi}=0 \tag{2.4}$$

Substituting ψ with $m, m\vec{\xi}$ and $\frac{1}{2}m\xi^2$ in the previous expression and performing the integration using the integral expressions for the macroscopic quantities as presented in the next section we get the macroscopic conservation equations

$$\begin{aligned}
&\frac{1}{\rho}\left(\frac{\partial\rho}{\partial t}+\vec{U}\cdot\vec{\nabla}\rho\right)=-\vec{\nabla}\cdot\vec{U} && \text{mass conservation}\\
&\rho\left(\frac{\partial\vec{U}}{\partial t}+\vec{U}\cdot\vec{\nabla}\vec{U}\right)=\rho\vec{F}-\vec{\nabla}\cdot\vec{P} && \text{momentum conservation}\\
&\rho\left(\frac{\partial e}{\partial t}+\vec{U}\cdot\vec{\nabla}e\right)=-\vec{\nabla}\cdot\vec{Q}+\rho\vec{F}\cdot\vec{U}-\vec{P}:\vec{\nabla}\vec{U} && \text{energy conservation}
\end{aligned} \tag{2.5}$$

where ρ is the density, U is the macroscopic velocity, $\vec{F}$ is the force field, $\vec{P}$ is the stress tensor, e is the energy and $\vec{Q}$ is the heat flux vector. The previous equations are valid in the whole range of the Knudsen number. One of the reasons that the macroscopic approach fails to model rarefied flows is that the constitutive laws (e.q. Fourier's, Newton's and Fick's for the Navier-Stokes model) are not valid in those regimes.

A particular solution of the BE when no external forces are present $\left(\vec{F}=0\right)$ and for an equilibrium state $\left(\frac{\partial f}{\partial t}=0,\ \frac{\partial f}{\partial \vec{r}}=0\right)$ is the global Maxwellian distribution defined as [5]

$$f^{M}=\frac{N}{\left(2\pi\frac{k_B}{m}T\right)^{3/2}}\exp\left[-\frac{\left(\vec{\xi}-\vec{U}\right)^2}{2\frac{k_B}{m}T}\right] \tag{2.6}$$

where $N,T,\vec{U}$ are constants. The distribution of the same form when $N,T,\vec{U}$ are depended on t and $\vec{r}$ is the local Maxwellian distribution and does not satisfy the above mentioned special case of the BE in principal.

2.2 Macroscopic quantities

Macroscopic quantities of practical interest can be obtained as moments of the distribution function using the following expressions [5],[6]:

Number density $$N\left(\vec{r},t\right)=\int f\left(\vec{r},\vec{\xi},t\right)d\vec{\xi} \tag{2.7}$$

Velocity $$\vec{U}\left(\vec{r},t\right)=\frac{1}{N\left(\vec{r},t\right)}\int\vec{\xi}f\left(\vec{r},\vec{\xi},t\right)d\vec{\xi} \tag{2.8}$$

Stress tensor $$P_{ij}\left(\vec{r},t\right)=m\int\left(\xi_i-U_i\right)\left(\xi_j-U_j\right)f\left(\vec{r},\vec{\xi},t\right)d\vec{\xi} \tag{2.9}$$

Temperature $$T\left(\vec{r},t\right)=\frac{m}{3N\left(\vec{r},t\right)k_B}\int\left(\vec{\xi}-\vec{U}\right)^2 f\left(\vec{r},\vec{\xi},t\right)d\vec{\xi} \tag{2.10}$$

Heat flux $$\vec{Q}\left(\vec{r},t\right)=\frac{m}{2}\int\left(\vec{\xi}-\vec{U}\right)^2\left(\vec{\xi}-\vec{U}\right)f\left(\vec{r},\vec{\xi},t\right)d\vec{\xi} \tag{2.11}$$

H quantity $$H\left(\vec{r},t\right)=\int f\left(\vec{r},\vec{\xi},t\right)\ln\left[\frac{f\left(\vec{r},\vec{\xi},t\right)}{c_0}\right]d\vec{\xi} \tag{2.12}$$

where k_B is the Boltzmann constant and c_0 is a constant to make $\frac{f}{c_0}$ dimensionless. The H quantity may be related to entropy S and the so-called H-theorem to the second law of thermodynamics.

2.3 The BGK and Shakhov kinetic models

As mentioned the solution of the BE is a very demanding task that requires a lot of computational cost, mainly due to the fivefold integral on the right hand side. One way to overcome this difficulty is the substitution of the collision integral with expressions given by kinetic models.

The most basic and well know kinetic model is the BGK model [9]. It assumes that each molecule will be in the state of local equilibrium after only one collision. The mathematical expression of the BGK model is:

$$J(f)=\frac{P}{\mu}\left(f^M-f\right) \tag{2.13}$$

It has been extensively used to model isothermal single gas flows, with considerable success. It cannot model non isothermal flows though as it cannot provide the correct expressions for the viscosity and thermal conductivity coefficients simultaneously, as it yields for the Prandtl number $\mathrm{Pr}=1$ instead of $2/3$.

An extension of the BGK model, able to handle non isothermal flows is the Shakhov model [10], which has been used extensively in the present work. The mathematical expression is:

$$J(f)=\frac{P}{\mu}\left(f_{eq}^S-f\right) \tag{2.14}$$

where

$$f_{eq}^S=f^M\left[1+\frac{2}{5}\frac{m\left(1-\mathrm{Pr}\right)}{N\left(k_BT\right)^2}\vec{Q}\cdot\left(\vec{\xi}-\vec{U}\right)\left(\frac{m\left(\vec{\xi}-\vec{U}\right)^2}{2k_BT}-\frac{5}{2}\right)\right] \tag{2.15}$$

This model provides the correct value of the Prandtl number $\mathrm{Pr} = 2/3$, but is limited to single monatomic gas flows.

2.4 Boundary conditions

The boundary conditions for flows simulated using the BE are part of the solution. Their main objective is the correlation the distribution of the molecules departing from the boundary with that of the incoming molecules. The most widely used type of boundary condition is the Maxwell diffuse-specular. In the case of purely diffuse boundary conditions the distribution of molecules departing from the boundary is the local Maxwellian distribution characterized by the wall temperature and velocity. Specular reflection assumes that molecules arriving to the boundary collide with it in an elastic way, and are reflected without exchanging energy with the boundary. Taking $\vec{n}$ as a unit vector normal to the boundary with direction towards the flow field, we can denote the incoming distribution as $f^-\left(\vec{\xi}'\right)$ when $\vec{\xi}' \cdot \vec{n} < 0$ and the outgoing as $f^+\left(\vec{\xi}\right)$ when $\vec{\xi} \cdot \vec{n} > 0$. A general expression for the boundary conditions is [34]

$$f^+\left(\vec{\xi}\right) = -\int_{\vec{\xi}\cdot\vec{n}<0} \frac{\vec{\xi}' \cdot \vec{n}}{\vec{\xi} \cdot \vec{n}} W\left(\vec{\xi}' \to \vec{\xi}\right) f^-\left(\vec{\xi}'\right) d\vec{\xi}' \tag{2.16}$$

where $W\left(\vec{\xi}' \to \vec{\xi}\right)$ is the scattering kernel and is the probability that a molecule arriving at the boundary with velocity $\vec{\xi}'$ will depart with velocity $\vec{\xi}$.

In the case of specular reflection we expect that only the velocity component normal to the boundary will change, and will become the opposite, that is [5]

$$f^+\left(\vec{\xi}\right) = f^-\left(\vec{\xi} - 2\left(\vec{\xi} \cdot \vec{n}\right)\vec{n}\right) \tag{2.17}$$

leading to the scattering kernel

$$W_s\left(\vec{\xi}' \to \vec{\xi}\right) = \delta\left[\vec{\xi}' - \vec{\xi} + 2\left(\vec{\xi} \cdot \vec{n}\right)\vec{n}\right] \tag{2.18}$$

where δ is the Dirac function according to $\int \delta\left(\vec{r} - \vec{a}\right)\varphi\left(\vec{r}\right) d\vec{r} = \varphi\left(\vec{\alpha}\right)$.

In the case of purely diffuse boundary conditions, the outgoing distribution is the local Maxwellian characterized by the wall conditions,

$$f^{+}\left(\vec{\xi}\right)=N_{w}\left(\frac{m}{2k_{B}\pi T_{w}}\right)^{3/2}\exp\left[-\frac{m\left(\vec{\xi}-\overrightarrow{U_{W}}\right)^{2}}{2k_{B}T_{W}}\right] \tag{2.19}$$

where T_W is the wall temperature $\overrightarrow{U_w}$ is the wall velocity and N_w is a parameter ensuring the impermeability condition. The above expression gives the scattering kernel

$$W_{d}\left(\vec{\xi}'\rightarrow\vec{\xi}\right)=\frac{1}{2\pi}\vec{\xi}\cdot\vec{n}\left(\frac{m}{k_{B}T_{w}}\right)^{3/2}\exp\left[-\frac{m\left(\vec{\xi}-\overrightarrow{U_{W}}\right)}{2k_{B}T_{W}}\right] \tag{2.20}$$

In practice the boundary interaction is not purely specular neither purely diffusive. It is more accurate to assume that a portion a of the molecules is reflected diffusively and the remaining $(1-a)$ undergoes specular reflection, leading to the diffuse-specular scattering kernel

$$W\left(\vec{\xi}'\rightarrow\vec{\xi}\right)=aW_{d}\left(\vec{\xi}'\rightarrow\vec{\xi}\right)+(1-a)W_{s}\left(\vec{\xi}'\rightarrow\vec{\xi}\right) \tag{2.21}$$

where a is the accommodation coefficient.

One drawback of the diffuse-specular scattering kernel is that the probability of a molecule reflecting according to specular or diffusive reflection is independent of the velocity magnitude and direction. The Epstein scattering kernel overcomes this drawback, but was criticized as the coefficients used in it are chosen empirically [35].

2.5 Deterministic solution of model kinetic equations

Several methods have been developed for the solution of the Boltzmann and model equations. In this work the discrete velocity method has been used. In the discrete velocity method the continuous spectrum of molecular velocities is replaced by a discrete set of velocities, accordingly chosen in order to achieve good accuracy. Since the molecular velocity takes discrete values it is possible to replace the Boltzmann or model equation with a set of partial integrodifferential equations with the physical space coordinates being the free variables.

This method has been extensively used over the years to solve the kinetic model equations. It was initially applied to simple, one dimensional geometries for linearized equations [36],[37]. The Poiseuille and Couette flows for parallel plates where simulated for small

pressure gradients and wall velocities respectively, as well as the Poiseuille flow between concentrical cylinders. It was also applied to linear heat transfer problems between plates and cylinders. Later two dimensional geometries were simulated, for linear cases [38-[45], such as the driven cavity flow and flows through ducts of different cross sections . Moreover, non-linear flows have been successfully simulated using the discrete velocity method, in one-dimensional cases such as the heat transfer between coaxial cylinders [46]. Two dimensional nonlinear flows where this method was successfully applied include pressure driven flows through slits, orifices and tubes [47],[48].

Considerable effort has been made over the years in order to make this method more efficient. One approach is to implement a conservative scheme as described in [49]. In such a numerical scheme the macroscopic quantities calculated at the end of each time step are corrected so that they satisfy the conservation equations. When a trivial numerical scheme is implemented, dense computational grids have to be used in order to ensure that the conservation principals are not violated. Using the conservative scheme requires more computational effort per iteration than a trivial scheme, but since coarse grids can be used without lack in accuracy, the overall CPU time requirement is decreased.

Another approach is to use the so-called accelerated form of the equations, as described in [50]. In this delicate approach the kinetic equation is substituted by a system of equations, its size depending on the number of moments to be calculated, and this system is iteratively solved. One of the equations is in non-accelerated form, meaning that the computational effort for this equation alone is comparable to the computational effort for the trivial scheme. It is apparent that since the whole system of equations has to be solved, the computational effort per iteration is increased, but the number of iterations required for convergence is dramatically decreased. An interesting point is that the greatest improvements were noticed in near hydrodynamic cases, a regime where the trivial scheme has a very slow convergence rate.

Chapter 3 Problem description and formulation

3.1 Flow configuration

The present work is focused in the simulation of temperature driven cavity flows through kinetic theory. The Shakhov model equation [10] was used, as it provides the correct viscosity and thermal conductivity coefficients, in contrast with the BGK. The Shakhov model has been proven to be a reliable model for non-isothermal flows [51-[55]. The parameters characterizing the flow are the Knudsen number, the temperature ratio of the cold over the hot walls, the aspect ratio H/W of the cavity and the IPL parameter. The macroscopic quantities of interest are the temperature $T(x',y')$ and density $N(x',y')$ distributions, the velocity $\vec{U}(x',y')$ and heat flux $\vec{Q}(x',y')$ vectors and the stress tensor $P_{ij}(x',y')$.

It is convenient here to introduce the following non-dimentionlization:

$$
\begin{aligned}
&x=\frac{x'}{W},\ y=\frac{y'}{W},\ \tau=\frac{T}{T_0},\ n=\frac{N}{N_0},\ N_0=\frac{1}{HW}\int_{-W/2}^{W/2}\int_{0}^{H}N(x',y')dx'dy' \\
&\vec{u}=\frac{\vec{U}}{u_0},\ \vec{\zeta}=\frac{\vec{\xi}}{u_0},\ u_0=\sqrt{2\frac{k_B}{m}T_0},\ \vec{q}=\frac{\vec{Q}}{N_0k_BT_0u_0},\ p_{ij}=\frac{P_{ij}}{N_0k_BT_0},\ h=\frac{H}{N_0}
\end{aligned}
\tag{3.1}
$$

where N_0 is the average density and u_0 is the most probable molecular velocity.

The cross section of the cavity along with the geometric parameters, the origin of the coordinate system and the flow structure are shown in Figure 3. Four different cavity configurations were simulated. In the first configuration, Figure 4a, the right half of the boundaries $(x>0)$ is kept at a high temperature T_H while the rest is at a lower temperature T_C. This case has already been investigated in [25] and the results were used to benchmark the code. Two types of vortices were observed, type-I rotating so that the velocity in the vicinity of the horizontal walls is from cold to hot, and type-II counter-rotating to type-I

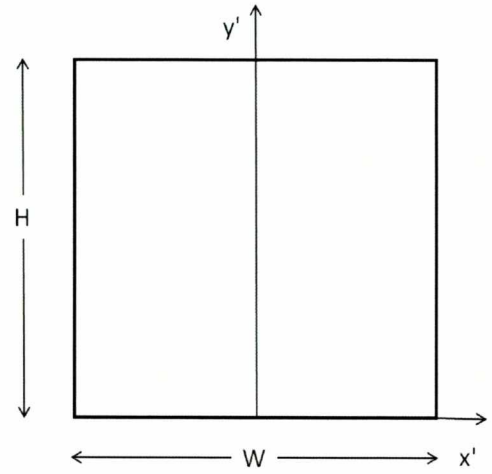

Figure 3: View of the cavity and the axes origin.

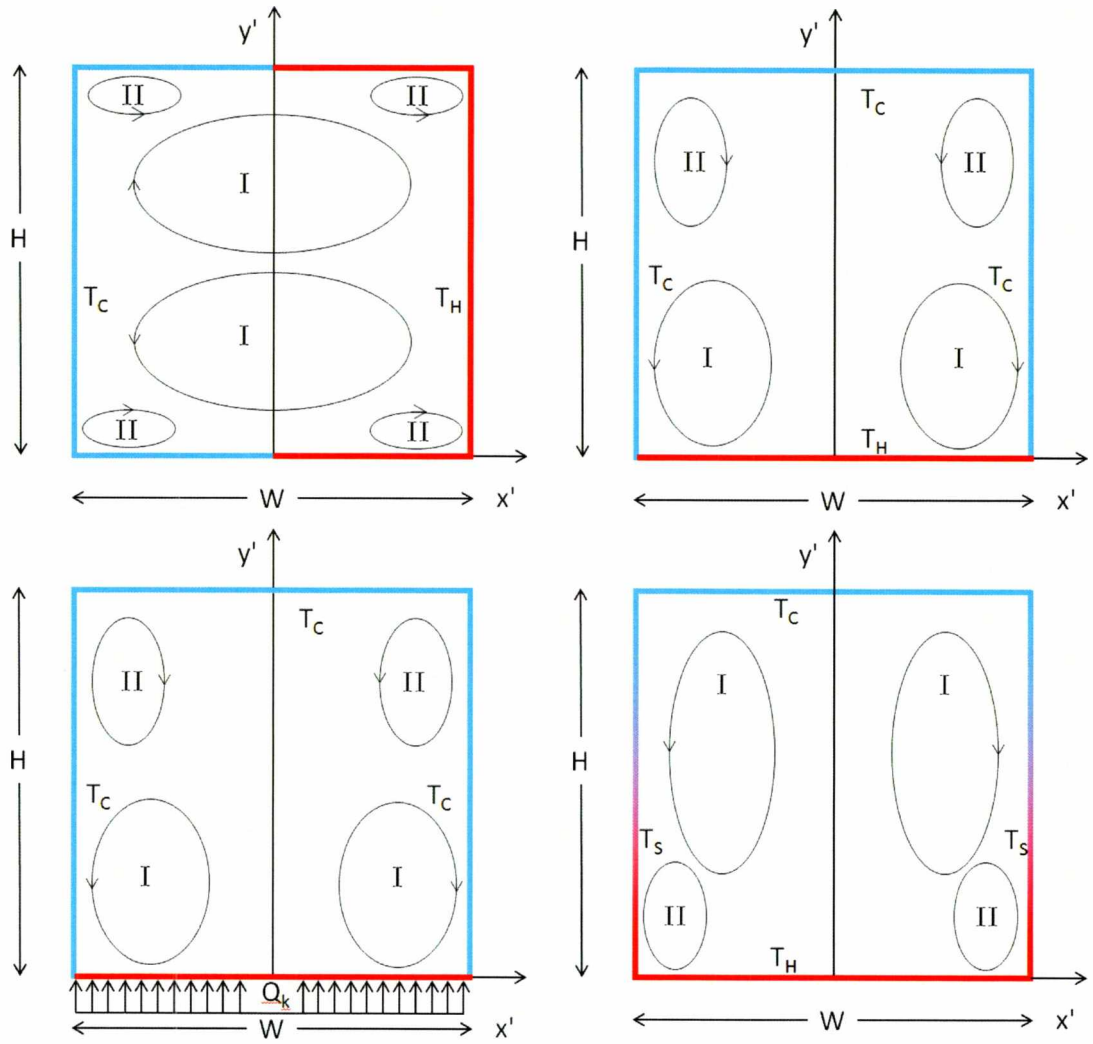

Figure 4: The four different cavity configurations simulated.

vortices. In the second case, Figure 4b, the bottom wall of the cavity is kept at a high temperature T_H, while the other three walls are at a lower temperature T_C. The third case, Figure 4c, is similar to the second, except that the bottom wall temperature is unknown and the heat flux is known. In both of those cases two types of vortices appear, type-I vortices having velocity in the vicinity of the bottom walls directed from cold to hot, and type-II counter-rotating to them. In the fourth case, Figure 4d, the bottom wall is at a high temperature T_H, the top wall is at lower temperature T_C, while the lateral walls have a linear temperature distribution between T_H and T_C according to $T_S = T_H - (T_H - T_C)\, y'/H$. Again, two types of vortices are present, types I and II, with velocities in the vicinity of the lateral walls heading from cold-to-hot and from hot-to-cold respectively.

3.2 Governing equations

The nonlinear steady-state two dimensional Shakhov model equation is

$$\xi_x \frac{\partial f}{\partial x'} + \xi_y \frac{\partial f}{\partial y'} = \frac{P}{\mu}\left(f^s - f\right) \tag{3.2}$$

where P is the local pressure, $\mu = \mu(T)$ is the viscosity at local temperature T and

$$f^S = f^M \left[1 + \frac{2}{15} \frac{m}{N\left(k_B T\right)^2} \vec{Q} \cdot \left(\vec{\xi} - \vec{U}\right) \left(\frac{m\left(\vec{\xi} - \vec{U}\right)^2}{2k_B T} - \frac{5}{2} \right) \right] \tag{3.3}$$

with

$$f^M = \frac{N}{\left(2\pi \frac{k_B}{m} T\right)^{3/2}} \exp\left[- \frac{m\left(\vec{\xi} - \vec{U}\right)^2}{2k_B T} \right] \tag{3.4}$$

being the local Maxwellian. Introducing the dimensionless distribution function $g = f u_0^3 / N_0$ along with the non-dimensional variables of Eq. (3.1) the reference Knudsen number as

$$Kn_0 = \frac{\sqrt{\pi}}{2} \frac{\mu_0 u_0}{P_0 W} \tag{3.5}$$

and the IPL molecular interaction model [7] that yields a viscosity of the form $\mu = \mu_0 \left(\frac{\mathrm{T}}{\mathrm{T}_0} \right)^{\omega}$, with $\omega \in [0.5,1]$ where $\omega = 0.5$ and $\omega = 1$ correspond to the limiting cases of Hard Sphere and Maxwell molecules respectively, we get the non-dimensional form of the Shakhov model equation:

$$c_x \frac{\partial g}{\partial x} + c_y \frac{\partial g}{\partial y} = \frac{1}{Kn_0} \frac{\sqrt{\pi}}{2} n\tau^{1-\omega} \left(g^s - g \right) \tag{3.6}$$

$$g^S = g^M \left[1 + \frac{4}{15} \frac{1}{n\tau^2} \vec{q} \cdot \left(\vec{\zeta} - \vec{u} \right) \left(\frac{\left(\vec{\zeta} - \vec{u} \right)^2}{\tau} - \frac{5}{2} \right) \right] \tag{3.7}$$

$$g^M = \frac{n}{\left(\pi\tau \right)^{3/2}} \exp\left[- \frac{\left(\vec{\zeta} - \vec{u} \right)^2}{\tau} \right] \tag{3.8}$$

To close the problem the above integrodifferential equation must accompanied by the boundary conditions and the expressions for the macroscopic quantities. The integral expressions for the macroscopic properties are derived through Eqs. (2.7)-(2.12) and are given by:

Number density $$n = \int g d\vec{\zeta} \tag{3.9}$$

Velocity $$\vec{u} = \frac{1}{n} \int \vec{\zeta} g d\vec{\zeta} \tag{3.10}$$

Stress tensor $$p_{ij}\left(\vec{r}, t \right) = 2 \int \left(\zeta_i - u_i \right) \left(\zeta_j - u_j \right) g d\vec{\zeta} \tag{3.11}$$

Temperature $$\tau = \frac{2}{3n} \int \left(\vec{\zeta} - \vec{u} \right)^2 g d\vec{\zeta} \tag{3.12}$$

Heat flux $$\vec{q} = \int \left(\vec{\zeta} - \vec{u} \right)^2 \left(\vec{\zeta} - \vec{u} \right) g d\vec{\zeta} \tag{3.13}$$

H quantity $$h\left(\vec{r}, t \right) = \int g \ln[g] d\vec{\zeta} \tag{3.14}$$

In (3.14) c_0 has been constituted by N_0 / u_0^3 .

Here the Maxwell diffuse specular boundary conditions were used, in the dimensionless form [8]

$$g^{+}\left(x,y,\zeta_x,\zeta_y,\zeta_z\right)=ag^{M}+(1-a)g^{-}\left(x,y,\zeta_x-2\vec{n}\cdot\vec{\zeta}_x,\zeta_y-2\vec{n}\cdot\vec{\zeta}_y,\zeta_z\right) \tag{3.15}$$

where g^{+} is the outgoing distribution, g^{-} is the incoming distribution and $\vec{n}$ is the unit vector perpendicular to the wall. For each of the four walls, and assuming pure diffuse reflection the above boundary condition becomes

$$g^{+}_{bottom}\left(x,0,\zeta_x,\zeta_y,\zeta_z\right)=\frac{n_w^{bottom}}{\left(\pi\tau_w^{bottom}\right)^{3/2}}\exp\left[-\frac{\left(\vec{\zeta}-\overrightarrow{u_w^{bottom}}\right)^2}{\tau_w^{bottom}}\right]$$

$$g^{+}_{top}\left(x,1,\zeta_x,\zeta_y,\zeta_z\right)=\frac{n_w^{top}}{\left(\pi\tau_w^{top}\right)^{3/2}}\exp\left[-\frac{\left(\vec{\zeta}-\overrightarrow{u_w^{top}}\right)^2}{\tau_w^{top}}\right]$$

$$g^{+}_{left}\left(-\frac{1}{2},y,\zeta_x,\zeta_y,\zeta_z\right)=\frac{n_w^{left}}{\left(\pi\tau_w^{left}\right)^{3/2}}\exp\left[-\frac{\left(\vec{\zeta}-\overrightarrow{u_w^{left}}\right)^2}{\tau_w^{left}}\right] \tag{3.16}$$

$$g^{+}_{right}\left(\frac{1}{2},y,\zeta_x,\zeta_y,\zeta_z\right)=\frac{n_w^{right}}{\left(\pi\tau_w^{right}\right)^{3/2}}\exp\left[-\frac{\left(\vec{\zeta}-\overrightarrow{u_w^{right}}\right)^2}{\tau_w^{right}}\right]$$

The parameter n_w is computed in terms of the incoming distribution, in order to satisfy the impermeability condition:

$$\vec{u}\cdot\vec{n}=0\Rightarrow\int_{R^3}\vec{\zeta}\cdot\vec{n}\,g\,d\vec{\zeta}=0\Rightarrow\int_{\vec{\zeta}\cdot\vec{n}>0}\vec{\zeta}\cdot\vec{n}\,g^{+}\,d\vec{\zeta}+\int_{\vec{\zeta}\cdot\vec{n}<0}\vec{\zeta}\cdot\vec{n}\,g^{-}\,d\vec{\zeta}=0 \tag{3.17}$$

In the case of known heat flux at a boundary the temperature τ_w of the boundary is not known and has to be calculated along with the n_w parameter using the following expressions:

$$\begin{aligned}&\vec{u}\cdot\vec{n}=0\Rightarrow\int_{\vec{\zeta}\cdot\vec{n}>0}\vec{\zeta}\cdot\vec{n}\,g^{+}\,d\vec{\zeta}+\int_{\vec{\zeta}\cdot\vec{n}<0}\vec{\zeta}\cdot\vec{n}\,g^{-}\,d\vec{\zeta}=0\\&\vec{q}=\vec{q}_w\Rightarrow\int_{\vec{\zeta}\cdot\vec{n}>0}\left(\vec{\zeta}-\vec{u}\right)^2\left(\vec{\zeta}-\vec{u}\right)g^{+}\,d\vec{c}+\int_{\vec{\zeta}\cdot\vec{n}<0}\left(\vec{\zeta}-\vec{u}\right)^2\left(\vec{\zeta}-\vec{u}\right)g^{-}\,d\vec{\zeta}=\vec{q}_w\end{aligned} \tag{3.18}$$

The above equations are coupled as both τ_w and n_w appear in the outgoing distribution term.

3.3 Projection procedure

Although the problem is two-dimensional in the physical space Eq. (3.6) is five dimensional as $g = g\left(x, y, c_x, c_y, c_z\right)$. To reduce the computational cost it is possible to eliminate the c_z component of the molecular velocity using the projection procedure. During this procedure the Shakhov equation, the boundary conditions and the integral expressions for the macroscopic quantities are integrated all over c_z resulting in a system for two reduced distribution functions. This procedure is irreversible as information is lost during the integration, but due to the symmetry in the z-direction the lost information is of no practical interest. The two reduced distribution functions are:

$$\varphi\left(x, y, \zeta_x, \zeta_y\right) = \int_R g d\zeta_z \tag{3.19}$$

$$\psi\left(x, y, \zeta_x, \zeta_y\right) = \int_R \zeta_z^2 g d\zeta_z \tag{3.20}$$

Applying the projection procedure to Eqs. (3.6)-(3.14) the following expressions are deduced:

$$\zeta_x \frac{\partial \varphi}{\partial x} + \zeta_y \frac{\partial \varphi}{\partial y} = \frac{1}{Kn} \frac{\sqrt{\pi}}{2} n\tau^{1-\omega}\left(\varphi^s - \varphi\right) \tag{3.21}$$

$$\zeta_x \frac{\partial \psi}{\partial x} + \zeta_y \frac{\partial \psi}{\partial y} = \frac{1}{Kn} \frac{\sqrt{\pi}}{2} n\tau^{1-\omega}\left(\psi^s - \psi\right) \tag{3.22}$$

where

$$\varphi^S = \varphi^M \left[1 + \frac{4}{15} \frac{1}{n\tau^2} \vec{q} \cdot \left(\vec{\zeta} - \vec{u}\right) \left(\frac{\left(\vec{\zeta} - \vec{u}\right)^2}{\tau} - 2 \right)\right] \tag{3.23}$$

$$\psi^S = \psi^M \left[1 + \frac{4}{15} \frac{1}{n\tau^2} \vec{q} \cdot \left(\vec{\zeta} - \vec{u}\right) \left(\frac{\left(\vec{\zeta} - \vec{u}\right)^2}{\tau} - 1 \right)\right] \tag{3.24}$$

with

$$\varphi^M = \frac{n}{\pi\tau} \exp\left[-\frac{\left(\vec{\zeta} - \vec{u}\right)^2}{\tau} \right] \tag{3.25}$$

$$\psi^M = \frac{n}{2\pi}\exp\left[-\frac{\left(\vec{\zeta}-\vec{u}\right)^2}{\tau}\right] \tag{3.26}$$

The expressions for the macroscopic quantities become

Number density $$n = \int \varphi d\vec{\zeta} \tag{3.27}$$

Velocity $$\vec{u} = \frac{1}{n}\int \vec{c}\varphi d\vec{\zeta} \tag{3.28}$$

Shear Stress $$p_{xy}\left(\vec{r},t\right) = 2\int\left(\zeta_x - u_x\right)\left(\zeta_y - u_y\right)\varphi d\vec{\zeta} \tag{3.29}$$

Temperature $$\tau = \frac{2}{3n}\int\left(\left(\zeta_x^2+\zeta_y^2\right)\varphi+\psi\right)d\vec{\zeta} - \frac{2}{3}\left(u_x^2+u_y^2\right) \tag{3.30}$$

Heat flux $$\vec{q} = \int\left(\left(\vec{\zeta}-\vec{u}\right)^2\varphi+\psi\right)\left(\vec{\zeta}-\vec{u}\right)d\vec{\zeta} \tag{3.31}$$

H quantity $$h\left(\vec{r},t\right) = \int\varphi\ln\left[\frac{\varphi}{\sqrt{\pi\tau}}\right]d\vec{\zeta} - \frac{1}{2}n \tag{3.32}$$

In order to express the h quantity in terms of the reduced distribution function, we assume that due to the equilibrium in the z direction the distribution function can be expressed as [29] $g = g_{x,y}g_z$, where $g_z = \frac{1}{\sqrt{\pi\tau}}\exp\left[-\frac{\zeta_z^2}{\tau}\right]$. Using Eq. (3.19) for the reduced distribution function we get

$$\varphi = \int_{-\infty}^{\infty} g d\zeta_z \Rightarrow \varphi = \int_{-\infty}^{\infty} g_{x,y}g_z d\zeta_z \Rightarrow \varphi = g_{x,y}\underbrace{\int_{-\infty}^{\infty}\frac{1}{\sqrt{\pi\tau}}\exp\left[-\frac{\zeta_z^2}{\tau}\right]d\zeta_z}_{1} \Rightarrow \varphi = g_{x,y}.$$

Substituting $g = \frac{\varphi}{\sqrt{\pi\tau}}\exp\left[-\frac{\zeta_z^2}{\tau}\right]$ into Eq. (3.14) we get Eq. (3.32) after some routine manipulation.

The expressions for the boundary conditions become:

$$\varphi^+ = \varphi^M = \frac{n_w}{\pi\tau_w}\exp\left[-\frac{\left(\vec{\zeta}-\vec{u_w}\right)^2}{\tau_w}\right] \tag{3.33}$$

$$\psi^{+} = \psi^{M} = \frac{n_w}{2\pi} \exp\left[-\frac{\left(\vec{\zeta} - \vec{u_w}\right)^2}{\tau_w} \right] \tag{3.34}$$

In the case of known heat flux

$$\vec{u} \cdot \vec{n} = 0 \Rightarrow \int\limits_{\vec{\zeta} \cdot \vec{n} > 0} \vec{\zeta} \cdot \vec{n}\ \varphi^{+}\ d\vec{\zeta} + \int\limits_{\vec{\zeta} \cdot \vec{n} < 0} \vec{\zeta} \cdot \vec{n}\ \varphi^{-}\ d\vec{\zeta} = 0$$

$$\vec{q} = \vec{q}_w \Rightarrow \int\limits_{\vec{\zeta} \cdot \vec{n} > 0} \left[\left(\vec{\zeta} - \vec{u}\right)^2 \varphi^{+} + \psi^{+} \right] \left(\vec{\zeta} - \vec{u}\right)\ d\vec{\zeta} + \int\limits_{\vec{\zeta} \cdot \vec{n} < 0} \left[\left(\vec{\zeta} - \vec{u}\right)^2 \varphi^{-} + \psi^{-} \right] \left(\vec{\zeta} - \vec{u}\right)\ d\vec{\zeta} = \vec{q}_w$$

This boundary condition is applied to the bottom wall of the cavity to get

$$u_y = 0 \Rightarrow \int\limits_{\zeta_y > 0} \zeta_y\ \varphi^{+}\ d\vec{\zeta} + \int\limits_{\zeta_y < 0} \zeta_y\ \varphi^{-}\ d\vec{\zeta} = 0$$

$$q_y = q_w \Rightarrow \int\limits_{\zeta_y > 0} \left[\left(\vec{\zeta} - \vec{u}\right)^2 \varphi^{+} + \psi^{+} \right] \left(\zeta_y - u_y\right)\ d\vec{\zeta} + \int\limits_{\zeta_y < 0} \left[\left(\vec{\zeta} - \vec{u}\right)^2 \varphi^{-} + \psi^{-} \right] \left(\zeta_y - u_y\right)\ d\vec{\zeta} = q_w$$

Substituting the expressions for the outgoing distribution, setting the wall velocity to 0 and performing the integrations, we get

$$\tau_w^{bottom} = \frac{1}{2}\left(\frac{B - q_w}{A} - u_x^2 \right) \text{ and } n_w^{bottom} = -2A\sqrt{\frac{\pi}{\tau_w^{bottom}}} \tag{3.35}$$

where

$$A = \int\limits_{-\infty}^{0} \int\limits_{-\infty}^{\infty} \mathrm{c}_y\ \varphi^{-}\ dc_x dc_y \text{ and } B = \int\limits_{-\infty}^{0} \int\limits_{-\infty}^{\infty} \left[\left(\vec{\zeta} - \vec{u}\right)^2 \varphi^{-} + \psi^{-} \right] \left(\zeta_y - u_y\right) d\zeta_x d\zeta_y \tag{3.36}$$

3.4 Discretization

For the molecular velocity space discretization the discrete velocity method has been used. It is computationally efficient to present the velocity vector in polar coordinates according to $\zeta_x = c\cos(\theta)$ and $\zeta_y = c\sin(\theta)$. The continuum spectrum of molecular velocities (c, θ) is replaced by a set of discrete velocities (c_m, θ_n) where $c_m \in (0, \infty)$, $m = 1, 2, ..., M$ and $\theta_n \in (0, 2\pi)$, $n = 1, 2, ..., N$. The magnitudes c_m are taken to be the roots of the Legendre polynomial of order M accordingly mapped form $(-1, 1)$ to $(0, \infty)$, while the polar angles

are $\theta_n = \pi(2n-1)/N$. The implemented deterministic algorithm has been repeatedly applied to solve nonlinear flows and heat transfer problems with considerable success [48],[56], [57].

For the physical space discretization a second order finite volume scheme is used [57]. The flow domain is divided into $I \times J$ rectangular elements. Upon the molecular velocity space discretization the deduced equations are integrated over each space element defined by $\left[x_{i-1/2}, x_{i+1/2}\right]$ and $\left[y_{j-1/2}, y_{j+1/2}\right]$. After this procedure the discretized equations are:

$$\varphi^{(\kappa+1/2)}_{i+1/2,j+1/2,m,n} Td11 + \varphi^{(\kappa+1/2)}_{i+1/2,j-1/2,m,n} Td10 + \varphi^{(\kappa+1/2)}_{i-1/2,j+1/2,m,n} Td01 + \varphi^{(\kappa+1/2)}_{i-1/2,j-1/2,m,n} Td00 = RHS\varphi \tag{3.37}$$

$$\psi^{(\kappa+1/2)}_{i+1/2,j+1/2,m,n} Td11 + \psi^{(\kappa+1/2)}_{i+1/2,j-1/2,m,n} Td10 + \psi^{(\kappa+1/2)}_{i-1/2,j+1/2,m,n} Td01 + \psi^{(\kappa+1/2)}_{i-1/2,j-1/2,m,n} Td00 = RHS\psi \tag{3.38}$$

where

$$\begin{aligned}
Td00 &= -\frac{c_m \cos\theta_n}{2\Delta x} - \frac{c_m \sin\theta_n}{2\Delta y} + \frac{1}{4}\left(\frac{1}{Kn_0}\frac{\sqrt{\pi}}{2} n\tau^{1-\omega}\right)^{(k)}_{i-1/2,j-1/2} \\
Td01 &= -\frac{c_m \cos\theta_n}{2\Delta x} + \frac{c_m \sin\theta_n}{2\Delta y} + \frac{1}{4}\left(\frac{1}{Kn_0}\frac{\sqrt{\pi}}{2} n\tau^{1-\omega}\right)^{(k)}_{i-1/2,j+1/2} \\
Td10 &= +\frac{c_m \cos\theta_n}{2\Delta x} - \frac{c_m \sin\theta_n}{2\Delta y} + \frac{1}{4}\left(\frac{1}{Kn_0}\frac{\sqrt{\pi}}{2} n\tau^{1-\omega}\right)^{(k)}_{i+1/2,j-1/2} \\
Td11 &= +\frac{c_m \cos\theta_n}{2\Delta x} + \frac{c_m \sin\theta_n}{2\Delta y} + \frac{1}{4}\left(\frac{1}{Kn_0}\frac{\sqrt{\pi}}{2} n\tau^{1-\omega}\right)^{(k)}_{i+1/2,j+1/2}
\end{aligned} \tag{3.39}$$

$$\begin{aligned}
RHS\varphi = \frac{1}{4}\Bigg[&\left(\frac{1}{Kn_0}\frac{\sqrt{\pi}}{2} n\tau^{1-\omega}\varphi^S\right)^{(k)}_{i+1/2,j+1/2,m,n} + \left(\frac{1}{Kn_0}\frac{\sqrt{\pi}}{2} n\tau^{1-\omega}\varphi^S\right)^{(k)}_{i+1/2,j-1/2,m,n} + \\
&+\left(\frac{1}{Kn_0}\frac{\sqrt{\pi}}{2} n\tau^{1-\omega}\varphi^S\right)^{(k)}_{i-1/2,j+1/2,m,n} + \left(\frac{1}{Kn_0}\frac{\sqrt{\pi}}{2} n\tau^{1-\omega}\varphi^S\right)^{(k)}_{i-1/2,j-1/2,m,n}\Bigg]
\end{aligned} \tag{3.40}$$

$$\begin{aligned}
RHS\psi = \frac{1}{4}\Bigg[&\left(\frac{1}{Kn_0}\frac{\sqrt{\pi}}{2} n\tau^{1-\omega}\psi^S\right)^{(k)}_{i+1/2,j+1/2,m,n} + \left(\frac{1}{Kn_0}\frac{\sqrt{\pi}}{2} n\tau^{1-\omega}\psi^S\right)^{(k)}_{i+1/2,j-1/2,m,n} + \\
&+\left(\frac{1}{Kn_0}\frac{\sqrt{\pi}}{2} n\tau^{1-\omega}\psi^S\right)^{(k)}_{i-1/2,j+1/2,m,n} + \left(\frac{1}{Kn_0}\frac{\sqrt{\pi}}{2} n\tau^{1-\omega}\psi^S\right)^{(k)}_{i-1/2,j-1/2,m,n}\Bigg]
\end{aligned} \tag{3.41}$$

where k is the iteration index.

The macroscopic quantities are calculated through expressions $(3.27-3.32)$. The integrals are estimated using the Gauss-Legendre quadrature for the velocity magnitude integration and the trapezoidal rule for the polar angle integration. The discrete expressions derived are:

Number density
$$n_{i,j}^{(k+1)} = \sum_{m=1}^{M}\sum_{n=1}^{N}\varphi_{i,j,m,n}^{(k+1/2)} w_m \Delta\theta \tag{3.42}$$

Velocity
$$u_{x\,\mathrm{i,j}}^{(k+1)} = \frac{1}{n_{i,j}}\sum_{m=1}^{M}\sum_{n=1}^{N} c_m \cos\theta_n \varphi_{i,j,m,n}^{(k+1/2)} w_m \Delta\theta \tag{3.43}$$

$$u_{\mathrm{y\,i,j}}^{(k+1)} = \frac{1}{n_{i,j}}\sum_{m=1}^{M}\sum_{n=1}^{N} c_m \sin\theta_n \varphi_{i,j,m,n}^{(k+1/2)} w_m \Delta\theta \tag{3.44}$$

Shear stress
$$p_{xy,i,j}^{(k+1)} = 2\sum_{m=1}^{M}\sum_{n=1}^{N}\left(c_m\cos\theta_n - u_{x\,\mathrm{i,j}}\right)\left(c_m\sin\theta_n - u_{\mathrm{y\,i,j}}\right)\varphi_{i,j,m,n}^{(k+1/2)} w_m \Delta\theta \tag{3.45}$$

Temperature
$$\tau_{i,j}^{(k+1)} = \frac{2}{3n_{i,j}}\sum_{m=1}^{M}\sum_{n=1}^{N}\left(c_m^2\varphi_{i,j,m,n}^{(k+1/2)} + \psi_{i,j,m,n}^{(k+1/2)}\right) w_m \Delta\theta - \frac{2}{3}\left(u_{x\,\mathrm{i,j}}^2 + u_{y\,\mathrm{i,j}}^2\right) \tag{3.46}$$

Heat flux

$$q_{x\,i,j}^{(k+1)} = \sum_{m=1}^{M}\sum_{n=1}^{N}\left[\left[\left(c_m\cos\theta_n - u_{xi,j}\right)^2 + \left(c_m\sin\theta_n - u_{yi,j}\right)^2\right]\varphi_{i,j,m,n}^{(k+1/2)} + \psi_{i,j,m,n}^{(k+1/2)}\right]\left(c_m\cos\theta_n - u_{xi,j}\right) w_m\Delta\theta \tag{3.47}$$

$$q_{\mathrm{y}\,i,j}^{(k+1)} = \sum_{m=1}^{M}\sum_{n=1}^{N}\left[\left[\left(c_m\cos\theta_n - u_{xi,j}\right)^2 + \left(c_m\sin\theta_n - u_{yi,j}\right)^2\right]\varphi_{i,j,m,n}^{(k+1/2)} + \psi_{i,j,m,n}^{(k+1/2)}\right]\left(c_m\sin\theta_n - u_{yi,j}\right) w_m\Delta\theta \tag{3.48}$$

H quantity
$$h_{i,j}^{(k+1)} = \sum_{m=1}^{M}\sum_{n=1}^{N}\varphi_{i,j,m,n}^{(k+1/2)} \ln\left[\frac{\varphi_{i,j,m,n}^{(k+1/2)}}{\sqrt{\pi\tau_{i,j}}}\right] w_m\Delta\theta - \frac{1}{2}n_{i,j} \tag{3.49}$$

In the above expressions w_m and $\Delta\theta$ are the weights associated with the velocity magnitude and polar angle integrations respectively.

The simulation stops when a convergence criteria given by

$$\varepsilon^{(k)} = \max_{i,j}\left\{\left|n_{i,j}^{(k)} - n_{i,j}^{(k-1)}\right| + \left|u_{x\,i,j}^{(k)} - u_{x\,i,j}^{(k-1)}\right| + \left|u_{\mathrm{y}\,i,j}^{(k)} - u_{\mathrm{y}\,i,j}^{(k-1)}\right| + \left|\tau_{i,j}^{(k)} - \tau_{i,j}^{(k-1)}\right|\right\} < error \tag{3.50}$$

where "$error$" is chosen empirically, is fulfilled.

A known issue with the boundary conditions used is that they are always discontinuous at the corners of the flow domain. This is because the n_w parameters calculated for the same corner node but for a different wall, e.g. $n_{w,1}^{bottom}$ and $n_{w,1}^{left}$ for the bottom left corner, are different. In order to overcome this difficulty we do not calculate the n_w parameters of the corners directly using the integral expressions derived, but they are estimated using an extrapolation for each wall, and the two different parameters estimated this way are averaged as show bellow:

$$n_{w,2}^{bottom} = \frac{n_{w,1}^{bottom} + n_{w,3}^{bottom}}{2} \Rightarrow n_{w,1}^{bottom} = 2n_{w,2}^{bottom} - n_{w,3}^{bottom}$$

$$n_{w,2}^{left} = \frac{n_{w,1}^{left} + n_{w,3}^{left}}{2} \Rightarrow n_{w,1}^{left} = 2n_{w,2}^{left} - n_{w,3}^{left}$$

$$n_{w,1}^{bottom} = n_{w,1}^{left} = \frac{n_{w,1}^{bottom} + n_{w,1}^{left}}{2} = \frac{2\left(n_{w,2}^{bottom} + n_{w,2}^{left}\right) - \left(n_{w,3}^{bottom} + n_{w,3}^{left}\right)}{2}$$

the same procedure is done for the density and temperature as well.

In closed domain flows the total mass of the gas has to remain constant throughout the simulation. A problem that came up with this configuration is that since the boundary conditions are part of the solution, the initial estimation can be far from the final solution and during the first few iterations of the code the velocity normal to the walls is not necessarily zero. This causes an artificial mass flow rate through the boundaries and the final mass in the cavity is not the same as the initial. To overcome this, in the first few iterations we calculate the average dimensionless number density in the cavity and normalize the number density of each node with this average. Another possible solution is to obtain the n_w parameters analytically for the free molecular limit and use those values of n_w as an initial guess. This way the mass is conserved at high reference Knudsen numbers, but as the Knudsen number is decreased the final values of n_w become much different from the initial guess and the same problem arises. A final solution is to start from an initial guess, iterate for a few iterations and initialize the problem using the calculated values of n_w as the new initial guess. Repeating this procedure several times the initial values of the n_w converges and the code is allowed to carry on with the simulation of the flow. This procedure however comes with a considerable computational cost.

Chapter 4 Decomposition of the distribution function

4.1 Introduction

In general the distribution at each point of the flow domain consists of particles arriving from the domain boundaries without any collisions with other particles and particles arriving after an arbitrary number of collisions with other particles. The former part of the distribution function is named ballistic part and the latter collision part. In this chapter a method is introduced for the decomposition of the distribution function into these two parts. The two parts of the solution are named this way to distinguish this from other decompositions proposed, such as the splitting in the free molecular and collisional parts. These decompositions are used because they offer either less computational effort, or improved accuracy in certain formulations, especially in formulations with strong boundary induced discontinuities [41],[58],[59]. The proposed decomposition does not offer any computational advantages, but is a tool that can be used to explain certain phenomena that are observed in rarefied gas flows.

Such flows are characterized by relatively large Knudsen numbers, meaning that the mean free path is comparable to a characteristic length of the problem. In those regimes a particle can travel a significant distance after being emitted from the wall before colliding with other particles. This particle will carry the boundary information, such as temperature, to a location far from the boundary, and this leads to very interesting non equilibrium phenomena, such as the thermal creep flow. As most of the non-equilibrium phenomena depend on this mechanism, it is of great scientific importance to develop a method that is able to give a quantitative measure of the contribution of the ballistic and collisional parts.

4.2 Decomposition using the DSMC method

This decomposition has been achieved modifying the traditional DSMC algorithm in [33] by S. Stefanov. This was achieved by adding an index I_j for each simulator particle $j = 1, 2, ..., Number\ of\ particles$. Particles whose index value is 0 are part of the ballistic distribution and those with value 1 are part of the collision distribution. When a particle is emitted from the boundary its index value is set to 0, and when a pair of particles collides both their index values are set to 1, while no change is made during the free motion of particles. The distribution function is decomposed as

$$g\left(x, y, \vec{\zeta}\right) = g^{(b)}\left(x, y, \vec{\zeta}\right) + g^{(c)}\left(x, y, \vec{\zeta}\right) \tag{4.1}$$

where $g^{(b)}$ and $g^{(c)}$ denote the ballistic and collision parts of the distribution function respectively. During the simulation the particles' indexes change their values all the time. During the sampling procedure, where the macroscopic quantities are calculated, the two kinds of particles are sampled separately, to deduce the ballistic and collisional parts of the macroscopic quantities.

Based on the above description it is deduced that for the ballistic part of the distribution the boundaries act as a source, while the bulk flow acts as a sink. The situation is reversed for the collision part of the particle distribution, where the bulk flow acts as a distributed source and the walls as a sink. The equivalent deterministic procedure is not trivial, an attempt is made in the next section while some results are presented in Section 5.4.3.

4.3 Kinetic decomposition

The equivalent procedure was achieved using the kinetic model equations and the results are generally in agreement with the ones obtained using the DSMC method. In order to distinguish between the two methods, the term streaming instead of ballistic is used here. In Figure 5 c is the magnitude of the molecular velocity, θ is the polar angle, s_0 is the distance from the point (x, y) to the boundary along the characteristic and g^+ is the outgoing distribution.

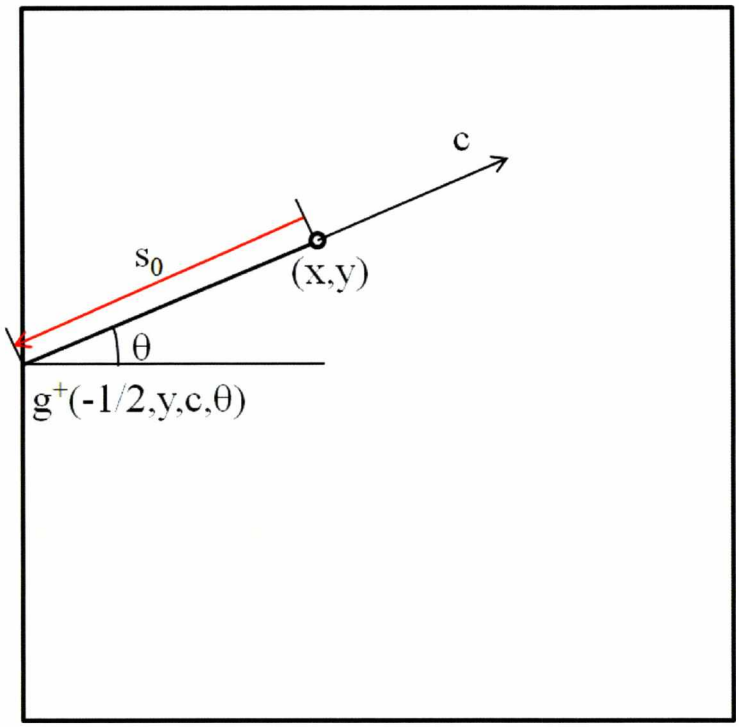

Figure 5: View of the cavity with the outgoing distribution and the distance s_0.

Taking the non-dimensional Shakhov model equation we have:

$$c\cos\theta\frac{\partial g}{\partial x}+c\sin\theta\frac{\partial g}{\partial y}+\frac{1}{Kn_0}\frac{\sqrt{\pi}}{2}n\tau^{1-\omega}g=\frac{1}{Kn_0}\frac{\sqrt{\pi}}{2}n\tau^{1-\omega}g^S\Rightarrow$$

$$c\left(\cos\theta\frac{\partial g}{\partial x}+\sin\theta\frac{\partial g}{\partial y}\right)+\frac{1}{Kn_0}\frac{\sqrt{\pi}}{2}n\tau^{1-\omega}g=\frac{1}{Kn_0}\frac{\sqrt{\pi}}{2}n\tau^{1-\omega}g^S\Rightarrow$$

$$-c\frac{\partial g}{\partial s}+\frac{1}{Kn_0}\frac{\sqrt{\pi}}{2}n\tau^{1-\omega}g=\frac{1}{Kn_0}\frac{\sqrt{\pi}}{2}n\tau^{1-\omega}g^S \tag{4.2}$$

Then, integrating the above expression from 0 to s_0 and assuming that the factor $\frac{1}{Kn_0}\frac{\sqrt{\pi}}{2}n\tau^{1-\omega}$ is constant, we get

$$\underbrace{g(x,y,c,\theta)}_{\text{Overall distribution}}=\underbrace{g^+\exp\left[-\frac{1}{Kn_0}\frac{\sqrt{\pi}}{2}n\tau^{1-\omega}\frac{s_0}{c}\right]}_{\text{Streaming part}}+\underbrace{\int_0^{s_0}\frac{1}{Kn_0}\frac{\sqrt{\pi}}{2}\frac{n\tau^{1-\omega}}{c}g^S\exp\left[-\frac{1}{Kn_0}\frac{\sqrt{\pi}}{2}n\tau^{1-\omega}\frac{s}{c}\right]ds}_{\text{Collision part}} \tag{4.3}$$

In the above expression the term in the left hand side is the overall distribution g, the first term in the right hand side is the streaming part $g^{(s)}$ and the second term of the right hand side

is the collision part $g^{(c)}$. The above procedure can be used for the reduced distribution functions, yielding:

$$\underbrace{\varphi(x,y,c,\theta)}_{\text{Overall distribution}} = \underbrace{\varphi^{+}\exp\left[-\frac{1}{Kn_0}\frac{\sqrt{\pi}}{2}n\tau^{1-\omega}\frac{s_0}{c}\right]}_{\text{Streaming part}} + \underbrace{\int_0^{s_0}\frac{1}{Kn_0}\frac{\sqrt{\pi}}{2}\frac{n\tau^{1-\omega}}{c}\varphi^{S}\exp\left[-\frac{1}{Kn_0}\frac{\sqrt{\pi}}{2}n\tau^{1-\omega}\frac{s}{c}\right]ds}_{\text{Collision part}} \quad (4.4)$$

and

$$\underbrace{\psi(x,y,c,\theta)}_{\text{Overall distribution}} = \underbrace{\psi^{+}\exp\left[-\frac{1}{Kn_0}\frac{\sqrt{\pi}}{2}n\tau^{1-\omega}\frac{s_0}{c}\right]}_{\text{Streaming part}} + \underbrace{\int_0^{s_0}\frac{1}{Kn_0}\frac{\sqrt{\pi}}{2}\frac{n\tau^{1-\omega}}{c}\psi^{S}\exp\left[-\frac{1}{Kn_0}\frac{\sqrt{\pi}}{2}n\tau^{1-\omega}\frac{s}{c}\right]ds}_{\text{Collision part}} \quad (4.5)$$

Using the discrete velocity method described in the previous chapter we solve the problem to obtain φ, ψ and the correspond expressions for the boundary conditions φ^{+} and ψ^{+}. The direct calculation of the collision part using the expressions

$$\varphi^{(c)} = \int_0^{s_0}\frac{1}{Kn_0}\frac{\sqrt{\pi}}{2}\frac{n\tau^{1-\omega}}{c}\varphi^{S}\exp\left[-\frac{1}{Kn_0}\frac{\sqrt{\pi}}{2}n\tau^{1-\omega}\frac{s}{c}\right]ds \quad (4.6)$$

and

$$\psi^{(c)} = \int_0^{s_0}\frac{1}{Kn_0}\frac{\sqrt{\pi}}{2}\frac{n\tau^{1-\omega}}{c}\psi^{S}\exp\left[-\frac{1}{Kn_0}\frac{\sqrt{\pi}}{2}n\tau^{1-\omega}\frac{s}{c}\right]ds \quad (4.7)$$

is complicated due to the path integral that needs to be calculated. This can be avoided calculating the streaming parts and then, knowing the overall distributions, the collision parts can be calculated through the expressions $\varphi = \varphi^{(s)} + \varphi^{(c)}$ and $\psi = \psi^{(s)} + \psi^{(c)}$.

The calculation of the ballistic part is performed in the following manner. The expressions $\varphi^{(s)} = \varphi^{+}\exp\left[-\frac{1}{Kn_0}\frac{\sqrt{\pi}}{2}n\tau^{1-\omega}\frac{s_0}{c}\right]$ and $\psi^{(s)} = \psi^{+}\exp\left[-\frac{1}{Kn_0}\frac{\sqrt{\pi}}{2}n\tau^{1-\omega}\frac{s_0}{c}\right]$ are used in each physical space element, where the quantities n and τ are mean values of those quantities at the four nodes of the element. This way the assumption made is overcome. The solution method will be described for one case, as depending on the polar angle we solve for a different node and the outgoing distribution is emitted from a different side of the element.

We calculate the distance $s_0 = \dfrac{\Delta x}{\cos\theta}$ of the characteristic as shown in Figure 6, and the point along the vertical side where the distribution is emitted is $y_1 = y_j - s_0 \sin\theta$. The outgoing distribution is estimated as a weighted average of the distribution in the adjusting nodes, as $\varphi^+ = w_1 \varphi^{(s)}_{i-1,j-1,m,n} + w_2 \varphi^{(s)}_{i-1,j,m,n}$ and $\psi^+ = w_1 \psi^{(s)}_{i-1,j-1,m,n} + w_2 \psi^{(s)}_{i-1,j,m,n}$, where $w_1 = \dfrac{y_j - y_1}{\Delta y}$ and $w_2 = \dfrac{y_1 - y_{j-1}}{\Delta y}$. Substituting those in the above expressions we get

$$\varphi^{(s)}_{i,j,m,n} = \varphi^+ \exp\left[-\frac{1}{Kn_0} \frac{\sqrt{\pi}}{2} n\tau^{1-\omega} \frac{s_0}{c_m} \right] \tag{4.8}$$

and

$$\psi^{(s)}_{i,j,m,n} = \psi^+ \exp\left[-\frac{1}{Kn_0} \frac{\sqrt{\pi}}{2} n\tau^{1-\omega} \frac{s_0}{c_m} \right] \tag{4.9}$$

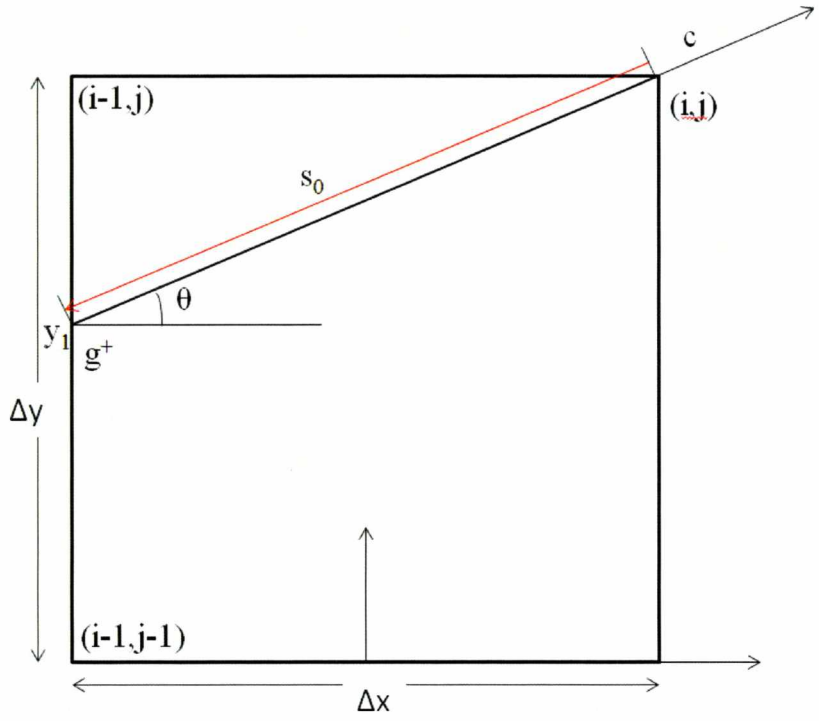

Figure 6: View of a grid element with the outgoing distribution and the distance s_0.

It is noted that the outgoing distributions denoted by the plus superscript are not necessarily the boundary conditions on the domain boundaries, but the distributions coming into the physical space elements.

The expressions for the macroscopic quantities become

$$n = \int \varphi d\vec{c} = \int \left(\varphi^{(s)} + \varphi^{(c)} \right) d\vec{c} = \int \varphi^{(s)} d\vec{c} + \int \varphi^{(c)} d\vec{c} = n^{(s)} + n^{(c)} \tag{4.10}$$

for the number density and

$$u_i = \frac{1}{n} \int c_i \varphi d\vec{c} = \frac{1}{n} \int c_i \left(\varphi^{(s)} + \varphi^{(c)} \right) d\vec{c} = \frac{1}{n} \int c_i \varphi^{(s)} d\vec{c} + \frac{1}{n} \int c_i \varphi^{(s)} d\vec{c} = u_i^{(s)} + n_i^{(c)} \tag{4.11}$$

for the velocity vector.

Having solved the overall problem, the overall macroscopic quantities are calculated, and calculating the streaming part of the distribution function, we integrate it to get the streaming part of the macroscopic quantities and through the above expressions, the collisional parts are calculated.

Chapter 5 Results and discussion

5.1 Computational parameters

The flow is characterized by the reference Knudsen number, in all of the cases checked, the temperature ratio in all but the known heat flux cases, where the value of the heat flux is known and the aspect ratio of the cavity H/W for the non-isothermal lateral walls case. The computational grid used was different in each case, and its parameters are summarized in the following table.

Table 3: The computational parameters for each case.

Case	I	J	Magnitudes	Angles	Error
Half heated cavity	200	200	40	200	10^{-10}
Bottom wall heated cavity with given temperature	400	400	80	400	10^{-13}
Bottom wall heated cavity with given heat flux	200	200	40	200	10^{-10}
Cavity with lateral walls having linear temperature variation	400	400*H/W	80	400	10^{-10}

It is noted that for the known bottom wall temperature and the linear temperature distribution along the vertical walls problems the temperature of the hot wall was used for the non-dimensionalization, while on the other two cases the temperature of the cold walls was

used. Therefore, the dimensionless quantities of these cases cannot be directly compared with each other and a transformation is required. Also, the reference Knudsen number used in section 5.2 for the half heated cavity is not the one defined at (3.5), but has been multiplied by the factor $\pi/4$ to match the definition of [25]. Finally, it is noted that upon convergence, all conservation principals are fulfilled.

5.2 Half heated cavity

In the half heated cavity problem, the boundaries at $x<0$ have a constant temperature T_C and the boundaries at $x>0$ have a constant temperature T_H, with $T_H > T_C$. Simulations were performed for one temperature ratio $\left(T_H / T_C = 2\right)$ and $Kn_0 = 0.05$, 0.5 and 5. The problem has been previously solved in [25] and the solution was repeated in this work for benchmarking purposes.

Since the boundary conditions are symmetric with the axis of symmetry at $y=0.5$, all results in this section are shown for the half of the flow domain. The effect of gas rarefaction in the flow field pattern can be seen in Figure 7. For small Knudsen numbers the biggest part of the bottom half of the flow domain is covered by a vortex (vortex Type-I) rotating so that the velocity in the vicinity of the bottom wall is from cold towards hot regions, due to thermal creep. Of course a second vortex of this kind exists in the upper part of the cavity, due to symmetry, and is counter rotating to the ones shown in Figure 7. In the bottom corners of the cavity two more vortices appear, counter rotating to the Type-I vortex (vortex Type-II), having a velocity in the vicinity of the bottom wall heading for hot towards cold regions. These vortices are created due to the viscous forces acted on them and in those regions are greater than the thermal creep forces. As the gas rarefaction is increased the Type-II vortices start to occupy a greater part of the cavity, squeezing the Type-I vortex towards the top part of the cavity.

In Figure 8 we can see the distribution of u_x along various horizontal planes of the cavity for various Knudsen numbers. Focusing to the distribution of u_x along the bottom wall $\left(y=0\right)$ we see that for $Kn_0 = 0.05$ the biggest part of the bottom wall has a positive u_x and only in small regions near the corners u_x becomes negative. As the Knudsen number increases

those regions become bigger, and in $Kn_0 = 5$ the biggest part of the bottom wall has a negative u_x, contrary to the velocity expected due to thermal creep.

The terms vortex Type-I and II are used here instead of the trivial terminology primary and secondary, as both kinds of vortices can be important in the description of the flow field, depending on the gas rarefaction. It is seen that as the Knudsen number increases the Type-II vortices start to occupy a considerable part of the flow domain. Moreover it can be seen at Figure 8 that the magnitude of u_x in the vicinity of the Type-II vortices can be greater than the magnitude in the vicinity of Type-I vortex. This flow, directed form hot to cold regions, is unexpected and of great interest as it is opposed to the normal thermal creep flow expected. It is also seen in Figure 8 and Figure 9 that as the gas rarefaction is increased, the magnitude of the velocities is decreased, and in the free molecular regime no motion is present as expected.

This problem was solved mainly for benchmarking purposes as mentioned above. It can be seen through Figures 8-13 that the comparison between the two results is very good. Of course there are small deviations but they are expected as in the present work the Shakhov kinetic model was used, while in [25] the BGK kinetic model was applied, and the BGK model cannot provide the correct viscosity and thermal conductivity simultaneously.

The boundary conditions in this configuration are discontinuous and a known issue of the DVM is the propagation of boundary induced discontinuities, known as ray effects. Those ray effects can be seen in Figure 8 and Figure 9 as small oscillations of the curves in the results of the present work. In the results of [25] they are not apparent as a sophisticated numerical procedure was used to cope with the discontinuities. Those discontinuities can also be seen at Figure 12 and Figure 13 at the distributions along the bottom wall. Because of the numerical procedure used in [25] they are much more visible compared to the results of the current work where they are smoothed. The discontinuity of the density distribution is much stronger in large Knudsen numbers, as expected, and is becoming weaker as the Knudsen number is decreased.

On the other hand the temperature discontinuity is strong even at small Knudsen numbers. Finally, we can see that the distributions of density and temperature at $y = 0.01$ are continuous even at high Knudsen numbers, as the discontinuities are rapidly diminished by viscous forces.

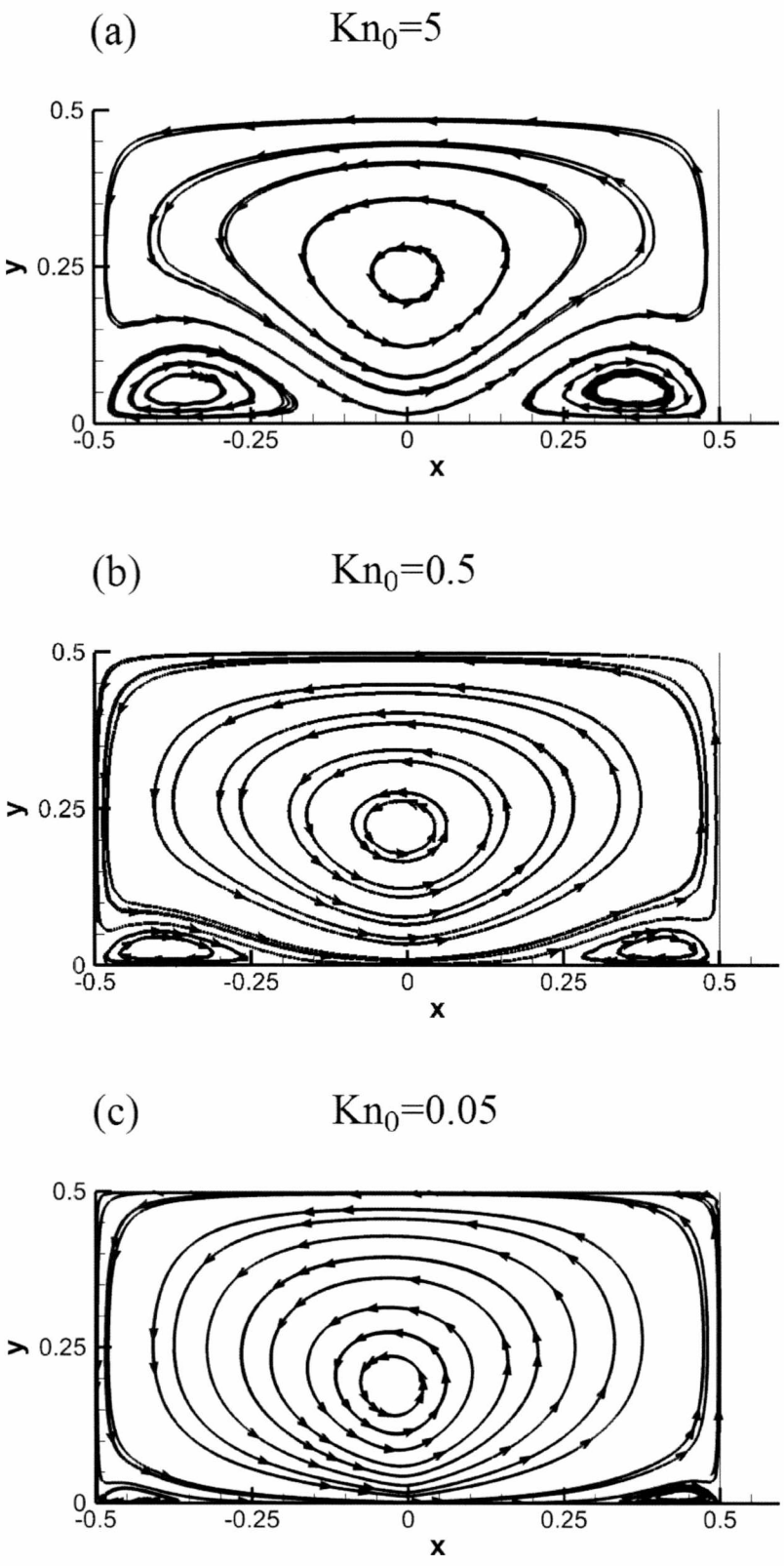

Figure 7: Streamlines for various Knudsen numbers

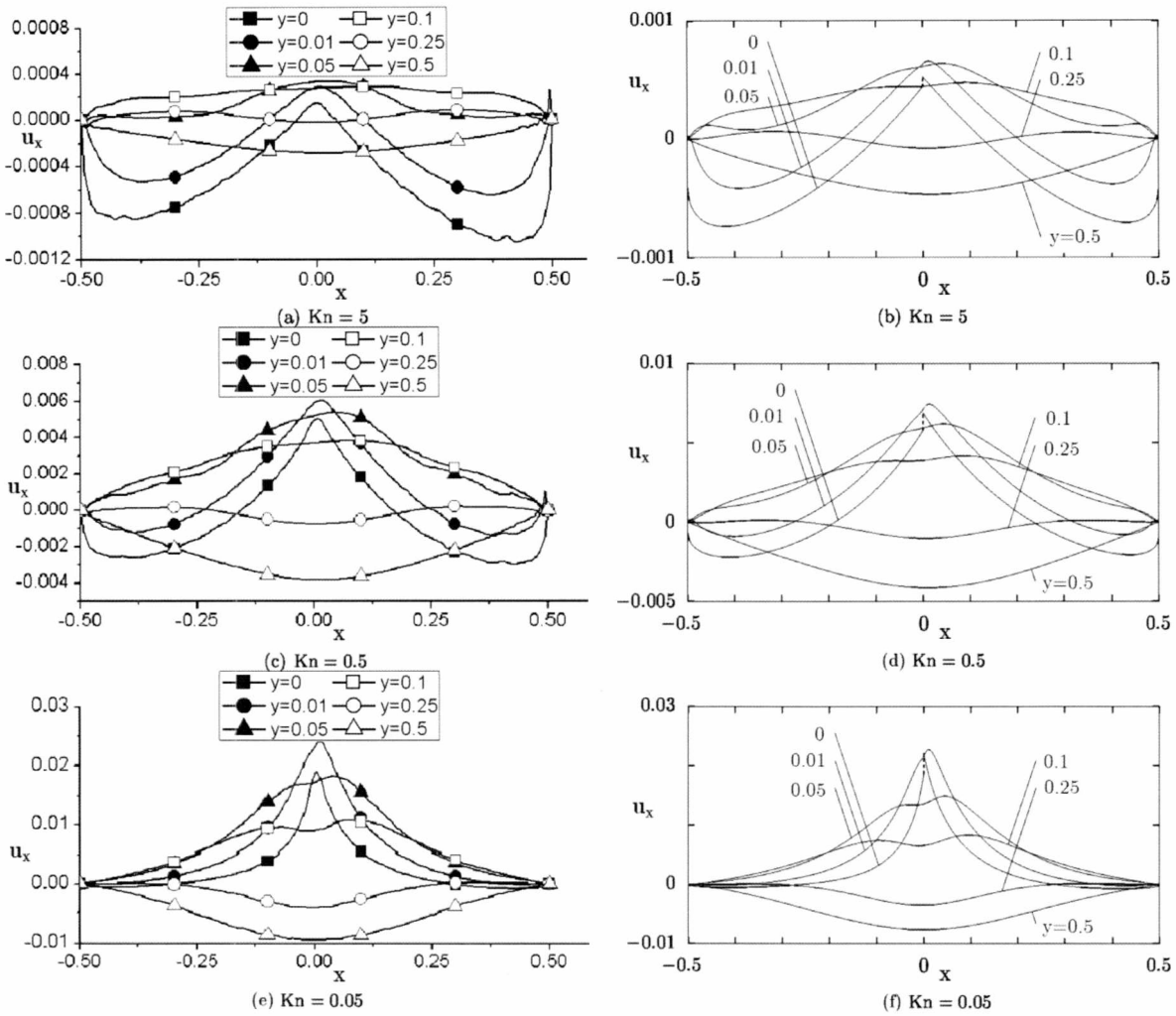

Figure 8: Distribution of the horizontal component of the velocity along horizontal planes for various Knudsen numbers: present results (left) and results of [25] (right).

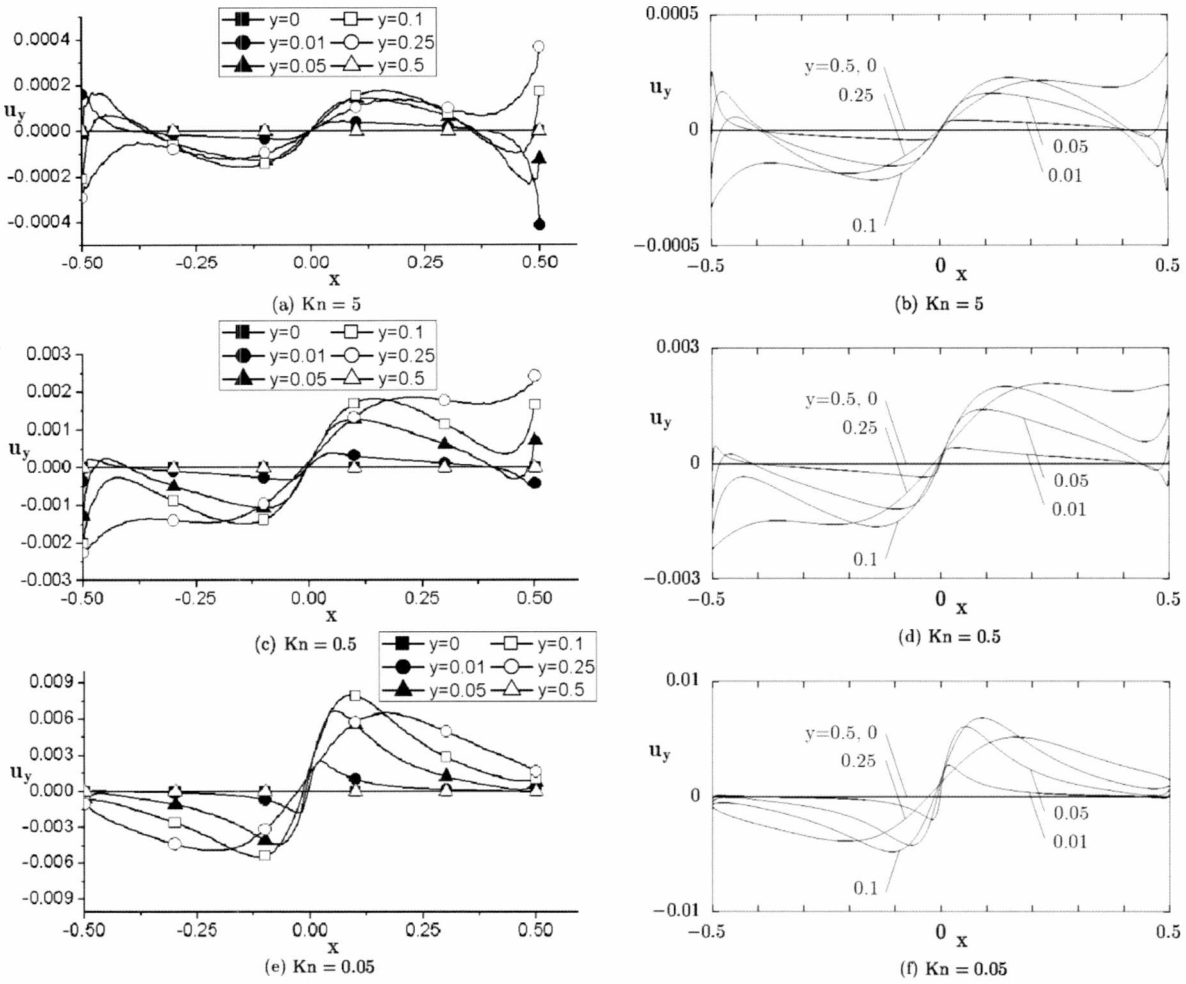

Figure 9: Distribution of the vertical component of the velocity along horizontal planes for various Knudsen numbers: present results (left) and results of [25] (right).

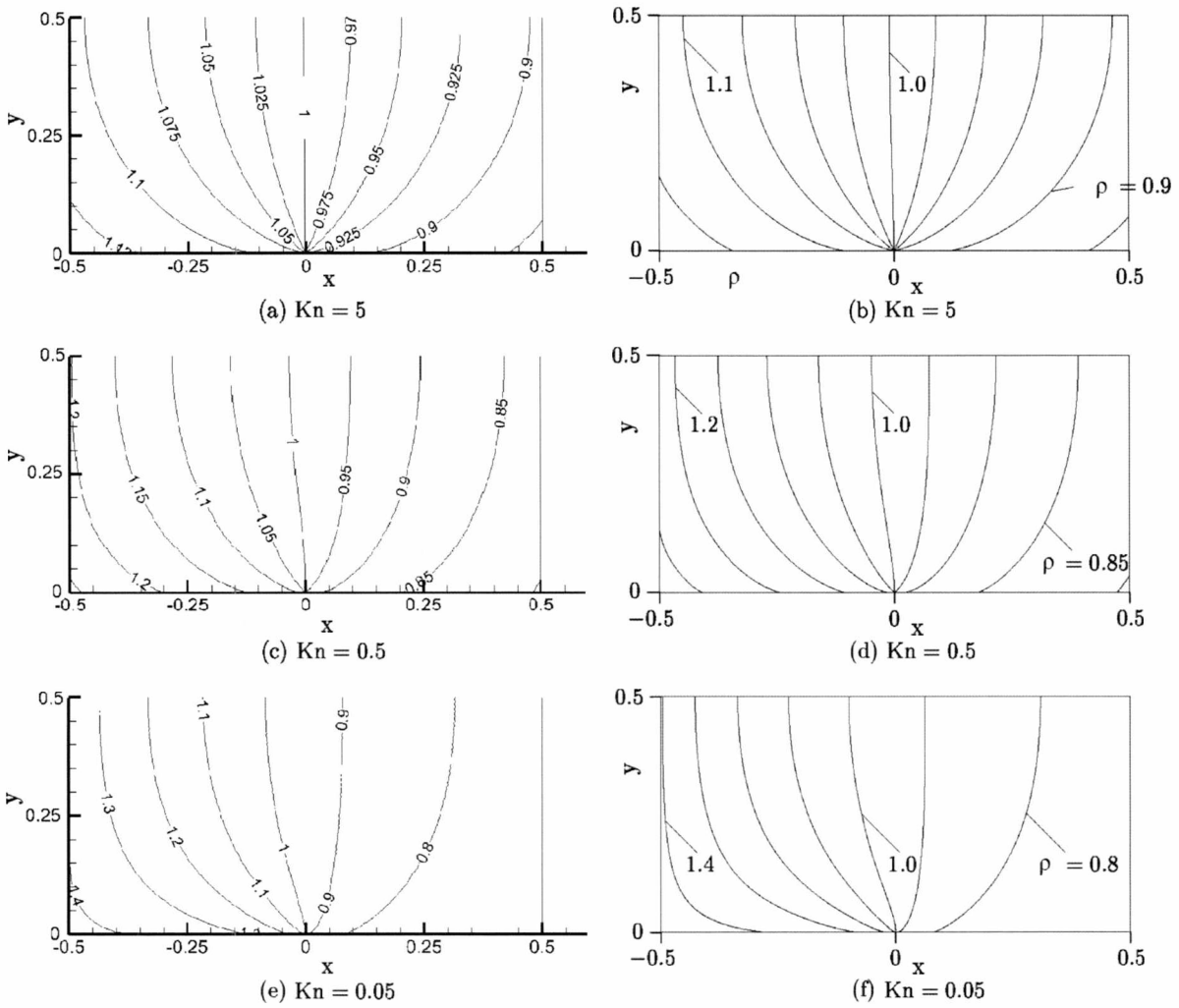

Figure 10: Density contours for various Knudsen numbers: present results (left) and results of [25] (right)

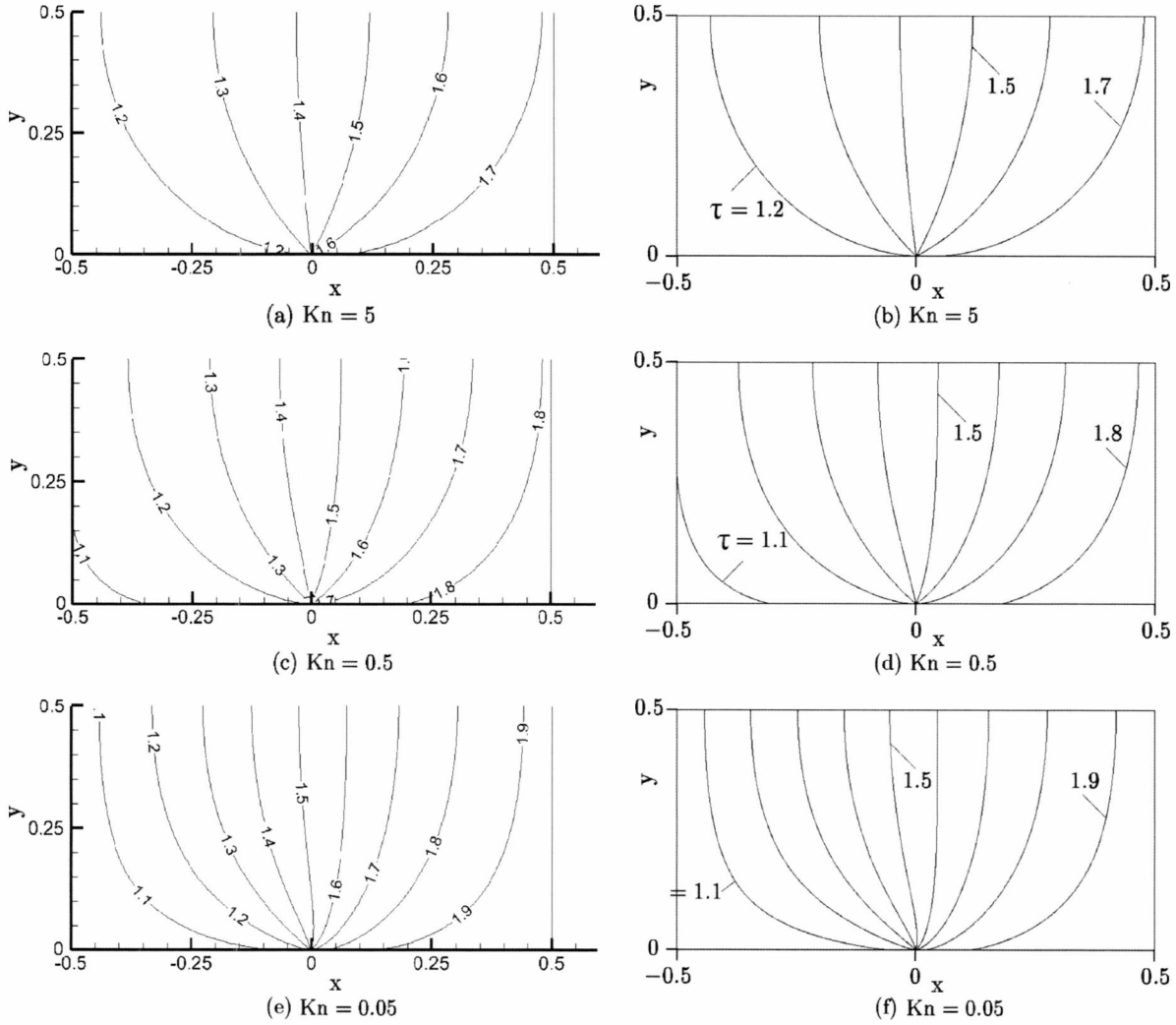

Figure 11: Temperature contours for various Knudsen numbers: present results (left) and results of [25] (right)

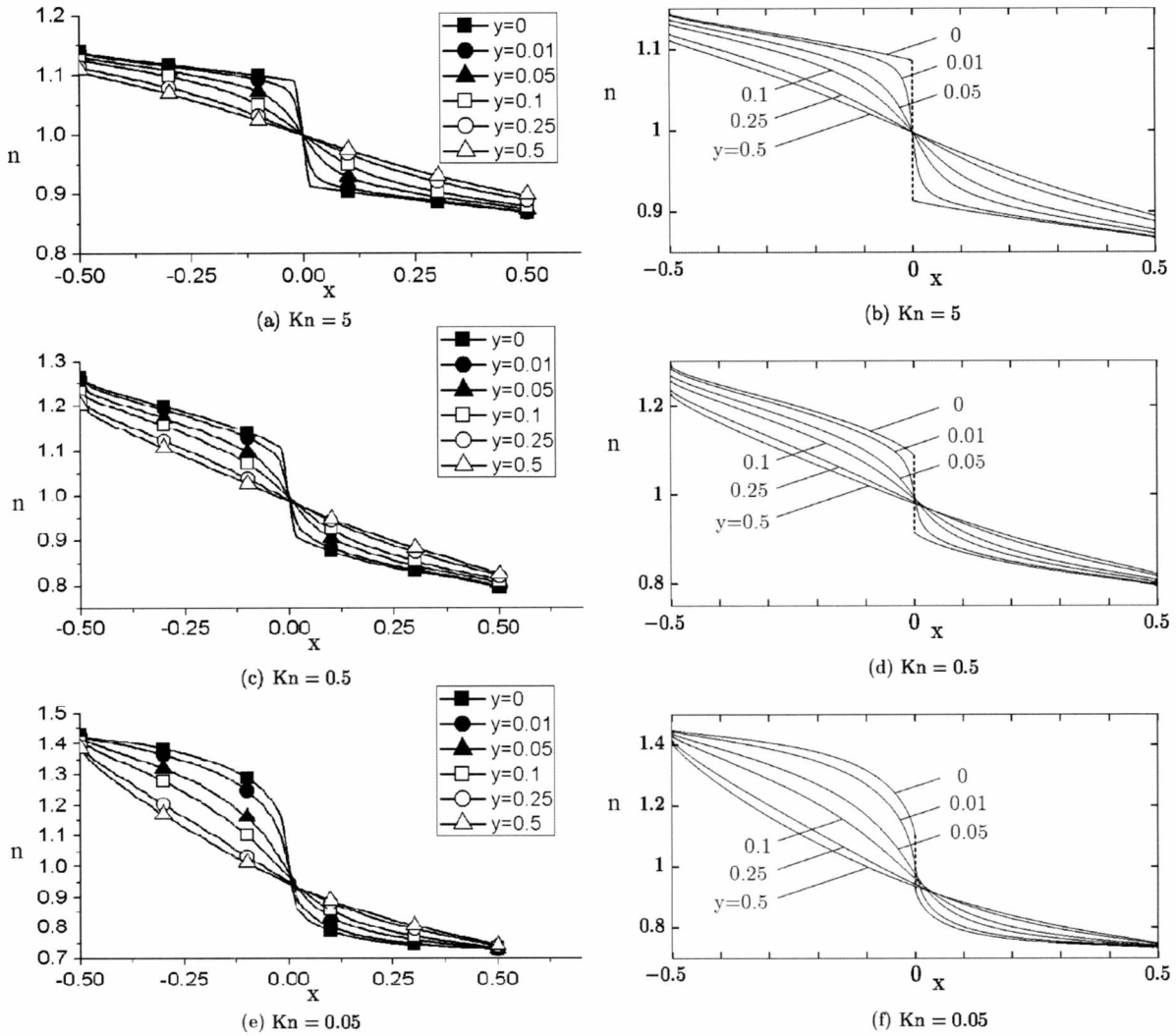

Figure 12: Distribution of density along horizontal planes for various Knudsen numbers: present results (left) and results of [25] (right).

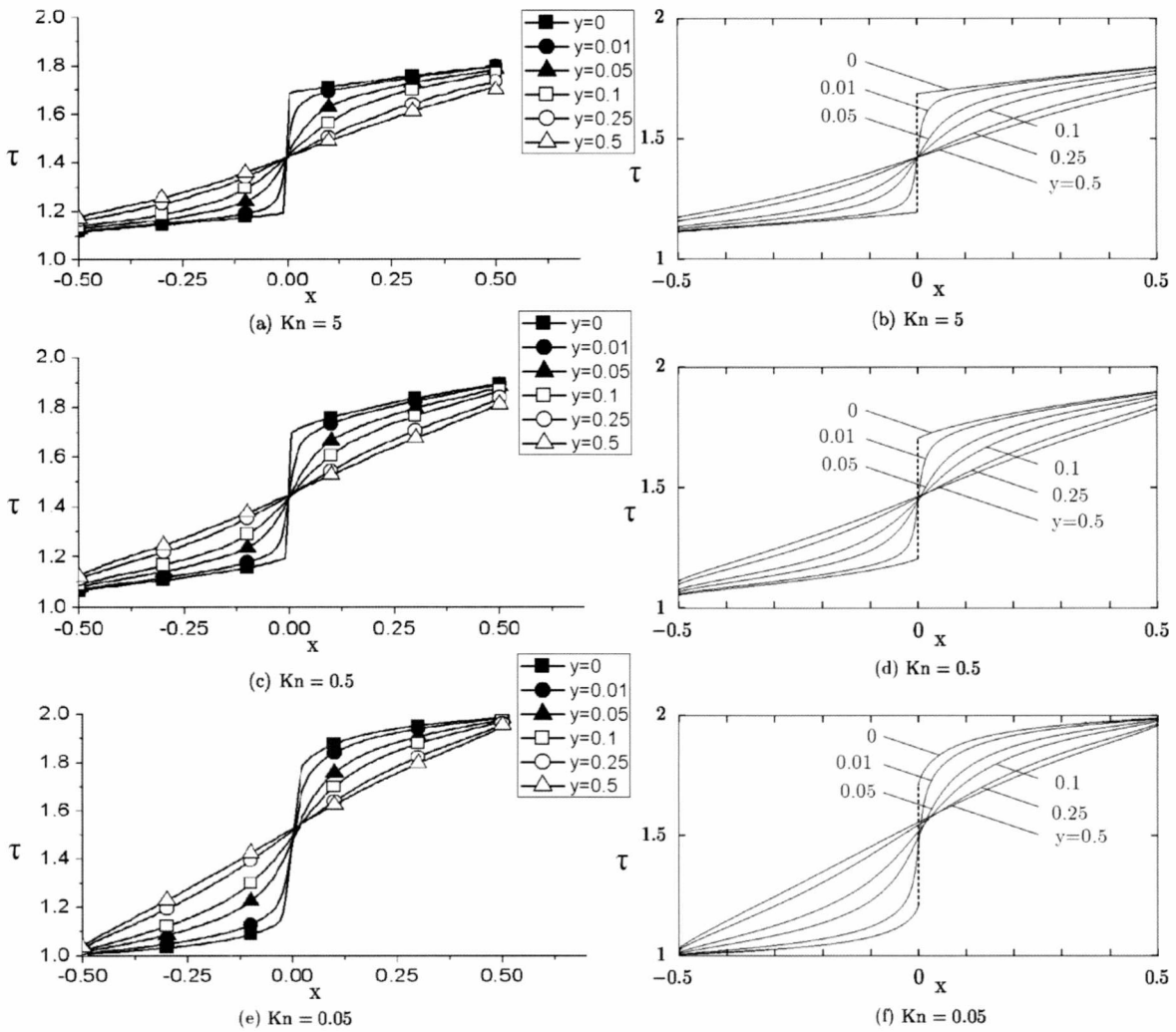

Figure 13: Distribution of temperature along horizontal planes for various Knudsen numbers: present results (left) and results of [25] (right).

5.3 Bottom wall heated cavity

In this formulation the bottom wall of the cavity is hot while the other three walls are kept at a constant lower temperature T_C. Two cases of this formulation where checked, in the first the bottom wall is kept at a constant given temperature T_H, while on the second the heat flux departing from the bottom wall is given and the wall temperature is part of the solution. In order to check the coherency of the results, the distribution of heat flux along the bottom wall that was taken from the solution of the given bottom wall temperature problem was used as a boundary condition for the given heat flux problem and the distribution of the wall temperature was the same as the one used as a boundary condition for the initial problem.

5.3.1 Dirichlet boundary conditions (given wall temperature)

This configuration, a cavity with one hot and three cold walls, is very commonly found in micro-electromechanical systems. During their design either the temperature ratio is assumed and the geometry and flow characteristics are chosen so that it is sufficient for the cooling, or the heat flux is assumed. In this section the given temperature case is investigated.

The flow was simulated for $0.1 < Kn_0$, three temperature ratios $T_C / T_H = 0.1,\ 1,\ 10$ and only hard sphere molecules $(\omega = 0.5)$ where assumed. In Figure 14 we see temperature contours and streamlines. At small Knudsen numbers the largest part of the cavity is occupied by vortices rotating so that the vertical velocity in the vicinity of the lateral walls is negative (Type-I), leading to a mass flow from cold towards hot regions. Two more vortices exist (Type-II), even in small Knudsen numbers, counter-rotating the Type-I vortices. The Type-II vortices are restricted to small regions near top of the lateral walls at small Knudsen numbers. As the Knudsen number is increased the Type-II vortices start to expand squeezing the Type-I vortices towards to the bottom part of the cavity. As can be seen in Figure 15 the greatest part of the lateral wall has a velocity from hot towards cold regions and in some cases the magnitude of u_y in the vicinity of the lateral walls is greater for the Type-II vortices, than for the Type-I. So it is clear that this unexpected flow from hot to cold regions exists in this formulation too.

Since these kinds of configurations are used mainly for the cooling of MEMS, it is of great practical interest to calculate the heat flux departing from the bottom plate. Figure 16 shows the dimensionless heat flux departing from the bottom plate in terms of the reference Knudsen number for various temperature ratios. The dimensionless heat flux increases, as the Knudsen number increases and tends to an asymptotic value as $Kn_0 \to \infty$. A very interesting finding is that the dimensionless heat flux does not necessarily increase as the temperature difference increases, but is seen to have a maximum around $T_C / T_H = 0.5$. The comparison shown in Figure 16 between the results of the current work (DVM) and the results of [60] (DSMC) have a good agreement, validating this interesting finding. Some dimensional results for the heat flux departing from the bottom plate per unit length in the z-direction are provided in Figure 17.

A well-known issue of the Discrete Velocity Method is the propagation of boundary induced discontinuities, especially at high Knudsen numbers, known as ray effects. A simple procedure was used to cope with the discontinuous boundary conditions at the two corners of the bottom wall. Along a small length at the two ends of the bottom wall, equal to 5% of the total side length of the square cavity, the temperature is taken to have a linear variation between T_C and T_H . Although the ray effects were diminished this way, the boundary conditions are still strongly discontinuous. Figure 18 shows the boundary conditions for $Kn_0 = 1$, $T_C / T_H = 0.1$ and for three values of the molecular velocity magnitude. It is seen that at the two corners of the bottom wall the boundary conditions are strongly discontinuous, despite the mentioned procedure. Another observation is that the value of the boundary conditions quickly tends to zero as the molecular velocity magnitude increases.

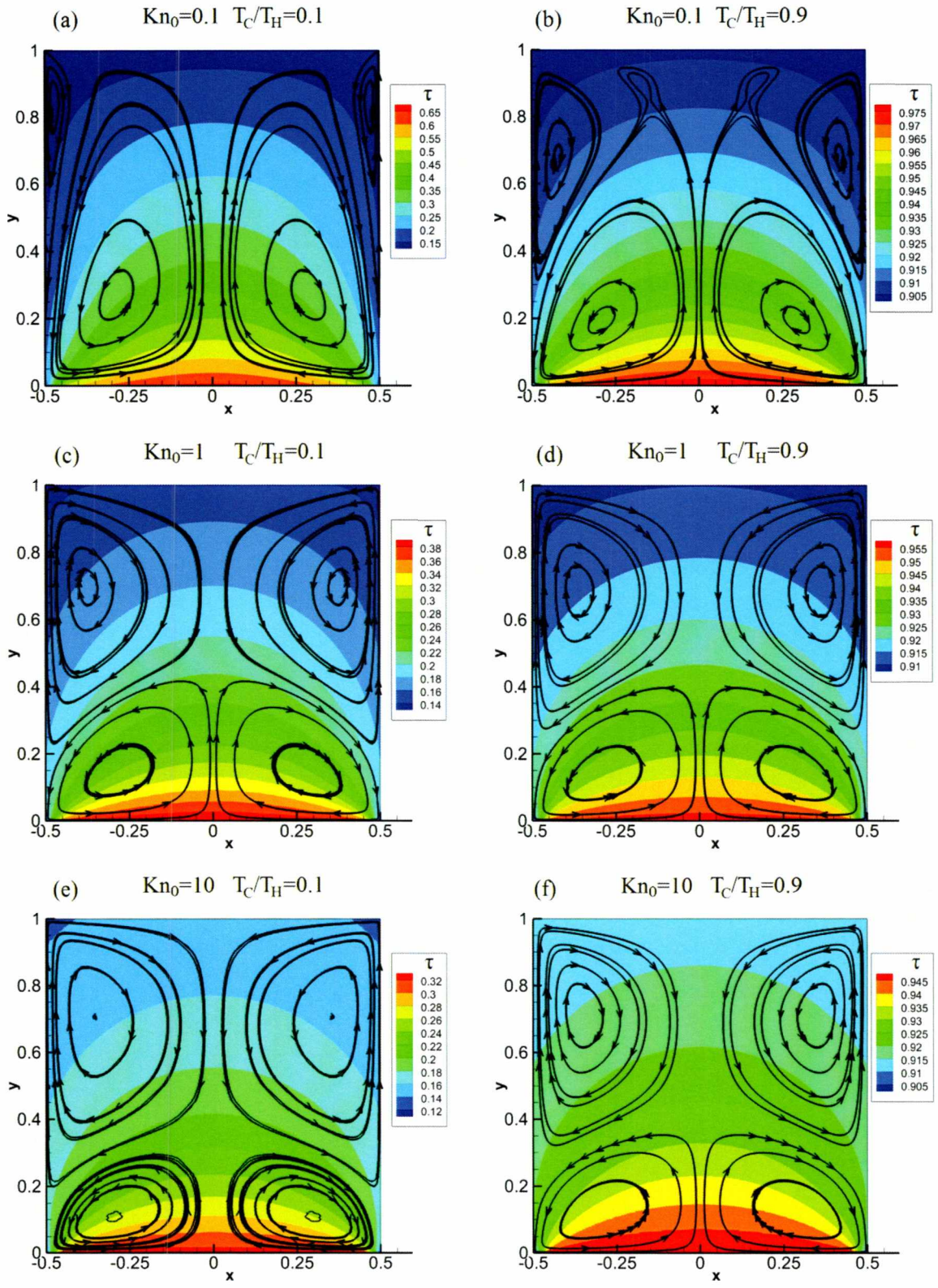

Figure 14: Streamlines and temperature contours for various Knudsen numbers with $T_C / T_H = 0.1$ (left) and $T_C / T_H = 0.9$ right

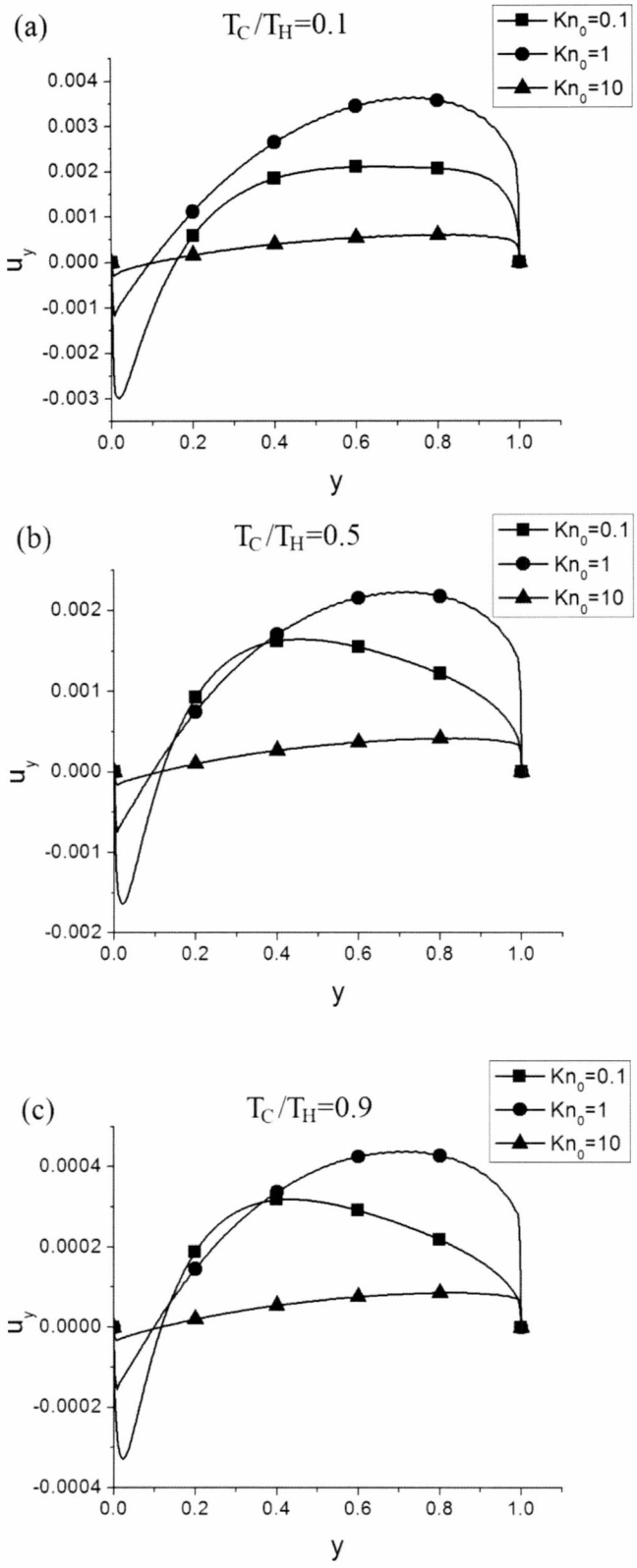

Figure 15: Distribution of the tangential velocity along the lateral walls for various temperature ratios and Knudsen numbers.

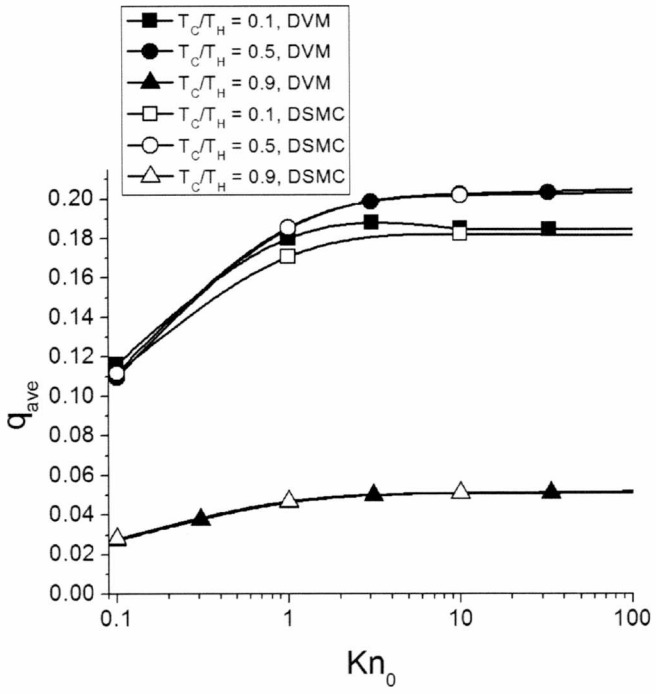

Figure 16: Average dimensionless heat flux departing from the bottom plate of a square enclosure in terms of the Knudsen number and for various temperature ratios.

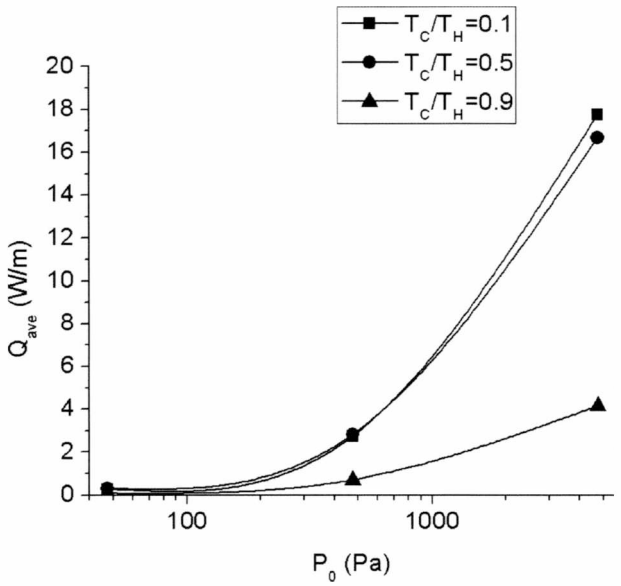

Figure 17: Dimensional heat flux in terms of the reference pressure for a square cavity of side $W = 50\mu\text{m}$ and for $T_0 = T_H = 1000\text{K}$.

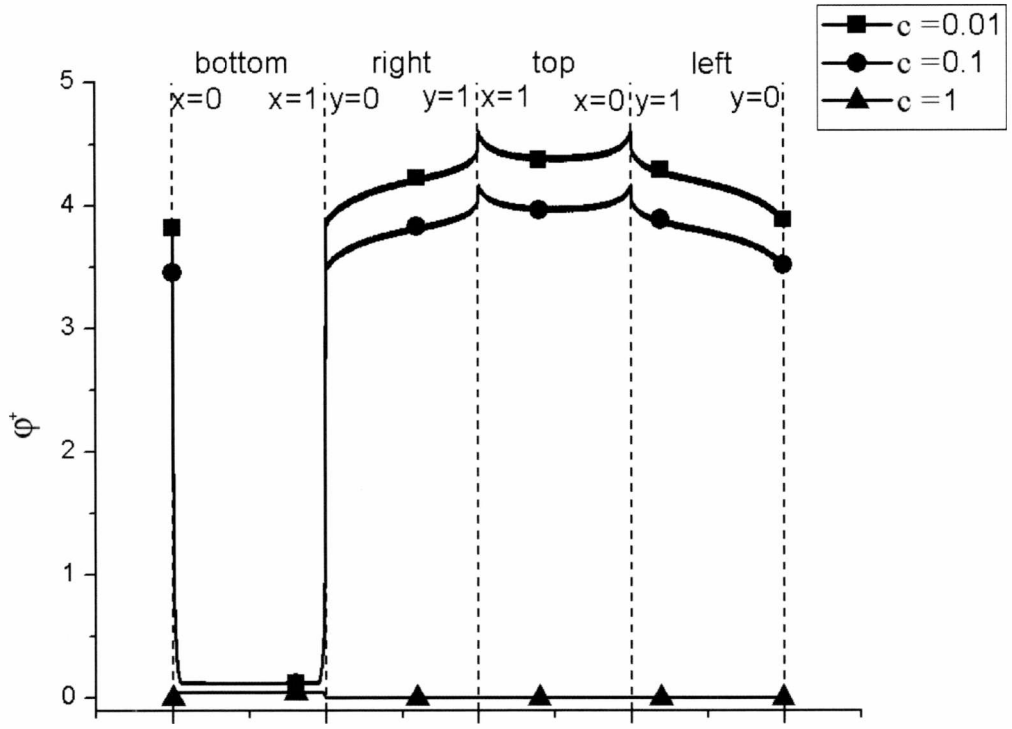

Figure 18: The boundary conditions for $Kn_0 = 1$, $T_C / T_H = 0.1$ and for three values of the molecular velocity magnitude.

5.3.2 Neumann boundary conditions (given heat flux)

In this configuration the heat flux departing from the bottom plate is given and the wall temperature is part of the solution. Figure 19 shows temperature contours and streamlines for $Kn_0 = 0.1$ and 1 with $q_w = 0.5$ and 1. The flow pattern is the same as in the given bottom wall temperature, as this is essentially the same set-up. Both Vortex-type I and II are present, in both reference Knudsen numbers shown in Figure 19. The type-II vortices are restricted close to the lateral walls for $Kn_0 = 0.1$, but still cover the biggest part of the wall, while for $Kn_0 = 1$ they are well developed covering the biggest part of the cavity.

Using the given heat flux boundary condition we can determine the operating temperatures for given geometry and flow conditions of the device, so that it is able to cope with the design load. The average dimensionless bottom wall temperature is given in Table 4 in terms of the dimensionless heat flux and the Knudsen number. This average dimensionless bottom wall temperature can in some cases be far from the actual values of the dimensionless bottom wall temperature distribution. This can be observed in Figure 20 where the distribution of the dimensionless bottom wall temperature is plotted for $q_w = 1$ and $Kn_0 = 0.01,\ 0.1,\ 1$ and 10. While for large reference Knudsen numbers the distribution is almost flat, for small values of the reference Knudsen number the distribution can have a large curvature, and the average value can be far from the actual.

Some dimensional results for the average bottom wall temperature are presented in Figure 21 in terms of the heat flux departing from the bottom plate for various values of the reference pressure for a square cavity of side $W = 50\mu m$ and $T_0 = T_C = 100K$.

Table 4: Average wall temperature for various reference Knudsen numbers and heat fluxes.

Kn_0	q_w					
	0.01	0.05	0.1	0.5	1	5
0.01	1.15	1.67	2.24	5.71	9.02	---
0.1	1.03	1.17	1.33	2.5	3.81	12.21
1	1.02	1.10	1.20	1.92	2.77	8.70
10	1.02	1.09	1.18	1.37	2.63	8.46

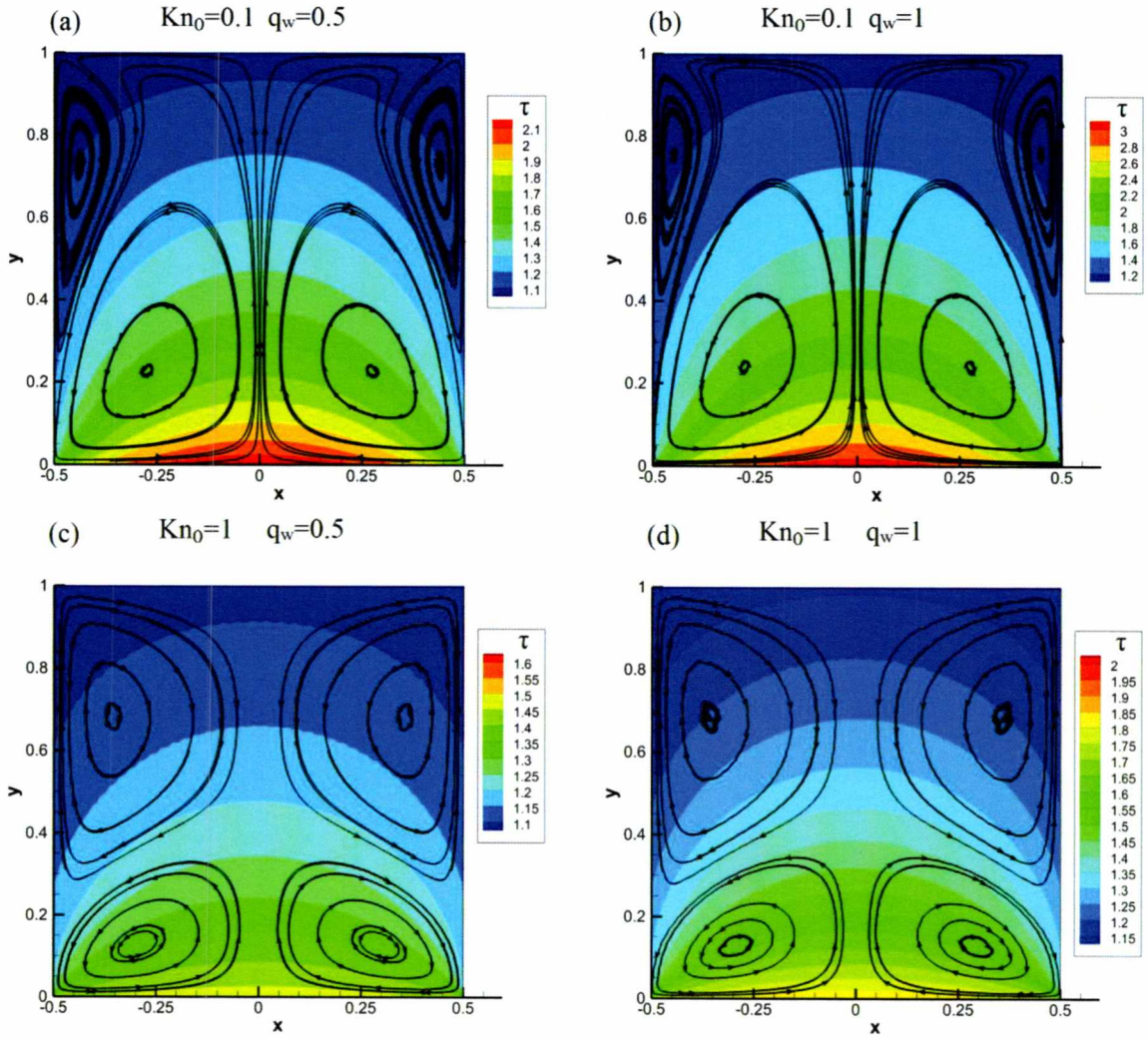

Figure 19: Streamlines and temperature contours for $q_w = 0.5$ (right), 1 (left) and $Kn_0 = 0.1$ (top), 1 (bottom).

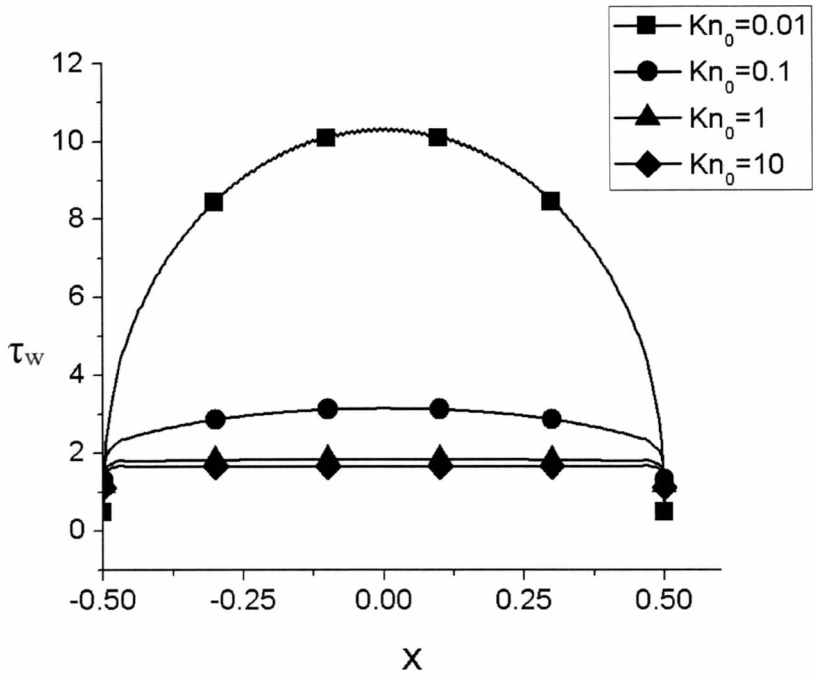

Figure 20: Distribution of bottom wall temperature for $q_w = 1$ and $Kn_0 = 0.01,\ 0.1,\ 1$ and 10

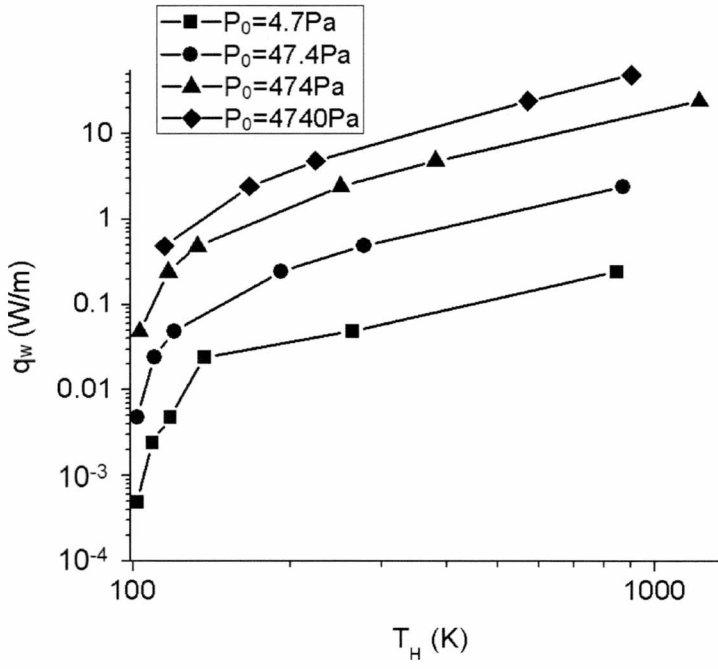

Figure 21: Dimensional heat flux departing from the bottom plate for a square cavity of side $W = 50\mu m$ and $T_0 = T_C = 100K$ in terms of the average bottom wall temperature for various values of the reference pressure.

5.4 Non-Isothermal lateral wall cavity

In this formulation the bottom wall is kept at a constant temperature T_H , the top wall is kept at a lower temperature T_C and the lateral walls have a linear temperature distribution between the cold and hot temperatures. Simulations were conducted for three temperature ratios $T_C / T_H = 0.1,\ 1,\ 10$, $0.01 < Kn < 10$ covering parts of the slip and free molecular regimes and the whole transition regime, three aspect ratios of the cavity $H / W = 0.5,\ 1,\ 2$ and two values of the IPL parameter $\omega = 0.5,\ 1$ corresponding to the two limiting cases of hard sphere and Maxwell molecules respectively.

5.4.1 Flow domain

The effect of gas rarefaction on the flow structure is shown in Figure 23. For $Kn_0 = 0.01$ only two vortices (Type-I) are present rotating so that the vertical velocity in the vicinity of the lateral walls is from cold towards hot regions, as expected due to thermal creep flow. As the Knudsen number is increased two additional vortices appear (Type-II) counter-rotating to the Type-I vortices. At $Kn_0 = 0.1$ the Type-II vortices are restricted to regions near the bottom corners of the cavity but as the Knudsen numbers is further increased they expand covering larger regions of the flow domain, and the Type-I vortices are squeezed towards the upper part of the cavity. Those Type-II vortices rotate so that the vertical component of the velocity in the vicinity of the lateral walls is from hot towards the cold regions, that is in the opposite direction of the expected thermal creep flow. Of course as the Knudsen numbers tends to infinity all motion in the cavity vanishes.

Figure 24 shows the streamlines and temperature contours for $T_C / T_H = 0.5, 0.9$ and the typical values of $Kn_0 = 0.1,\ 1,\ 10$. Comparing the flow pattern of this figure and Figure 23 the effect of the temperature ratio to the flow structure can be derived. As the temperature ratio and in effect the temperature gradient along the lateral walls are decreased the Type-II vortices become thinner, covering small parts of the flow domain, yet they can cover even the whole length of the lateral walls.

A quantitative description of the flow field is given in Figure 22, where the x and y components of the macroscopic velocity on vertical and horizontal planes, respectively, crossing the centers of the Type-I vortices are plotted. The results are for a square enclosure

with $T_C / T_H = 0.1$ and $Kn_0 = 0.01$, 0.1, 1. Along with the results of the present work (Shakhov), results of [33] have been included (DSMC) for comparison purposes. The distributions of u_y are symmetric about $x = 0$ and the points where u_y changes sign correspond to the x coordinate of the center of the two eddies of Type-I. The sign of u_x changes only once for $Kn_0 = 0.01$ and 0.1 meaning that only the two Vortex-type I are present (actually for Kn_0=0.1 the Type-II vortices have been created but are restricted to the bottom corners). For Kn_0=1 the sign changes several times meaning that the Type-II vortices are present. These observations are in accordance to the flow patterns shown in Figure 23. Another observation is that for all the cases the magnitude of the velocity is in the order of 10^{-2} or less (the local Mach is about 10% higher than the dimensionless velocity), which is typical of rarefied temperature driven flows. The maximum values of the Mach number were observed around Kn_0=0.1. Also as the Knudsen number is increased the magnitude of u_y in the vicinity of the Type-II vortices is increased and can become larger than the u_y in the vicinity of the Type-I vortices. These latter remarks are confirmed by the dimensionless flow rates of the Vortex-type I and II presented in Tables 5 and 6 respectively for various temperature ratios and reference Knudsen numbers. The former ones are computed integrating the dimensionless flux nu_x in the y direction from the center of the Vortex-type I to the top wall and the latter ones by integrating the flux nu_y in the x direction from the center of the Vortex-type II to the side wall. It is seen in Table 5 that that starting from Kn_0=0.01 as the Knudsen number is increased and for the same temperature ratio, the flow rate of Vortex-type I is increased obtaining a maximum value around Kn_0=0.07 and then is constantly decreased as the Knudsen number keeps increasing, for all temperature ratios. The corresponding flow rates of Vortex-type II in Table 6 indicate a maximum around Kn_0=1.2. The exact physical reasoning for these maximum flow rates with regards to the reference Knudsen number is contributed to the number of collisions between particles and between particles and boundaries as the gas rarefaction is changing. In addition, while for $Kn_0 \leq 0.1$ the flow rate of the Vortex-type II is several orders of magnitude smaller compared to the corresponding ones

Table 5: Dimensionless flow rate of Vortex-type I in a square enclosure for various Kn_0 and T_C / T_H

T_C / T_H	Kn_0						
	0.01	0.06	0.07	0.08	0.1	1	10
0.1	6.34(-4)	1.70(-3)	1.72(-3)	1.71(-3)	1.67(-3)	2.89(-4)	2.76(-5)
0.5	2.87(-4)	7.51(-4)	7.53(-4)	7.44(-4)	7.08(-4)	8.60(-5)	6.38(-6)
0.9	5.07(-5)	1.31(-4)	1.31(-4)	1.30(-4)	1.23(-4)	1.21(-5)	6.99(-7)

Table 6: Dimensionless flow rate of Vortex-type I in a square enclosure for various Kn_0 and T_C / T_H

T_C / T_H	Kn_0					
	0.1	1	1.1	1.2	1.3	10
0.1	2.55(-6)	1.18(-4)	1.198(-4)	1.204(-4)	1.202(-4)	3.99(-5)
0.5	6.98(-7)	2.46(-5)	2.504(-5)	2.513(-5)	2.512(-5)	8.70(-6)
0.9	8.41(-8)	2.85(-6)	2.902(-6)	2.936(-6)	2.942(-6)	1.08(-6)

of vortex Type-I, as the Knudsen number is increased the two flow rates become of the same order and in some cases the former ones are even larger. Also, for the same Knudsen number as the temperature difference is increased the flow rate is also increased.

The effect of the lateral walls in the flow pattern may be seen in Figure 25, where streamlines and temperature contours for two rectangular enclosures, namely, $H/W = 0.5$ and 2 for the specific case of $T_C / T_H = 0.1$ and $Kn_0 = 1$ are plotted. Comparing the flow fields of Figure 25 with the equivalent for a square cavity of Figure 23, it is seen that as the aspect ratio is increased the presence of the Vortex-type II becomes more dominant covering a larger part of the flow domain. Obviously, as the aspect ratio is increased the importance of the non-isothermal side walls compared to the bottom and top walls is also increased.

Since this is a thermally induced flow it is reasonable to investigate the effect of the intermolecular collision model and this is done by including in Figure 26 some results for Maxwell molecules for the specific cases of $T_C / T_H = 0.1$ and $Kn_0 = 0.1$ and 1. Comparing the plotted streamlines and temperature contours with the corresponding ones for hard spheres in Figure 23 it is observed that for $Kn_0 = 0.1$ there is actually no effect, while for $Kn_0 = 1$ there are differences.

5.4.2 Lateral walls

Here, a more thorough description of the macroscopic quantities in the vicinity of the boundaries of the enclosure is provided. This includes the y components of the velocity and heat flux as well as the shear stress along the lateral walls and the average heat flux from the bottom wall.

In Figure 27 the tangential velocity u_y along the lateral walls of a square enclosure for small, moderate and large temperature differences in a wide range of the reference Knudsen number are provided. When $u_y < 0$, the flow is from the top to bottom and corresponds to the expected thermal type flow as described by the Vortex-type I pattern, while when $u_y > 0$ the flow is the other way around and corresponds to the unexpected flow pattern as described by Vortex-type II. It is observed that when $Kn_0 = 0.01$ the values of u_y are negative and only very close to y=0 and 1 very small positive values appear. The Vortex-type I flow covers the whole flow domain. When $Kn_0 = 0.1$ both positive and negative values of u_y are observed. The positive values are close to the two ends and the negative values in the middle part of the wall. That implies that although the Vortex-type I flow still covers most of the whole flow field, counter rotating vortices at the bottom and top corners have been created, which, as the Knudsen number is increased, grow and merge into a Vortex-type II along the whole length of the side wall. These observations qualitatively hold for all three temperature ratios

According to the R13 approach in [31], the formation of the Vortex-type II is explained by the opposite contribution of the two different terms of the tangential velocity at the wall, which in the present notation, is written as

$$u_y^{R13} = -\frac{1}{\left(\tau n + 0.5 p_{yy}\right)}\left(\frac{\sqrt{\pi\tau}}{2} p_{xy} + \frac{1}{5} q_y\right) \tag{5.1}$$

The superscript R13 has been added here, in order to distinguish in our discussion the tangential velocity obtained by Eq. (5.1) from the one obtained through the kinetic solution. The first term in the parenthesis is the viscous part of the tangential wall velocity and the second one to the transpiration part, caused by the shear stress and the tangential heat flux, respectively. The respective magnitude of these terms determines the sign of the tangential velocity and the local direction of the flow along the side walls. In order to examine the validity of this theory, the kinetic results of p_{xy} and q_y are introduced to compute, according to Eq. (5.1), the viscous and transpirational parts of the wall tangential velocity and the whole velocity as well.

The shear stress p_{xy} and the tangential heat flux q_y along the lateral wall at $x=-1/2$ of a square enclosure for various Knudsen number and temperature ratios are provided in Fig. 28. It is seen that always $p_{xy}<0$ and $q_y>0$ so they have an opposite contribution to the tangential velocity. Since, however, as the Knudsen number is increased, both the values of the heat flux and the absolute values of the shear stresses are increased, it is necessary to further compute the contribution of each part separately.

In Figure 29, the tangential velocities obtained by kinetic theory and according to Eq. (5.1), denoted by u_y and u_y^{R13} respectively for $Kn_0=0.01$, 0.1, 1 and 2, are plotted. When the velocity distributions are negative the transpirational part of the solution dominates and the flow along the lateral walls is from cold-to-hot (Vortex-type I), while when they are positive the viscous part dominates and the flow is from hot-to-cold (Vortex-type II). The agreement between the kinetic and R13 theory in small Knudsen numbers is very good and then, as the flow becomes more rarefied, the discrepancies, as expected, are increased. In general, the good qualitative agreement for $Kn_0 \le 0.1$ indicates that the theory developed in [31] in order to explain the formation of the hot-to-cold flow in the vicinity of the walls is valid in the slip regime and fails as the Knudsen number is increased.

It has been pointed in the previous section that the aspect ratio of the enclosure effects significantly the flow configuration and quantities. To further demonstrate the effect of the lateral walls, the tangential velocity and heat flux along the lateral walls of enclosures with $H/W=0.5$, 1 and 2 for $T_C/T_H=0.1$ and $Kn_0=1$ are plotted in Figure 30. For the specific Knudsen number and temperature ratio the velocities are positive for all thre aspect ratios and approximately of the same magnitude resulting to stiffer velocity gradients as H/W is

decreased. The tangential heat flux is significantly increased as H/W is decreased, i.e., as the effect of the side walls is decreased.

In Figure 31 the average dimensionless heat flux departing from the bottom plate $q_{av} = \int_{-0.5}^{0.5} q_y(x,0)dx$ is plotted in terms of the reference Knudsen number Kn_0 for $T_C/T_H = 0.1,\ 0.5$ and 0.9. The corresponding results for the large temperature difference obtained by the DSMC method in [33] are included for comparison purposes. It is seen that the agreement between the corresponding Shakhov and the DSMC results is excellent. The dependency of q_{av} versus Kn_0 is qualitatively similar to the pure heat conduction problem between parallel plates, which corresponds to the limiting case of $H/W = 0$. However, quantitatively there are major differences and as H/W is increased the average heat flux is decreased, e.g. the computed values of q_{av} for $H/W = 0.5,\ 1$ and 2 are 0.35, 0.14 and 0.057 respectively. Concerning the effect of the collision parameter ω on q_{av} it turns out that it is small since the values of the computed average heat fluxes for hard sphere and Maxwell molecules are close. Finally, it is seen that in this case as the temperature difference between the top and bottom plates is increased the average heat flux for the same Kn_0 is also increased. Some dimensional results of the average heat flux departing from the bottom plate in terms of the reference pressure are seen in Figure 32.

In Figure 33 and Figure 34 the reduced distribution function is plotted in terms of the molecular velocity in various points of the cavity. Subfigures a,c,g and i correspond to the four cavity corners, subfigures b,d,f and h correspond to the middle of the stated wall and subfigure e corresponds to the center of the cavity. Figure 33 the distribution function for $T_C/T_H = 0.1$ and $Kn_0 = 0.05$ is shown. We observe that along the top wall the majority of particles are concentrated in a small region of the molecular velocity space near $c = 0$ and the number of particles outside of this region is very small, while in the other cases the distribution still has a maximum for $c = 0$ but is more evenly distributed. In some of the subfigures some weak discontinuities can be seen. The situation is much different in Figure 34 for $Kn_0 = 2$, where for all the cases the majority of particles is consecrated in small regions, and in the general case these regions are not symmetric with respect to the polar

angle of the molecular velocity. In all of the cases there are very strong discontinuities of the distribution function.

One of the main assumptions behind continuum models is that the flow is near equilibrium and the distribution function is either the local Maxwellian (Stokes analysis) or near the local Maxwellian (NSF analysis). When the reference Knudsen number is small this assumption is in the general case correct, whereas in large reference Knudsen numbers it fails. This can be seen in Figure 35, where the distribution function and the corresponding Maxwellian are plotted for $T_C / T_H = 0.1$ and $Kn_0 = 0.05$ and 2 at the center of the cavity. It is observed that for the small Knudsen number the distribution is indeed close to the local Maxwellian, whereas for the large Knudsen number the two distributions are very different.

Finally in Figure 36 a comparison is made between the distribution function at the middle of the top wall for $T_C / T_H = 0.1$ and $Kn_0 = 0.05$ and the corresponding Maxwellian distribution function. Although the reference Knudsen number is small, and the flow is expected to be near thermodynamic equilibrium we see that the distribution is far from the local Maxwellian. This is because the local Knuden number can be very different from the reference Knudsen number in non-linear flows, causing such issues. The existence of such regions, especially near and on the boundaries can further decrease the range of validity of the continuum approach.

5.4.3 Streaming and collision contributions

The decomposition procedure described in Chapter 4, is applied in a square enclosure for $Kn_0 = 0.05$ and 2, with $T_C / T_H = 0.1$. The two values of the reference Knudsen number have been chosen as representatives to demonstrate the contribution of the streaming and collision parts to the overall solution in the slip and transition regimes. In addition, the corresponding results are typical for analyzing the thermal effects on the flow configuration in small and large Knudsen numbers. There is a good qualitative agreement for large reference Knudsen numbers with the results using the DSMC decomposition introduced in [33], but as the reference Knudsen decreases deviations between the two results appear.

The streamlines and the contours of the vertical velocities of the streaming and collision parts of the solutions, denoted by $u_y^{(s)}$ and $u_y^{(c)}$ respectively, as well as the overall solutions are given for $Kn_0 = 0.05$ and 2 in Figure 37. More specifically, Figure 37a,b show the streaming

parts and Figure 37c,d the collision parts, while the overall solutions which are the summation of the two corresponding parts are shown in Figure 37e,f. It is seen that the streamlines of the streaming parts are directed from the boundaries toward the interior of the bulk flow while the streamlines of the collision parts are directed from the interior of the bulk flow toward the walls. These qualitative observations are well expected from the physical point of view since in the streaming part the walls act as source and the bulk flow as sink, while it is the other way around in the collision part. The streamlines along with the vertical velocities contours clearly indicate when the flow is in the positive or negative direction corresponding to hot-to-cold and cold-to-hot flow respectively. The summation of these flow fields deduce the overall solutions shown in Figure 37e,f.

The streamlines in Figure 37 may be further analyzed. Staring with $Kn_0 = 2$, where the flow patterns are simpler, the streamlines of the streaming and collision parts are directed to and originated from single points, with total velocity equals to zero. The slight displacement between the two focal points and the small differences in the velocity magnitudes of the collision and ballistic parts, lead to the creation of Vortex-type II. Continuing with $Kn_0 = 0.05$ it is seen that the streamlines patterns of the streaming and collision parts are quite different. The streaming part has some resemblance with the corresponding one for $Kn_0 = 2$, showing one single point towards which the streamlines are directed. The collision part however is different indicating two curves from which the streamlines are originated. This is a major difference with the DSMC decomposition, which shows two single points from which the streamlines are originated, and those two points are also the centers of two symmetric spiral swirls, that is also not the case here. The slope of the streamlines with respect to the vertical walls is another important element in the present analysis. It is seen that at $Kn_0 = 0.05$ the negative slope of the streamlines of the collision part is larger than the positive slope of the streamlines of the streaming part and this is a clear sign for a cold-to-hot gas motion along the vertical walls. At $Kn_0 = 2$ the two slopes are about the same with the streaming one appearing to be larger, which is an indication for a hot-to-cold gas motion.

A more detailed view of the flow along the later walls is presented in Figure 38, where the tangential velocities and number densities are presented. In Figure 38a the tangential velocities of the streaming and collision parts are plotted along the lateral walls for $Kn_0 = 0.05$ and 2, while the corresponding overall tangential velocities are given in Figure

38b. It is seen in Figure 38a that for $Kn_0 = 0.05$, the tangential velocities $u_y^{(s)}$ and $u_y^{(c)}$ are positive and negative respectively along most almost the whole length of the side walls and only very close to the top corners their signs are interchanged. In parallel, the overall tangential velocity in Fig. 37b is negative.

In the case of $Kn_0 = 2$, the tangential velocities $u_y^{(s)}$ and $u_y^{(c)}$ in Figure 38a, are positive and negative respectively up to about y=0.7 and then their signs are interchanged. The overall velocity in Figure 38b, is positive up to about y=0.7 and then its value becomes negative taking very small values close to zero. From the above it is deduced that the negative or positive values of u_y, corresponding to cold-to-hot or hot-to-cold flow along the walls depends on which part of the solution, either the streaming or the collision part prevails with respect to the other. At $Kn_0 = 0.05$ the contribution of the collision part is more significant and only the Vortex-type I flow is observed, while at $Kn_0 = 2$ the magnitude of the streaming part has been increased and becomes respectively more significant and therefore the Vortex-type II flow shows up.

These arguments are also supported by the streaming and collision number density profiles denoted by $n^{(s)}$ and $n^{(c)}$, in Figure 38c. It is seen that along the walls for $Kn_0 = 0.05$, $n^{(s)} < n^{(c)}$ and for $Kn_0 = 2$, $n^{(s)} > n^{(c)}$, which also indicates that in the overall solution the contribution of the collision part dominates at small Knudsen numbers, while at large Knudsen numbers the contribution of the streaming part becomes more significant. In Figure 38d the overall density profiles computed as the summations of the two parts are provided for $Kn_0 = 0.05$ and 2.

Based on both Figure 37 and Figure 38 and the previous discussion some more general comments on the streaming and collision contributions in the overall solution may be stated. In the free molecular limit, the flow is perfectly balanced by pressure and temperature distributions and both collision and streaming velocities are equal to zero. Increasing the gas density and respectively decreasing the Knudsen number, collisions between molecules destroy this balance and from thermodynamic viewpoint, the gas reaction is a weak motion in the enclosure with streamline patterns depending on the Knudsen number, the wall temperature distribution and the enclosure geometry. At very large Knudsen numbers, the streaming part is dominating. At moderate values there is interplay between the streaming and

collision parts and the behavior of the overall solution is very subtle particularly in the transition regime. Finally, at very small Knudsen numbers the collision part is dominating. In this latter case, the classic thermal creep theory works and predicts correctly the cold-to-hot direction of the streamlines along the vertical walls. As the Knudsen number increases the impact of the streaming part also increases and the convective vortices start to rotate in the hot-to-cold direction along the lateral walls.

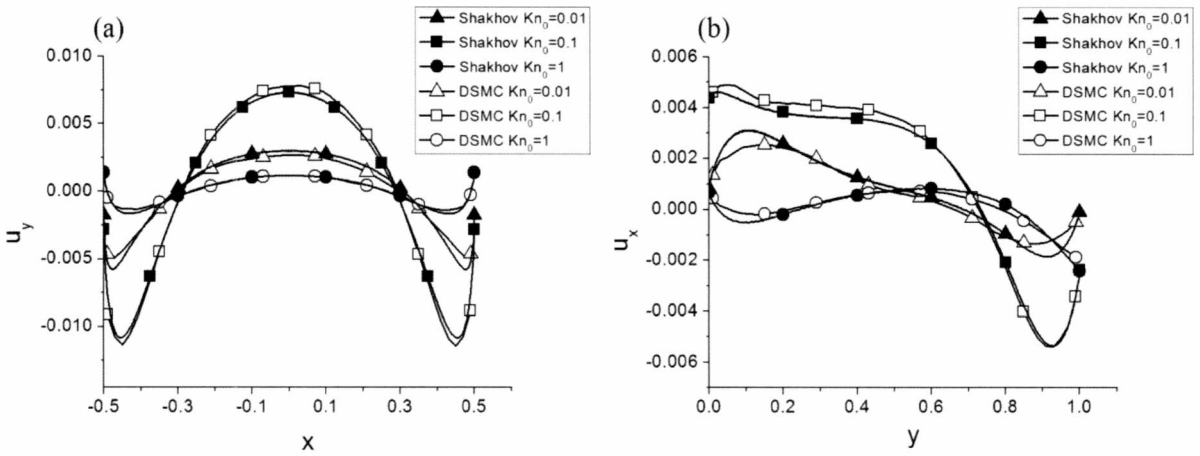

Figure 22: Distribution of the (a) y and (b) x components of the macroscopic velocity on vertical and horizontal planes respectively, passing through the centers of the Vortex-type I for a square enclosure with $T_C / T_H = 0.1$ and various Knudsen numbers.

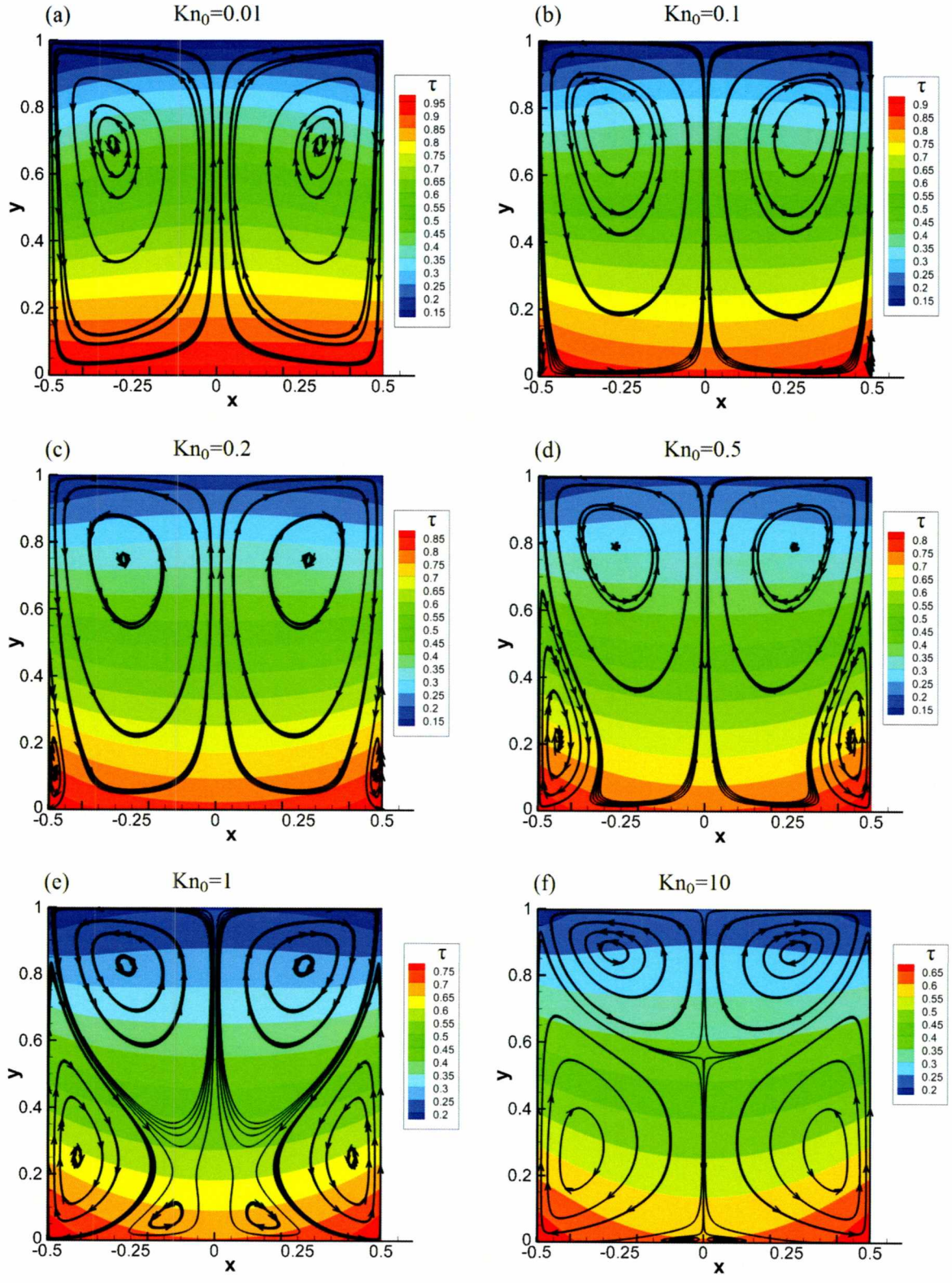

Figure 23: Streamlines and temperature contours for $T_C / T_H = 0.1$ and various Knudsen numbers.

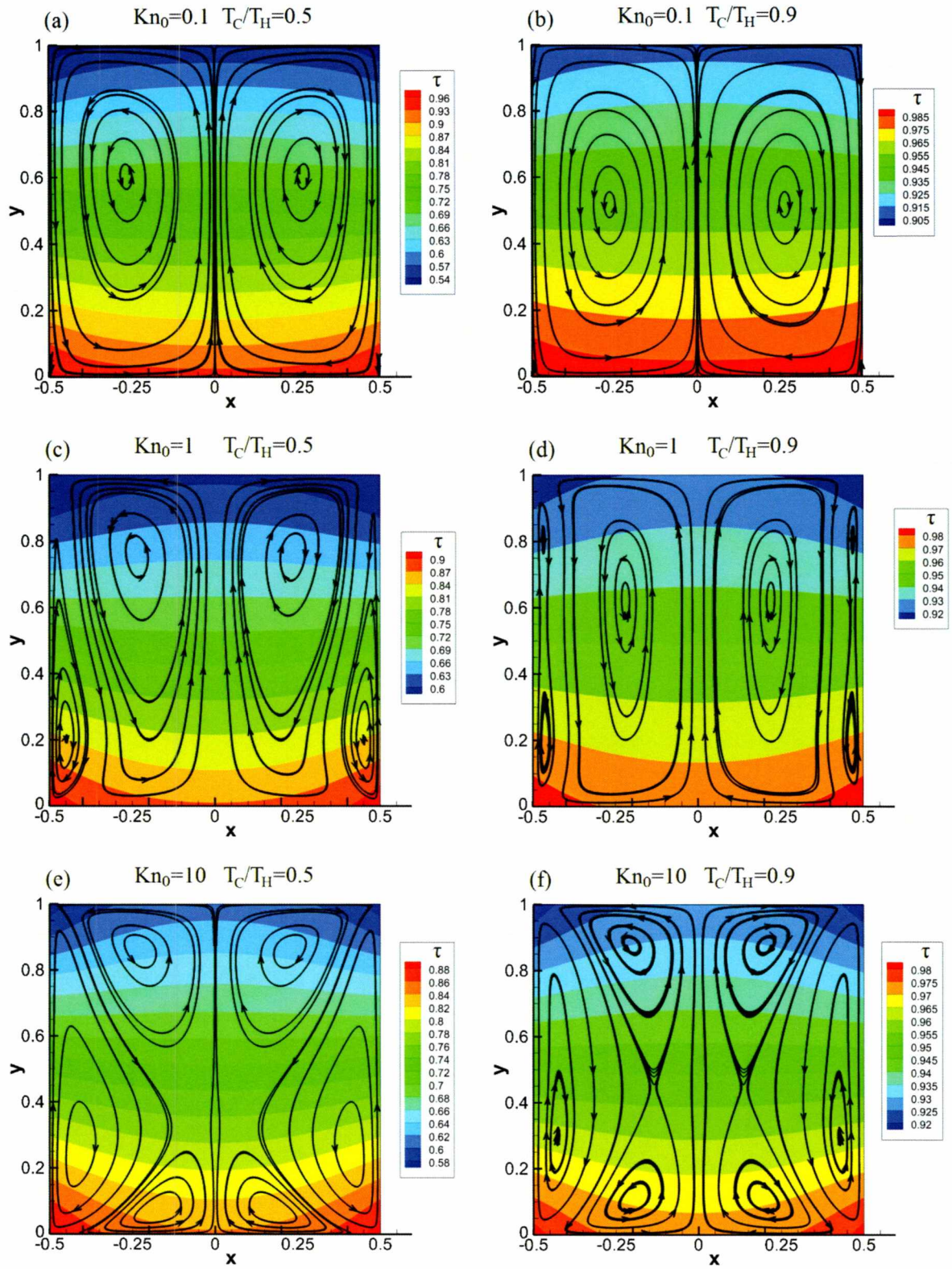

Figure 24: Streamlines and temperature contours for $T_C / T_H = 0.5,\ 0.9$ and various Knudsen numbers.

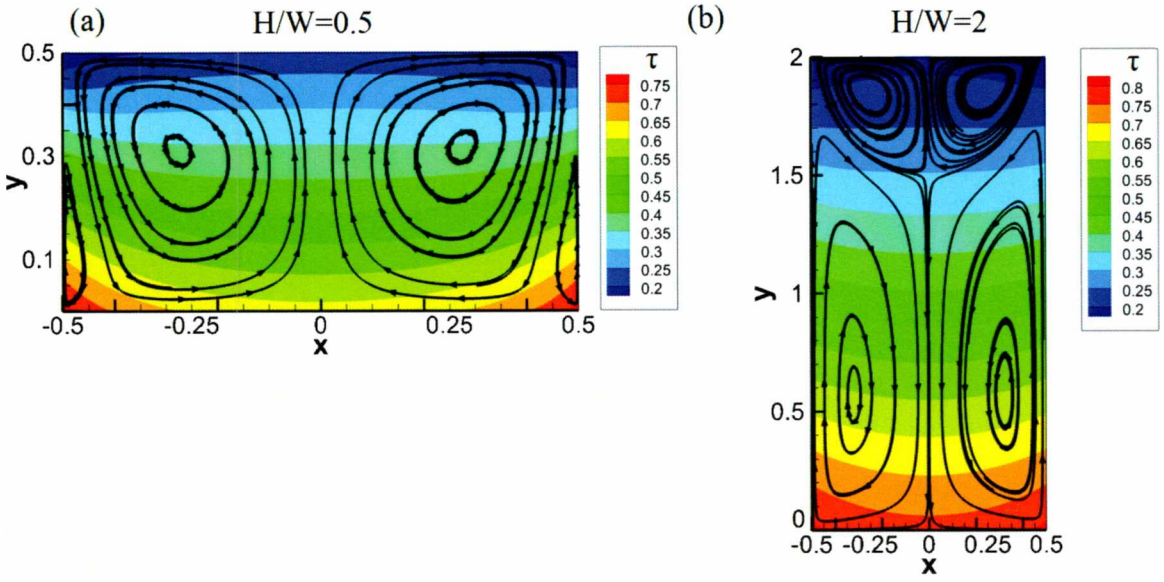

Figure 25: Streamlines and temperature contours in rectangular enclosures of (a) $H/W=0.5$ and (b) $H/W=2$, for $T_C/T_H=0.1$ and $Kn_0=1$

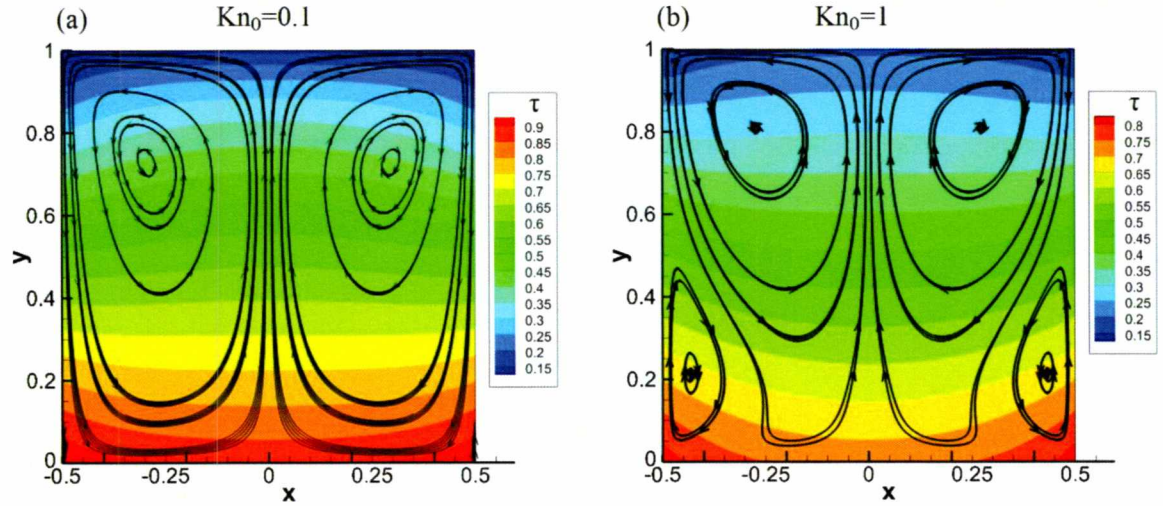

Figure 26: Streamlines and temperature contours in a square enclosure with (a) $Kn_0=0.1$ and (b) $Kn_0=1$ for Maxwell molecules $(\omega=1)$.

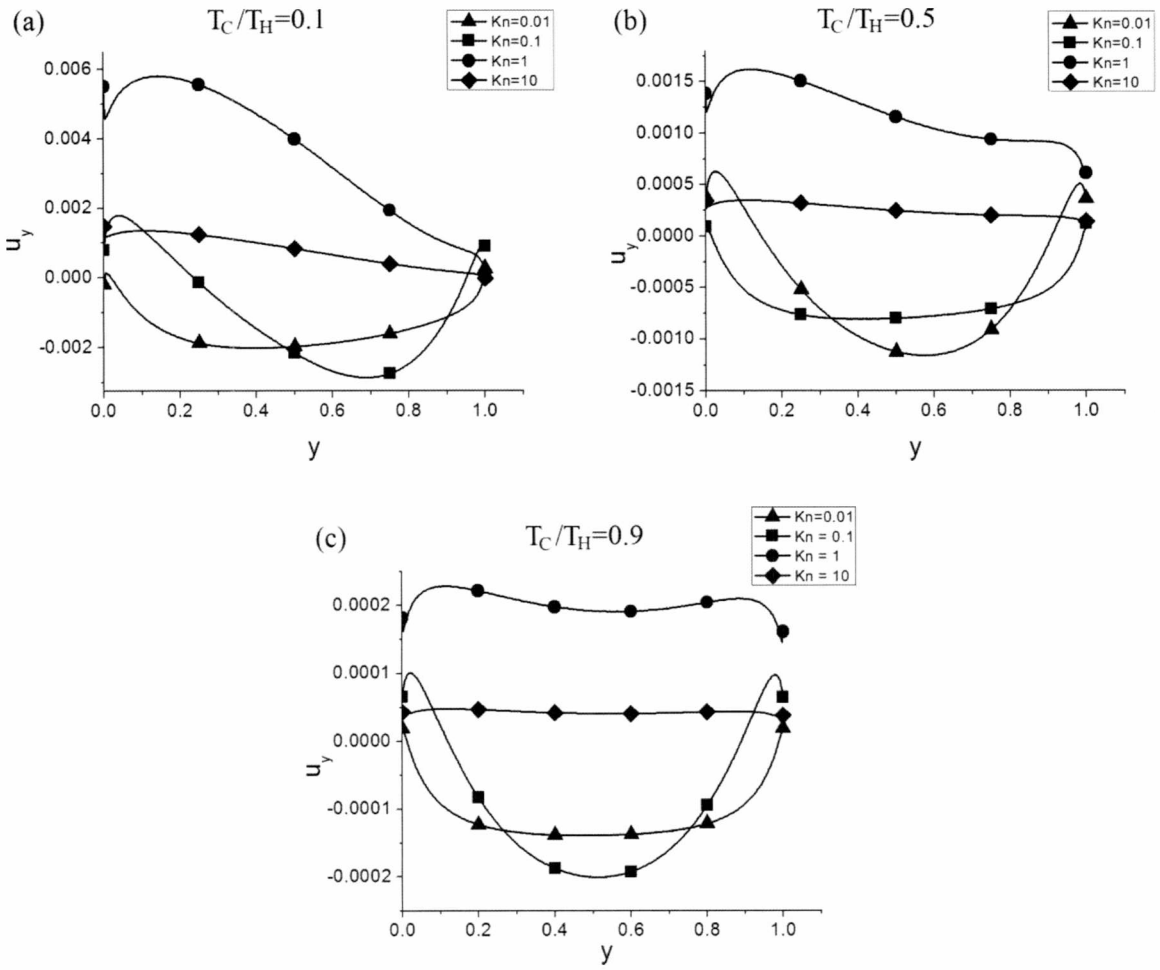

Figure 27: Distributions of the tangential velocity along the lateral walls of a square enclosure for various Knudsen numbers and temperature ratios.

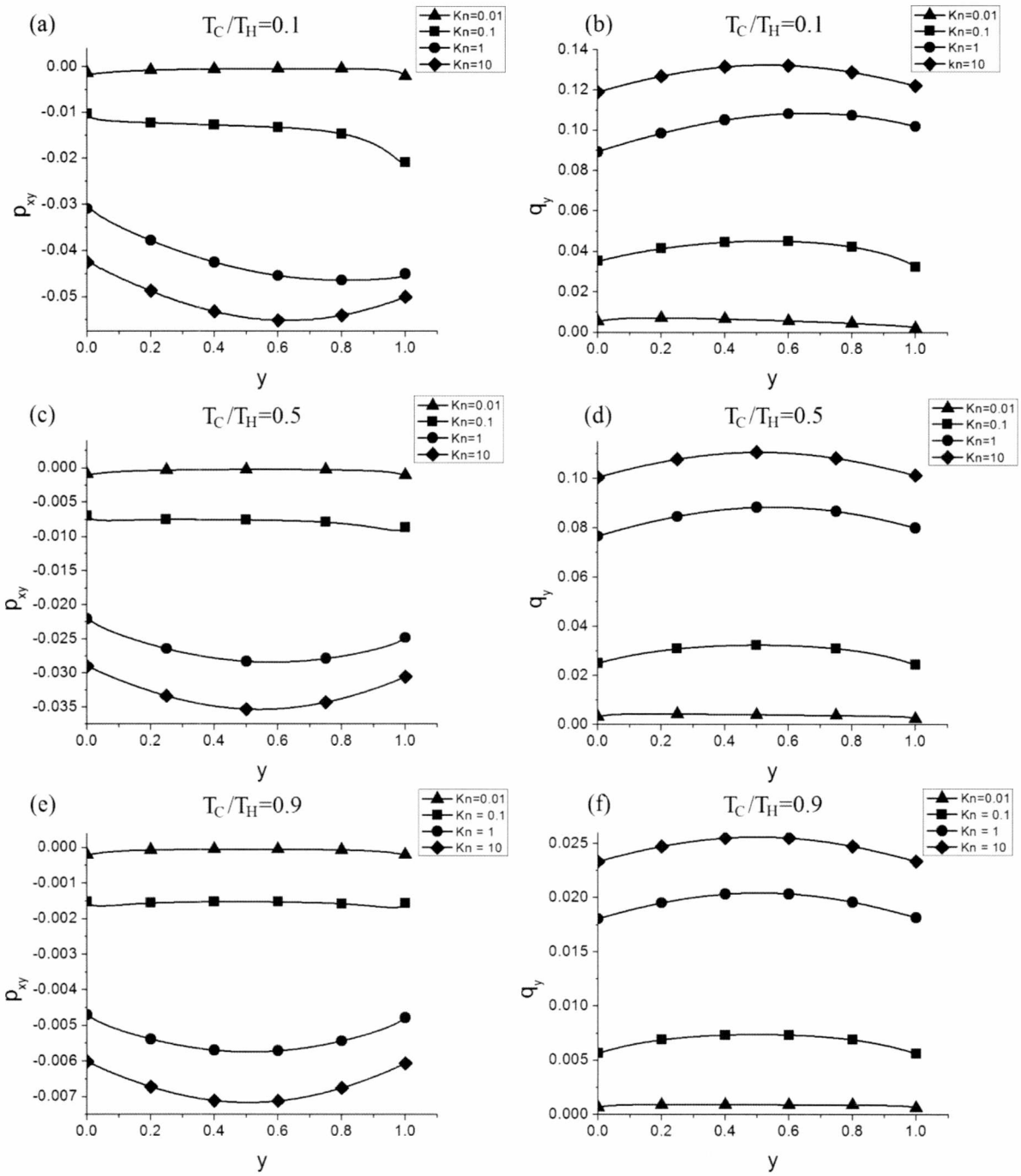

Figure 28: Distributions of the shear stress and tangential heat flux along the lateral wall at $x = -0.5$ of a square enclosure for various Knudsen numbers and temperature ratios.

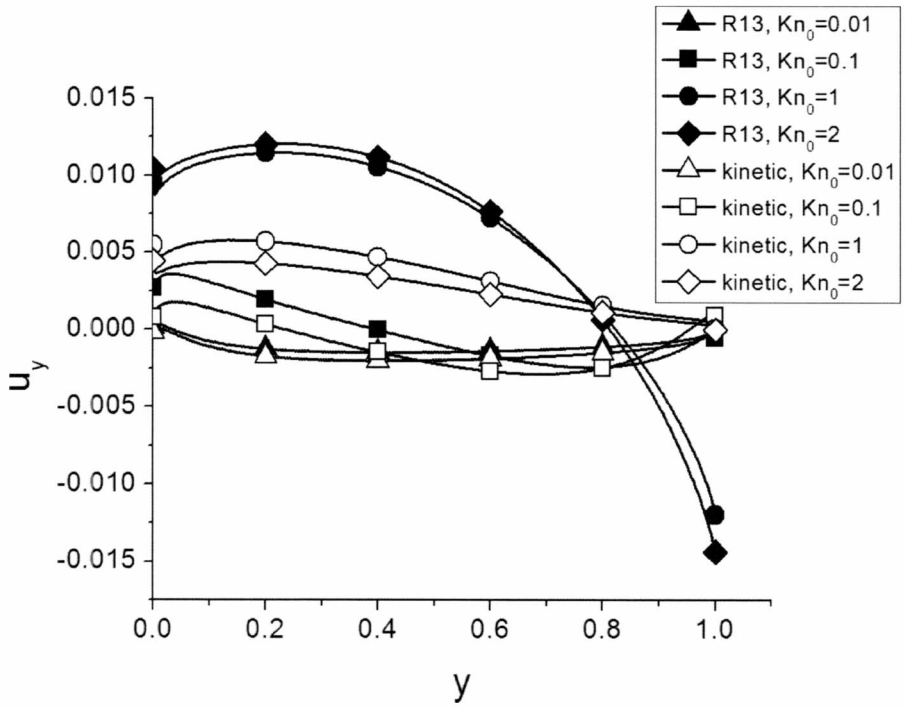

Figure 29: Tangential velocity distribution u_y along the lateral walls of a square enclosure for $T_C / T_H = 0.1$ and various Kn_0 computed directly by the present kinetic approach and by Eq. (5.1) based on the R13 approach

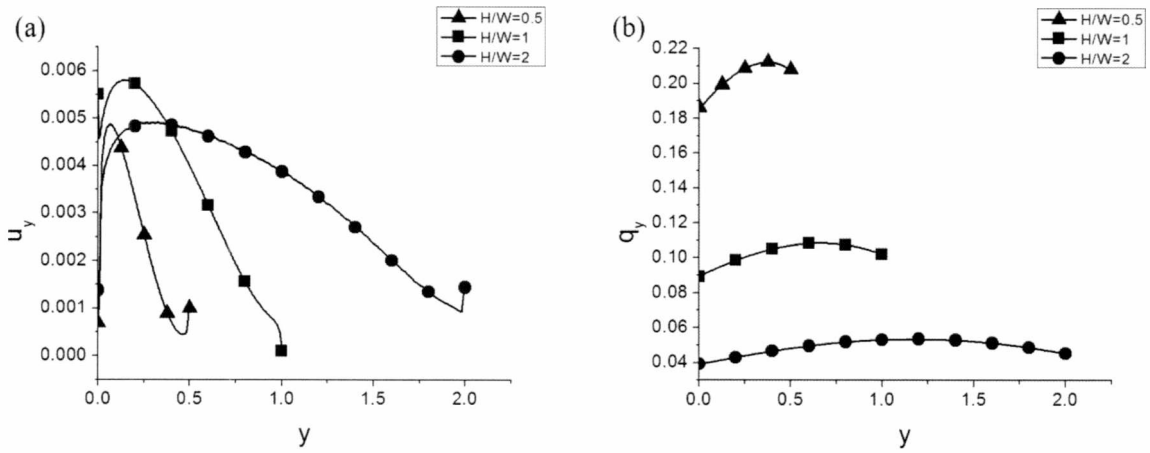

Figure 30: Distributions of the tangential (a) velocity and (b) heat flux along the lateral walls of rectangular enclosures with various aspect ratios for $T_C / T_H = 1$ and $Kn_0 = 1$.

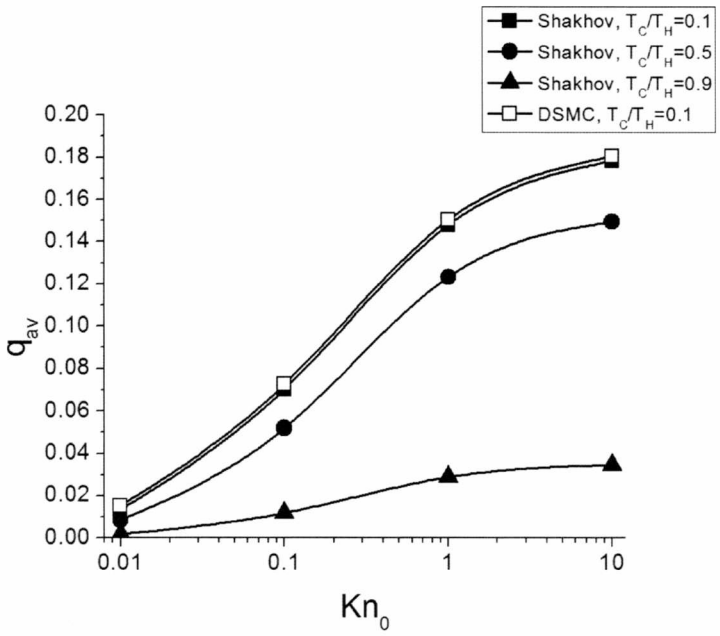

Figure 31: Average heat flux departing from the bottom plate of a square enclosure in terms of the reference Knudsen number for various temperature ratios.

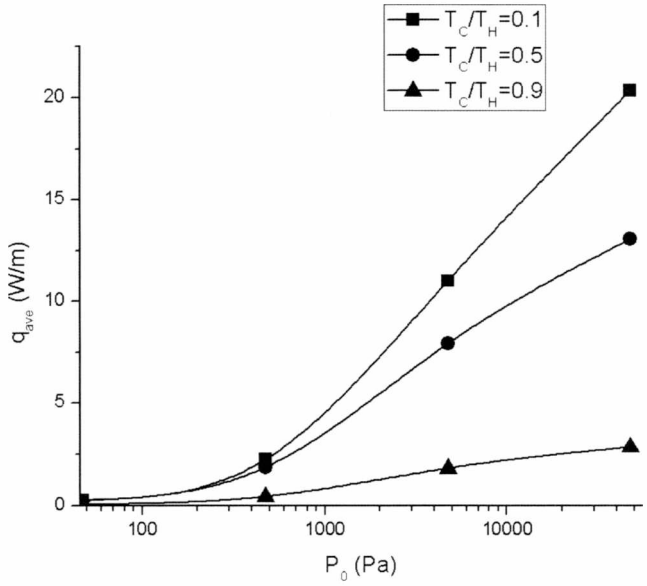

Figure 32: Dimensional heat flux in terms of the reference pressure for a square cavity of side $W = 50\mu\text{m}$ and for $T_0 = T_H = 1000\text{K}$.

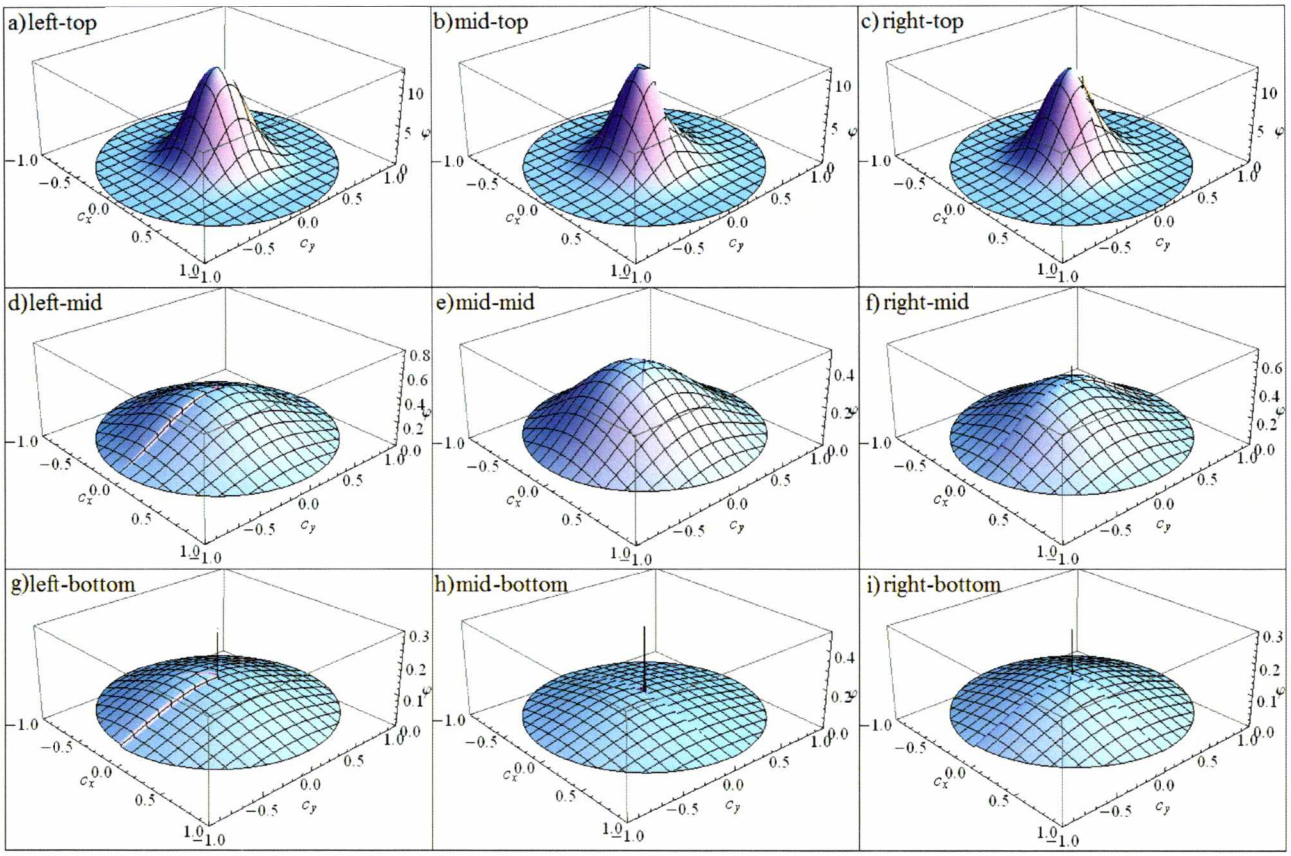

Figure 33: The distribution function at various points of the cavity for $T_C / T_H = 0.1$ and $Kn_0 = 0.05$.

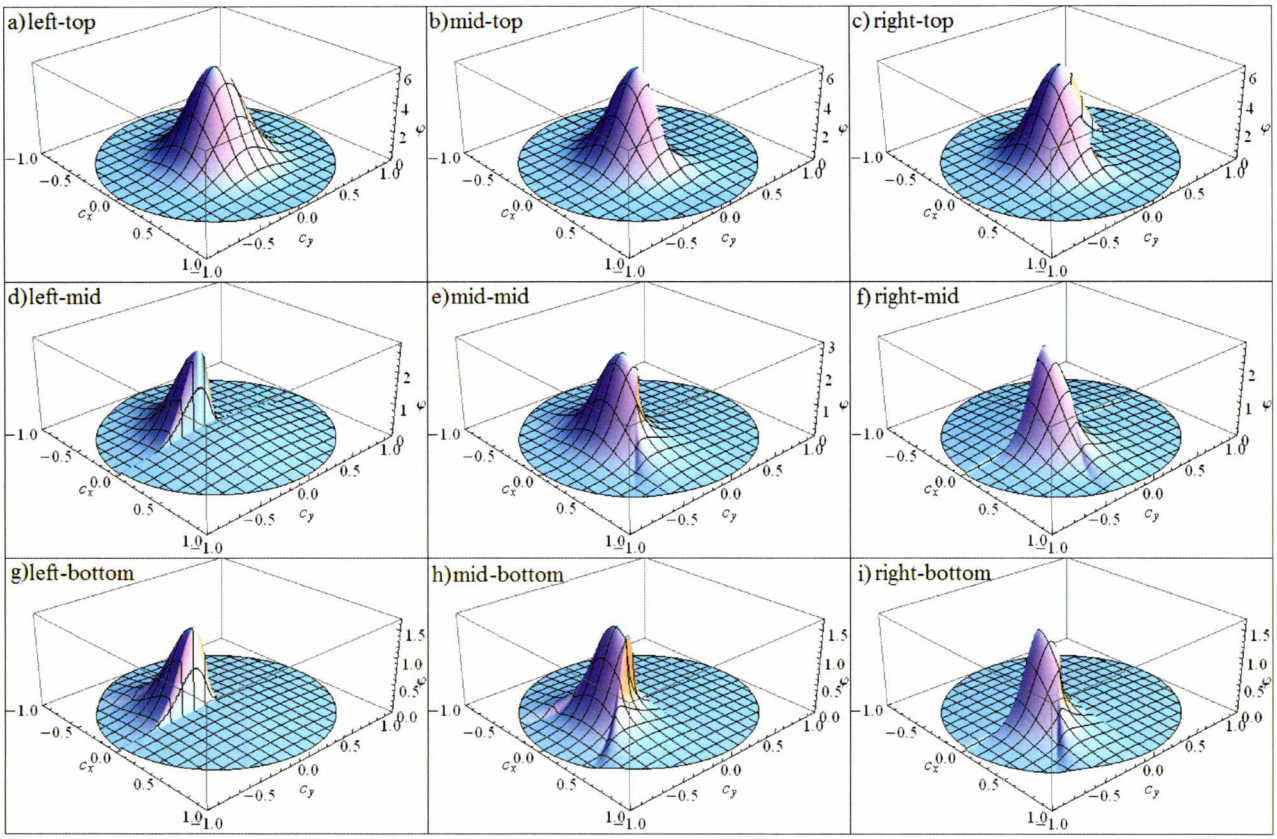

Figure 34: The distribution function at various points of the cavity for $T_C / T_H = 0.1$ and $Kn_0 = 2$.

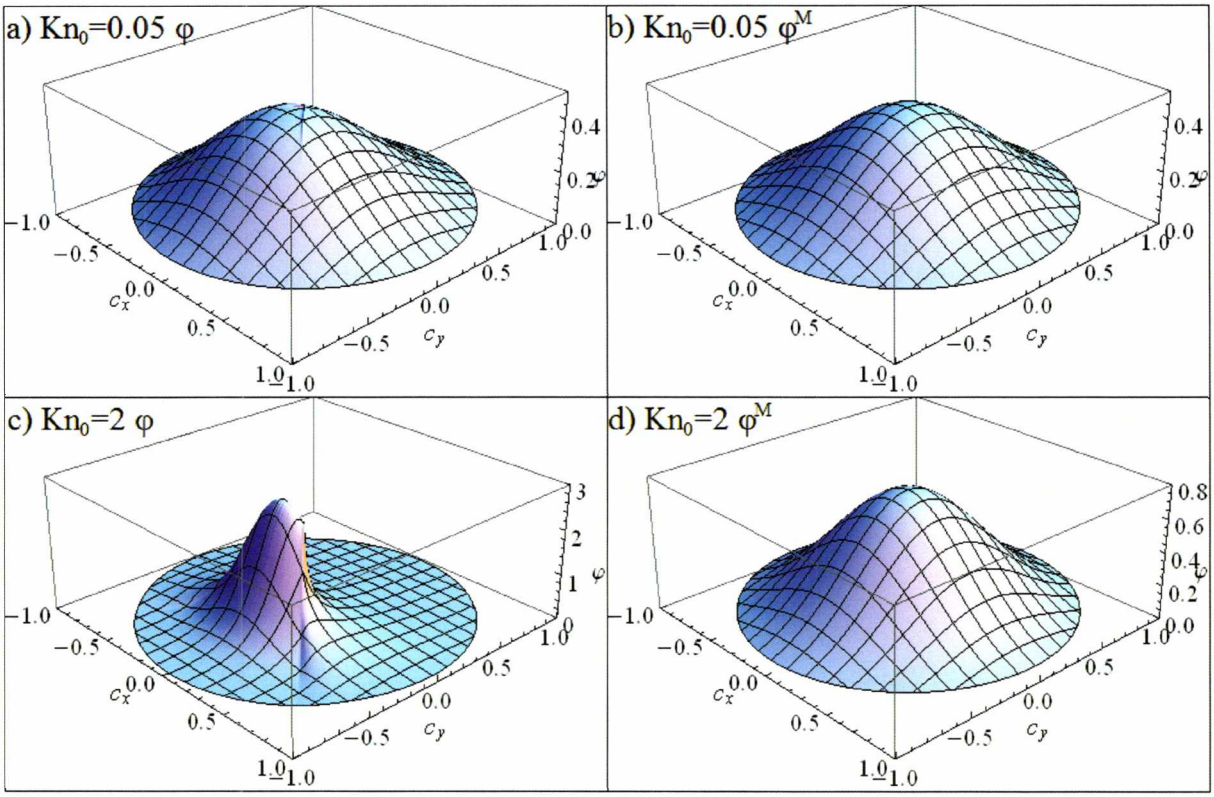

Figure 35: The distribution function (left) and the local Maxwellian distribution (right) for $Kn_0 = 0.05$ (top) and $Kn_0 = 2$ (bottom) at the center of the cavity.

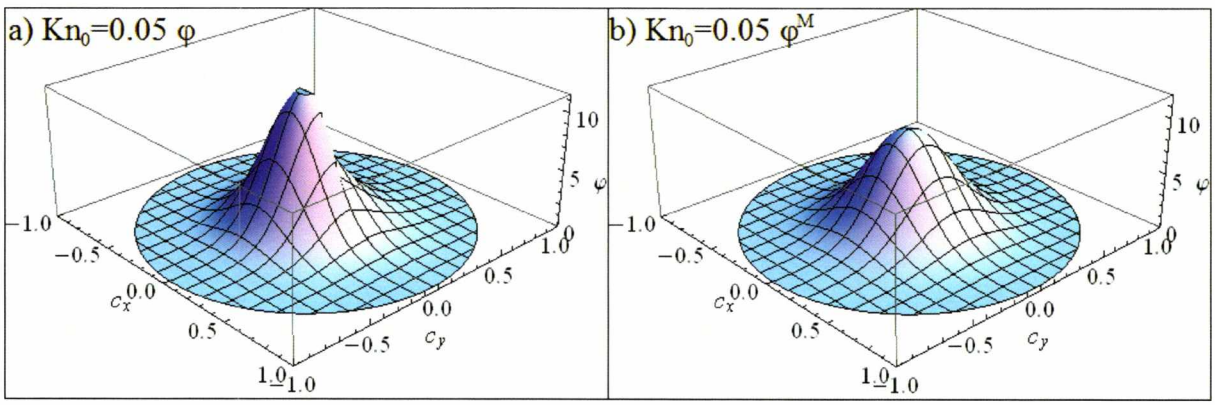

Figure 36: The distribution function at the middle of the top plate for $T_C / T_H = 0.1$ and $Kn_0 = 0.05$ (left) and the corresponding local Maxwellian (right).

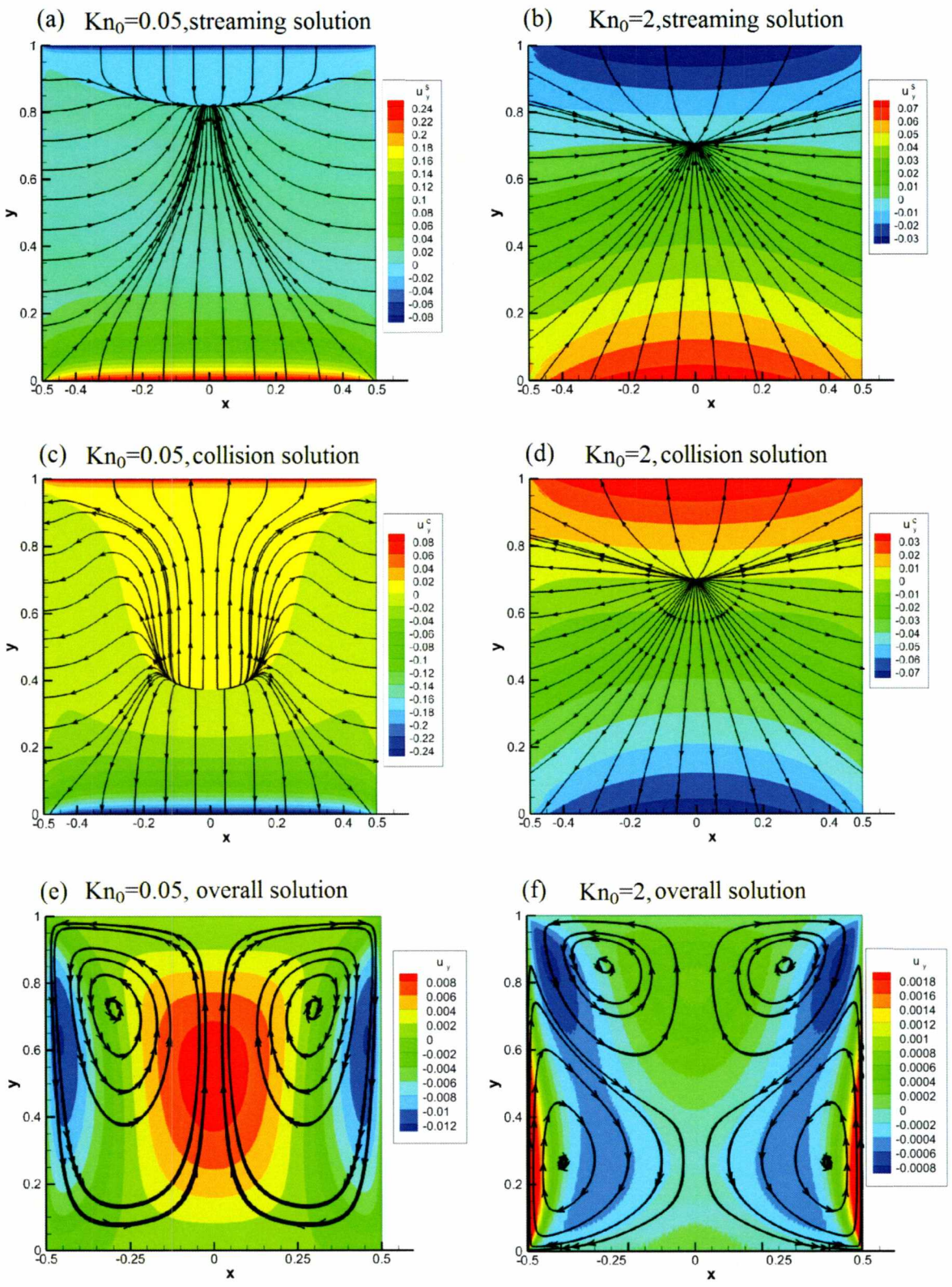

Figure 37: Streamlines and vertical velocity contours for the ballistic and collision parts as well as of the overall solution in a square enclosure for $Kn_0 = 0.05$ and 2, with $T_C / T_H = 0.1$.

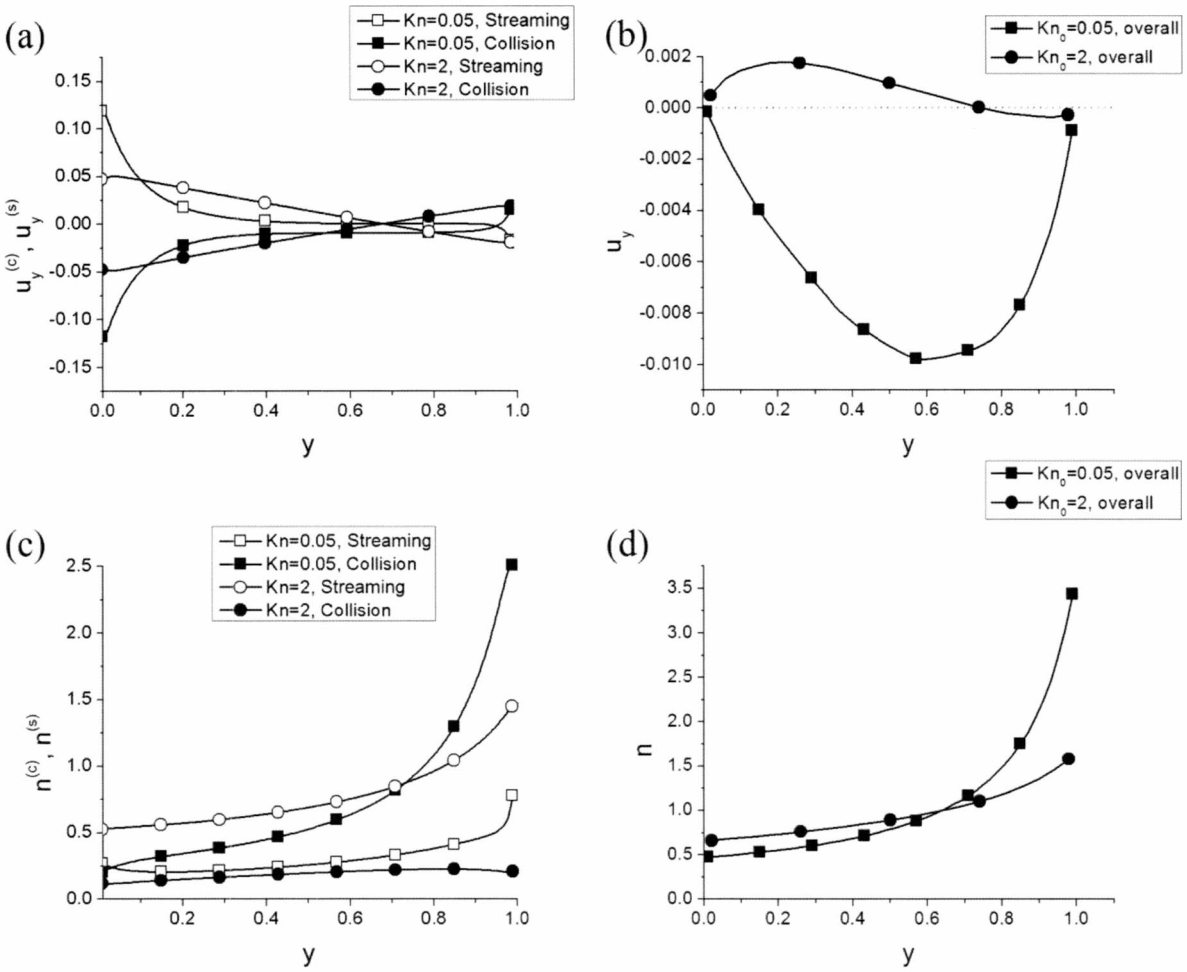

Figure 38: Tangential velocity and density of the ballistic and collision parts as well as of the overall solution in the vicinity of the lateral walls of a square enclosure for $Kn_0 = 0.05$ and 2, with $T_C / T_H = 0.1$.

Concluding remarks

Three flow/heat transfer configurations are investigated. The half heated cavity flow is investigated in terms of the reference Knudsen number for benchmarking purposes and the comparison with the results of [25] is excellent. After validating the results of the code, the bottom wall heated cavity configuration was simulated in terms of the reference Knudsen number and the temperature ratio or the heat flux departing from the bottom plate. Finally the non-isothermal lateral walls cavity configuration was investigated in terms of the reference Knudsen number, the temperature ratio of the top over the bottom plates and the aspect ratio of the enclosure. The Shakhov kinetic equation was solved numerically and results were obtained in the whole range of the Knudsen number.

The first configuration helped check the validity of the results provided by the code developed. The second configuration is of great technological importance as such flows are very common in vacuum packed micro/nano-electromechanical systems. A flow in the vicinity of the lateral walls going from hot-to-cold is observed even for small temperature differences and small reference Knudsen numbers. Another interesting finding was that the average heat flux departing from the bottom plate does not necessarily increase as the temperature difference increases. For relatively large Knudsen numbers, there is a maximum near $T_C / T_H = 0.5$. The latter case helped confirm previous results in similar non-isothermal set-ups, it has been found that in the vicinity of the lateral walls the gas is not necessarily going from hot-to-cold. Actually, even for relatively small Knudsen numbers in the slip or early transition regime a hot-to-cold flow along the non-isothermal walls is observed, which is enhanced as the Knudsen number and the temperature difference are increased. The cavity aspect ratio is also an important factor and the hot-to-cold flow is becoming more dominant as the depth compared to the width of the cavity is increased. The effect of these parameters on the flow configuration and bulk quantities has been thoroughly examined. Furthermore a procedure was introduced, equivalent to the DSMC decomposition introduced in [33] by S. Stefanov, for the decomposition of the solution into the ballistic and collision parts helping

understand the complex flow structures. It has been found that at small Knudsen numbers the collision part dominates and the classic thermal creep theory works, while at large Knudsen numbers the ballistic part prevails and then the gas along the wall flows from hot-to-cold.

It is believed that the present work has both scientific interest and technological impact and it is hoped to support the design and optimization of devices operating far from local equilibrium. Future extension to this work could be the simulation of thermally driven flows using polyatomic gasses, the simulation of the exact 3D configuration and a more extensive investigation of the decomposition procedure based on the deterministic solution of the model equations.

References

[1]: Bernoulli, Daniel. Hydrodynamica. 1738.

[2]: Clausius, Rudolf. "On the Nature of the Motion which we call Heat." Philosophical Magazine (1875): 108-127.

[3]: Maxwell, J.C. "Illustrations of the dynamical theory of gases." Philosophical Magazine (1860): 19, 19-32 and 20, 21-37.

[4]: Boltzmann, L. "Weitere Studien uber das Warmengleichgewicht unter Gasmolekulen." Wiener Berichte (1872): 66, 275-370.

[5]: Shen, Ching. Rarefied Gas Dynamics, Fundamentals, Simulations and Micro Flows. 2005.

[6]: Sone, Yoshio. Molecular Gas Dynamics, Theory, Techniques and Applications. 2007.

[7]: Bird, G.A. Molecular Gas Dynamics. 1976.

[8]: Cercignani, C. The Boltzmann equation and its Applications. 1988.

[9]: P.L. Bhatnagar, E.P. Gross, M. Krook. "A model for Collision Processes in Gases. I. Small Amplitude Processes in Charged and Neutral One-COmponent Systems." Physical Review (1954): 94(3) 511-525.

[10]: Shakhov, E.M. "Generalization of the Krook kinetic relaxation equation." Fluid Dyn. (1968): 3(5) 95-96.

[11]: Holway, L.H. Approxiamtion procedure for kinetic theory. PhD thesis, Harvard University, 1963.

[12]: Rykov, V.A. "Model Kinetic Equations for a Gas with Rotational Degrees of Freedom." Izv. Akad. Nauk. SSSR. Mekh. Zhidk. Gaza. (1975): (6), 701-115.

[13]: Holway, L.H. "New statistical models for kinetic theory." Physics of Fluids (1966): 9: 1658-1673.

[14]: McCormack, F.J. "Construction of linearized kinetic models for gaseous mixtures and molecular gases." Physics of Fluids (1973): 16: 2095.

[15]: H. Struchtrup, P. Taheri. "Macroscopic transport models for rarefied gas flows: A brief review." IMA Journal of Applied Mathematics (76 (5) 672-697): 201

[16]: Takata, S. "Note of the relation between thermophoresis and slow uniform flow problems for a rarefied gas." Physics of Fluids (2009): (21), 112001.

[17]: K. Aoki, Y. Sone, T. Tano. "Numerical analysis of a flow induced in a rarefied gas between noncoaxial circular cylinders with different temperatures for the entire range of the Knudsen number." Physics of Fluids (1989): (1), 409.

[18]: H. A. Stone, A. D. Stroock, A. Ajdari. "Engineering flows in small devices: microfluidics towards a lab-on-chip." Annual Revies of Fluid Mechanics 36 (2014): 381-411.

[19]: H.A. Yang, M.C. Wu, W.L. Fang. "Localized induction heating solder bonding for wafer level MEMS packaging." Journal of Micromechanics and Microengineering (2005): 15, 394-399.

[20]: H. Liu, M. Wang, J. Wang, G. Zhang, H. Liao, R. Huang, X. Zhang. "Monte Carlo simulations of gas flow and heat transfer in vacuum packaged MEMS devices." Applied Thermal Engineering (2007): 27: 323-329.

[21]: Y. Sone, Y. Waniguchi, K. Aoki, S. Takata. "One-way flow of a rarefied gas induced in a channel with a periodic temperature distribution." Physics of Fluids (1996): 8(8), 2227-2235.

[22]: A. Alexeenko, S. Gimelshein, E. Muntz, A. Ketsdever. "Kinetic modeling of temperature driven flows in short microchannels." International Journal of Thermal Sciences (2006): 45, 1045-1051.

[23]: A. Ketsdever, N. Gimelshein, S. Gimelshein, N. Selden. "Radiometric phenomena: From the19th to the 21st century." Vacuum (2012): 86, 1644-1662.

[24]: M. Vargas, M. Wüest and S. Stefanov. "Monte Carlo analysis of thermal transpiration effects in capacitance diaphragm gauges with helicoidal baffle system." Journal of Physics: Conference 362, 012013, 2012 (n.d.).

[25]: K. Aoki, S. Takata, H. Aikawa, F. Golse. "rarefied gas flow caused by a discontinuous wall temperature." Physics of Fluids (2001): 13 (9), 2645-2661.

[26]: S. Stefanov, V. Roussinov, C. Cercignani. "Rayleigh-Benard flow of a rarefied gas and its attractors. II. Chaotic and periodic convective regimes." Physics of Fluids (2002): 14 (7), 2270-2288.

[27]: S. Naris, D. Valougeorgis. "Gas flow in a grooved channel due to pressure and temperature gradients." 4th International Conference on Nanochannels, Microchannels and Minichannels, June 19-21, 2006, Limerick, Ireland, Paper No. ICNMMM2006-96225; Publisher: ASME June 19-21, 2006, Limerick, Ireland, Paper No. ICNMMM2006-96225; Publisher: ASME (n.d.).

[28]: Sone, Y. "Comment on "Heat transfer in vacuum packaged microelectromechanical system devices" [Phys. Fluids 20, 017103 (2008)]." Physics of Fluids (2008): 20, 017103.

[29]: A. Mohammadzadeh, E. Roohi, H. Niazmand, S. Stefanov, R. S. Myong. "Thermal and second-law analysis of a micro- or nanocavity using direct-simulation Monte Carlo." Physical Review E (2012): 85, 056305.

[30]: N. D. Masters, W. Ye. "Octant flux splitting information preservation DSMC method for thermally driven flows." Journal of Computational Physics (2007): 226, 2044-2062.

[31]: A. Rana, M. Torrilhon, H. Struchtrup. "Heat transfer in micro devices packaged in partial vacuum." Journal of Physics: Conference Series (2012): 362, 012034.

[32]: J. C. Huang, K. Xu, P. Yu. "A unified gas-kinetic scheme for continuum and rarefied flows III: Microflow simulations." Communications in Computational Physics (2013): 14 (5), 1147-1173.

[33]: Vargas, Manuel and Tatsios, Giorgos and Valougeorgis, Dimitris and Stefanov, Stefan. "Rarefied gas flow in a rectangular enclosure induced by non-isothermal walls." Physics of Fluids (2014): (26), 057101.

[34]: J.H. Ferziger, H.G. Kaper. Mathematical theory of transport processes in gases. 1972.

[35]: Melvin Epstein. "A Modell of the Wall Boundary Conditions in Kinetic Theory." AIAA Journal (1967): (10), 1797-1800.

[36]: S. Naris, D. Valougeorgis, D. Kalempa, F. Sharipov. "Gaseous mixture flow between two parallel plates in the whole range of the gas rarefaction." physica a (2004): 336(3), 294-318.

[37]: G. Breyiannis, S. Varoutis, D. Valougeorgis. "Rarefied gas flow in concentric annular tube: Estimation of the Poiseuille number and the exact hydraulic diameter." European journa of mechanics, b/Fluids (2008): (27) 609-622.
[38]: S. Naris, D. Valougeorgis. "Boundary-driven nonequilibrium gas flow in a grooved channel via kinetic theory." Physics of fluids (2007): (19), 067103.
[39]: S. Naris, D. Valougeorgis. "Rarefied gas flow in a triangular duct based on a boundary fitted lattice." European journal of mechanics, b/fluids (2008): (27), 810-822.
[40]: S. Naris, D. Valougeorgis. "Shear driven micro-flows of gaseous mixtures." Sensor letters (2006): (4), 1-7.
[41]: S. Naris, D. Valougeorgis. "The driven cavity flow over the whole range of the Knudsen number." Physics of Fluids (2005): (17), 097106.
[42]: S. Naris, D. Valougeorgis, D. Kalempa, F. Sharipov. "Flow of gaseous mixtures through rectangular microchannels driven by pressure, temperature, and concentration gradients." Physics of fluids (2005): (17), 100607.
[43]: S. Naris, D. Valougeorgis, F. Sharipov, D. Kalempa. "Discrete velocity modelling of gaseous mixture flows in MEMS." Superlatices and microstruvtures (2004): (35), 629-643.
[44]: S. Pantazis, D. Valougeorgis. "Rarefied gas flow through a cylindrical tube due to a small pressure difference." European journal of mechanics, B/fluids (2013): (38), 114-127.
[45]: S. Varoutis, S. Naris, V. Hauer, C. Day, D. Valougeorgis. "Computational and experimental stude of gas flows through long channels of various cross sections in the whole range of the Knudsen number." J. Vac. Sci. Technol. A (2009): 27(1).
[46]: S. Pantazis, D. Valougeorgis. "Heat transfer through rarefied gases between coaxial cylindrical surfces with arbitrary temperature differences." European Journal of mecahnics, b/Fluids (2010): (6), 494-509.
[47]: S. Mizdanitis, S. Pantazis, D. Valougeorgis. "Pressure driven rarefied gas flow through a slit and an orifice." Vacuum (2012): (86), 1701-1708.
[48]: S. Pantazis, S. Naris, C. Tantos, D. Valougeorgis, J. Andre, F. Millet, J.P. Perin. "Nonlinear vacuum gas flow through a short tube due to pressure and temperature gradients." Fusion engineering and design (2013): (88), 2384-2387.
[49]: Titarev, V.A. "Conservative numerical methods for model kinetic equations." Computers and Fluids (2007): (9), 1446-1459.
[50]: D. Valougeorgis, S. Naris. "Acceleration schemes of the discrete velocity method: gaseous flows in rectangular microchannels." SIAM J. Sci. Comput. (2003): 25(2), 534-552.
[51]: I. Graur, A. Ph. Polikarpov. "Comparison of different kinetic models for the heat transfer problem." Heat Mass Transfer (2009): 46, 237244.
[52]: Titarev, V. A. "Rarefied gas flow in a planar channel caused by arbitrary pressure and temperature drops." International Journal of Heat and Mass Transfer (2012): 55 (21-22), 5916-5930.
[53]: V. A. Titarev, E. M. Shakhov. "Computational study of a rarefied gas flow through a long circular pipe into vacuum." Vacuum (2012): 86 (11), 1709-1716.
[54]: V. A. Titarev, E. M. Shakhov, S. V. Utyuzhnikov. "Rarefied gas flow through a diverging conical pipe into vacuum." Vacuum (2014): 101, 10-17.
[55]: V. A. Titarev, M. Dumbser, S. V. Utyuzhnikov. "Construction and comparison of parallel implicit kinetic solvers in three spatial dimensions." Journal of Computational Physics (2014): 256, 17-33.

[56]: S. Misdanitis, S. Pantazis, D. Valougeorgis. "Pressure driven rarefied gas flow through a slit and an orifice." Vacuum (2012): 86, 1701-1708

[57]: S. Pantazis, D. Valougeorgis. "Non-linear heat transfer through rarefied gases between coaxial cylindrical surfaces at different temperatures,." European Journal of Mechanics B/Fluids (2010): 29, 494-509.

[58]: K. Aoki, C. Bardos, C. Dogbe, F. Golse. "A note on the propagation of boundary induced discontinuities in kinetic theory." Mathematical Models and Methods in Applied Sciences (2001): 11(9), 1581-1595.

[59]: Y. Sone, T. Takata. "Discontinuity of the velocity distribution function in a rarefied gas around a convex body and the s layer at the bottom of the Knudsen layer." Transport Theory and Statistical Physics (1992): 21, 501-530.

[60]: Tatsios Giorgos, Vargas H. Manuel, Stefanov K. Stefan, Valougeorgios Dimitri. "Non-equilibrium gas glow and heat transfer in a bottom heated square microcavity." 4th Micro and Nano Flows Conference. 2014.

Appendix A

If we consider a phase space element $d\vec{\xi}d\vec{r}$ then the number of molecules in this element is $f\left(\vec{r},\vec{\xi},t\right)d\vec{\xi}d\vec{r}$. The rate of change of the number of molecules is $\frac{\partial}{\partial t}f(\vec{r},\vec{\xi},t)d\vec{\xi}d\vec{r}$. This change can occur by molecules crossing the boundaries of the physical space element $d\vec{r}$ due to their free motion, by molecules crossing the boundaries of the molecular velocity space element $d\vec{\xi}$ due to field forces acting on them and by molecules entering or leaving the velocity space element $d\vec{\xi}$ due to their collisions.

For the calculation of the rate of change due to the free motion of molecules let's consider a cubic physical space element $d\vec{r} = dxdydz$. The number of particles crossing the boundary at x through a surface of area $dydz$ perpendicular to the x-axis during dt is

$$fd\vec{\xi}\ \xi_x dtdydz .$$

The number of particles crossing the boundaries at x+dx crossing a surface of area $dydz$ perpendicular to the x-axis during dt is

$$\left(\xi_x f + \frac{\partial(\xi_x f)}{\partial x}dx\right)d\vec{\xi}dtdydz .$$

It follows that the net gain of molecules crossing the two sides perpendicular to the x-axis is

$$-\frac{\partial(\xi_x f)}{\partial x}dxd\vec{\xi}dtdydz .$$

In proportion to this the net gain of molecules through the other sides is

$$-\frac{\partial(\xi_y f)}{\partial y}dyd\vec{\xi}dtdxdz$$

and

$$-\frac{\partial(\xi_z f)}{\partial z}dzd\vec{\xi}dtdxdy .$$

Summing these three quantities we have

$$\left(\frac{\partial f}{\partial t}\right)_{\substack{free\\motion}} dt = -\left(\frac{\partial(\xi_x f)}{\partial x} + \frac{\partial(\xi_y f)}{\partial y} + \frac{\partial(\xi_z f)}{\partial z}\right) d\vec{\xi} dt dx dy dz = -\vec{\xi}\frac{\partial f}{\partial \vec{r}} d\vec{r} d\vec{\xi} dt \qquad (A.1)$$

In order to calculate the rate of change of molecules due to field forces, we have to assume a square element $d\vec{\xi} = d\xi_x d\xi_y d\xi_z$ of the molecular velocity space. The force field acted on the molecules is $\vec{F}$ and is in force per unit of mass. The velocity of the particles linearly alters their position, and moves them through the boundaries of the physical space element $d\vec{r} = dxdydz$. This is equivalent to the force acted on molecules that linearly alters their velocity and moves them through the boundaries of the velocity space element $d\vec{\xi} = d\xi_x d\xi_y d\xi_z$. So according to the previous result, we have

$$\left(\frac{\partial f}{\partial t}\right)_{\substack{field\\forces}} dt = -\left(\frac{\partial(F_x f)}{\partial \xi_x} + \frac{\partial(F_y f)}{\partial \xi_y} + \frac{\partial(F_z f)}{\partial \xi_z}\right) d\vec{r} dt d\xi_x d\xi_y d\xi_z = -\vec{F}\frac{\partial f}{\partial \vec{\xi}} d\vec{r} d\vec{\xi} dt \qquad (A.2)$$

The rate of change of molecules in the phase space element is more complicated. Let us consider two types of molecules, those with velocity $\vec{\xi}$ (type 1) and those with velocity $\vec{\xi}_1$ (type 2). When a collision occurs between a molecule of type 1 and a molecule of type 2, their respective post collision velocities are $\vec{\xi}^*$ and $\vec{\xi}_1^*$. Considering a single molecule of type 1 traveling through molecules of type 2, with a relative velocity $\vec{c}_r = \vec{\xi} - \vec{\xi}_1$, the volume swept by the molecule in time dt is $\vec{c}_r \sigma d\Omega dt$, where σ is the differential cross section and $d\Omega$ is the differential element of the solid angle in which the molecule will scatter after the collision. The number of molecules with velocities about $\vec{\xi}_1$ is $f_1 d\vec{\xi}_1$, which gives for the number of collisions of a molecule with velocity $\vec{\xi}$ and molecules with velocity $\vec{\xi}_1$ in dt the expression $\vec{c}_r f_1 \sigma d\Omega d\vec{\xi}_1 dt$. In the phase space element $d\vec{\xi}d\vec{r}$ there are $f d\vec{\xi} d\vec{r}$ molecules with velocities about $\vec{\xi}$, so the number of collisions between molecules with velocities $\vec{\xi}$ and $\vec{\xi}_1$ becomes

$$\vec{c}_r f_1 f d\vec{c} d\vec{r} \sigma d\Omega d\vec{c}_1 dt .$$

This is the number of collisions of type $\left(\vec{\xi}, \vec{\xi}_1 \rightarrow \vec{\xi}^*, \vec{\xi}_1^*\right)$ that take molecules out of the velocity space element $d\vec{\xi}$. The inverse collisions $\left(\vec{\xi}^*, \vec{\xi}_1^* \rightarrow \vec{\xi}, \vec{\xi}_1\right)$ that move molecules into

$d\vec{\xi}$ have also to be considered. Taking into account the symmetry and analogy of the direct and inverse collisions, the number of such collisions is

$$\vec{c}_r f_1^* f^* d\vec{\xi} d\vec{r} \sigma d\Omega d\vec{\xi}_1 dt .$$

The net gain of molecules with velocities about $\vec{\xi}$ due to collisions with molecules with velocities about $\vec{\xi}_1$ is

$$\left(f_1^* f^* - f_1 f\right)\vec{c}_r \sigma d\Omega d\vec{\xi}_1 d\vec{\xi} d\vec{r} dt .$$

The net gain of molecules with velocities about $\vec{\xi}$ due to all collisions in dt can be found integrating the previous expression

$$\left(\frac{\partial f}{\partial t}\right)_{collisions} dt = \left(\int_{-\infty}^{\infty}\int_{0}^{4\pi}\left(f_1^* f^* - f_1 f\right)\vec{c}_r \sigma d\Omega d\vec{\xi}_1\right) d\vec{\xi} d\vec{r} dt \qquad (A.3)$$

Summing the previous expressions we get

$$\frac{\partial}{\partial t} f(\vec{r},\vec{\xi},t) d\vec{\xi} d\vec{r} = \left(\frac{\partial f}{\partial t}\right)_{\substack{free \\ motion}} + \left(\frac{\partial f}{\partial t}\right)_{\substack{field \\ forces}} + \left(\frac{\partial f}{\partial t}\right)_{collisions} \Rightarrow$$

$$\frac{\partial}{\partial t} f(\vec{r},\vec{\xi},t) d\vec{\xi} d\vec{r} = -\vec{\xi}\frac{\partial f}{\partial \vec{r}} d\vec{r} d\vec{\xi} - \vec{F}\frac{\partial f}{\partial \vec{\xi}} d\vec{r} d\vec{\xi} + \left(\int_{-\infty}^{\infty}\int_{0}^{4\pi}\left(f_1^* f^* - f_1 f\right)\vec{c}_r \sigma d\Omega d\vec{\xi}_1\right) d\vec{\xi} d\vec{r} \Rightarrow$$

$$\frac{\partial}{\partial t} f(\vec{r},\vec{\xi},t) + \vec{\xi}\frac{\partial f}{\partial \vec{r}} + \vec{F}\frac{\partial f}{\partial \vec{\xi}} = \int_{-\infty}^{\infty}\int_{0}^{4\pi}\left(f_1^* f^* - f_1 f\right)\vec{c}_r \sigma d\Omega d\vec{\xi}_1 = J(f) \qquad (A.4)$$

which is the Boltzmann equation.

ΠΑΝΕΠΙΣΤΗΜΙΟ ΘΕΣΣΑΛΙΑΣ
ΒΙΒΛΙΟΘΗΚΗ
004000121292

ΠΑΝΕΠΙΣΤΗΜΙΟ ΘΕΣΣΑΛΙΑΣ
ΒΙΒΛΙΟΘΗΚΗ